MAX-PLANCK-INSTITUT FÜR KOLLOID- UND GRENZFLÄCHENFORSCHUNG

Molecular Design of Heteroatom-doped Nanoporous Carbons with Controlled Porosity and Surface Polarity for Gas Physisorption and Energy Storage

Dissertation

zur Erlangung des akademischen Grades "doctor rerum naturalium" (Dr. rer. nat.)
in der Wissenschaftsdisziplin "Kolloidchemie"

eingereicht an der Mathematisch-Naturwissenschaftlichen Fakultät
der Universität Potsdam
von

Sol Youk

Potsdam-Golm, im August 2021

Published online on the
Publication Server of the University of Potsdam:
https://doi.org/10.25932/publishup-53909
https://nbn-resolving.org/urn:nbn:de:kobv:517-opus4-539098

Acknowledgement

First of all, I would like to express my deepest appreciation to my senior supervisor, Prof. Dr. Markus Antonietti, for providing the precious opportunity and generous scientific support to study in Max Planck Institute of Colloids and Interfaces. The guidance on the direction of my research as well as his passion for the scientific research have been enough to keep me motivated for the research. I've always thought it would be really great if I could become a scientist like him.

My sincerest special acknowledgment goes to my supervisor, Prof. Dr. Martin Oschatz. His generosity, tolerance, and patience have been very supportive throughout my studies all the time. Even though I had no any knowledge in adsorption and energy storage at the beginning, he always answered the millions of questions I had, so I could feel myself growing throughout entire my Ph.D. Discussions with him were always constructive and enjoyable, and I was filled with courage and optimism after every single scientific discussion. Not only the scientific inspiration but the discussions of overall life with beer also gave me a lot of positive energy from him. I would like to express my infinite gratitude for his all support.

I would like to thank the all collaborators of these works. Without their assistance of the evaluations and discussions, I would never have completed my research. I thank Prof. Dr. Jan Philipp Hofmann at the Eindhoven University of Technology, The Netherlands, for the XPS measurement and Dr. Torsten Gutmann and M. Sc. Edina Šić for the ssNMR analysis. I am very grateful to Dr. Nadezda V. Tarakina, Bolortuya Badamdorj, and Heike Runge for the SEM, TEM, and EDX measurements, Antje Völkel for TGA, EA, and DSC, Ines Below-Lutz for synthesis of HAT-CN precursors and the support of lab safety, Regina Rothe for the support of physisorption, and Jessica Brandt for ICP-OES and the support of lab safety. Thank Dr. Aleksandr Savateev and Dr. Nieves Lopez Salas for providing me the access for the facilities in their labs.

I thank very nice my group members and colleagues in MPI in Golm. I had a lot of respect for every of them although I could not express much. I am truly grateful for the memories with them, especially many parties at Chez Briel. I would like to express my gratitude to GT Love, Berlin Writing Gemeinshaft, my friends in Korea, my alumni friends in Berlin, and all the people who have made up my memories even including many Youtubers who helped me a lot during the COVID lockdown period.

I would like to thank my committee members and reviewers for their time to suggest me the precious advices. My deep gratitude goes to my parents as well to my brother. Last but not least, 수고했다 솔, 행복하자!

Table of Contents

1. Motivation 1
2. Background and Outline 5
2.1. Carbon, as a chemical element 5
2.2. The pore structure of porous carbon materials 8
2.2.1. Synthetic approaches to porous carbon materials 9
2.3. Functionalization of porous carbon materials 16
2.3.1. Various approaches to synthesize heteroatom-doped porous carbon materials 19
2.3.2. Electronic properties of heteroatom-doped carbon materials 20
2.4. Porous carbon materials on various applications 24
2.4.1. The selective CO_2 adsorption over N_2 27
2.4.2. Capacitors with nitrogen-doped porous carbon in aqueous electrolyte 31
2.5. Outline 36
3. Results and Discussions 38
3.1. Controlling pore size and pore functionality in sp^2- conjugated microporous materials by precursor chemistry and salt templating 38
3.1.1. Background and state-of-the-art 38
3.1.2. Nitrogen- oxygen- lined porous carbon by salt-templating 42
3.1.3. Structural characterizations for nitrogen- oxygen- lined carbons 53
3.2. Molecular designed nanoporous carbon from citrazinic acid and melamine for physisorption and energy storage of various polar adsorbates 60
3.2.1. Background and state-of-the-art 61
3.2.2. The physical properties and pore Structure of citrazinic acid and melamine based porous carbon 64
3.3. Carbon materials with kinetically favorable pore structure by direct pyrolysis of a preorganized hexaazatriphenylene precursor 82
3.3.1. Background and state-of-the-art 83
3.3.2. The pore structure properties of Vac-HAT-Ts and C-HAT-Ts 84
4. Conclusions and Perspectives 94
5. References 99
6. Appendix 113
6.1 List of abbreviations 113
6.2 Characterization methods 114

6.3 Experimental process 129
6.4 Supporting tables and figures 132
6.4.1 List of tables 139
6.4.2 List of Figures 140
List of Publications 144
Declaration 145

1. Motivation

The world energy consumption has constantly increased every year due to economic development and population growth, with 2018 seeing 70% higher than the average increase since 2010.[1] Despite ongoing efforts to replace fossil fuels with renewable energy such as solar and wind power, fossil resources are still the main energy source of the world according to a report released in 2020 (**Figure 1.1**a).[2] This inevitably caused CO_2 emissions to rise to 33.1 Gt in 2018. The CO_2 concentration in the atmosphere meanwhile passed a value of 400 ppm, and these figures are ever increasing with economic growth (**Figure 1.1**b).[3,4] Due to the alarming situation, a world-wide initiative was launched in 2010 to reduce global carbon emissions by 45% by 2030 and reach zero net carbon by 2050.[5,6] Global energy demand in 2020 recorded a 6% decline for the first time in 70 years,[2] but efforts to reduce carbon emissions still must be maintained and increased as one of main reasons of the decline seems to be due to the COVID-19 pandemic situations.[1]

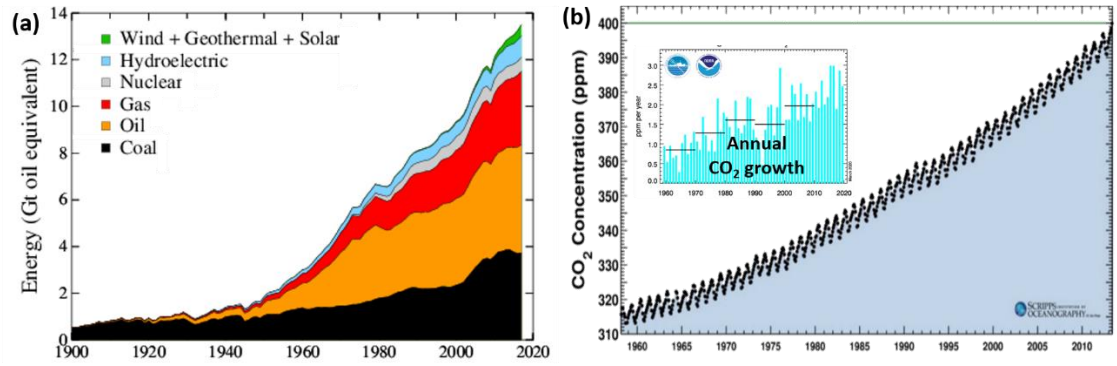

Figure 1.1 (a) Total energy supply by source from 1900 to 2018, and (b) increase of the atmospheric CO_2 concentration measured from 1958 to 2015.

In addition to CO_2 emission reduction, carbon capture and storage (CCS) is also important in preventing the enrichment of CO_2. The capture process that artificially absorbs existing carbon dioxide is an integral process that accounts for 70-80% of the total cost of the CCS.[7] Depending on its mechanism, the capture can be classified into two types – chemisorption, which utilizes chemical adsorption; and physisorption, which utilizes physical adsorption at the interface between adsorbent and adsorbate. Chemisorption is more widely used because of its high efficiency and selectivity. Solvents such as monoethanol-amine (MEA) and diethanolamine absorb CO_2 easily so they are used in the post combustion capture (PCC), in which carbon dioxide generated from fossil fuels is able to be immediately and directly removed.[8-10] However, there are many bottlenecks to be solved, such as solvent loss, amine degradation, vulnerability to heat and toxicity. In particular, the high cost of regeneration, caused by the strong attraction of carbon dioxide is demanding and requires a huge amount of energy to separate it from the solvent. This is one of the biggest obstacles for chemisorption.[11-13]

On the other hand, some of these drawbacks can be compensated through physisorption. Zeolites, a family of crystalline porous aluminosilicates built of adjacent SiO_4 and AlO_4 tetrahedra,[14] have shown promising results in separating CO_2 from gas mixtures by displaying significant adsorption selectivity and capacity even in ambient conditions.[15-18] Synthesized under hydrothermal conditions from an alkali-rich aluminosilicate hydrogel system where water plays an important role not only as a reactant component but reaction medium, zeolites with their high polarity provide the necessary strong affinity with carbon dioxide. Another promising material for physical CO_2 binding are metal-organic frameworks (MOFs), which are a type of crystalline porous material invented in the late 1990's.[19] MOFs, synthesized by self-assembly of organic ligands and metal or

metal oxide clusters, not only have an incredibly high specific surface area (~ 7800 m^2 g^{-1}) and pore volume (~ 5 cm^3 g^{-1}),[20] but also provide a regular pore structure with a variety of functional chemical sites. Among more than 90,000 species, certain species of MOFs have been reported to have a high adsorption capacity and selectivity for carbon dioxide adsorption even exceeding those of zeolites.[21-24] However, limitations for both materials exist. Zeolites demand relatively high regeneration energy and have limited adsorption kinetics due to the exceptionally narrow pore structure. MOFs have low stability against heat and moisture and high manufacturing cost.

Nanoporous carbons have recently received attention as an attractive functional porous material due to their unique properties.[25-27] These materials are crucial in many applications of modern science and industry such as water and air purification, catalysis, gas separation, and energy storage/conversion due to their high chemical and thermal stability, and in particular electronic conductivity in combination with high specific surface areas.[28-30] [28-30] Nanoporous carbons can be used to adsorb environmental pollutants or small gas molecules such as CO_2 and to power electrochemical energy storage devices such as batteries and fuel cells. In all fields, their pore structure or electrical properties can be modified depending on their purposes.

This thesis provides an in-depth look at novel nanoporous carbons from the synthetic and the application point of view. The interplay between pore structure, atomic construction, and the adsorption properties of nanoporous carbon materials are investigated. Novel nanoporous carbon materials are synthesized by using simple precursor molecules containing heteroatoms through a facile templating method. The affinity, and in turn the adsorption capacity, of carbon materials toward polar gas molecules (CO_2 and H_2O) is enhanced by the modification of their chemical construction. It is also shown that these properties are important in electrochemical energy storage,

here especially for supercapacitors with aqueous electrolytes which are basically based on the physisorption of ions on carbon surfaces. This shows that nanoporous carbons can be a “functional” material with specific physical or chemical interactions with guest species just like zeolites and MOFs. With the advantages of high electrical conductivity, well-developed pore structure, highly hydrophilic surface structure, nanoporous carbons is a very promising material that has wide implications for different fields of future energy needs.

2. Background and Outline

2.1. Carbon, as a chemical element

Carbon is the fourth most abundant element in the universe after hydrogen, helium and oxygen. It is the second most abundant element in our body after oxygen and ubiquitous in all of life – food, clothes, buildings and even the Earth itself. As there are 4 valence electrons in the outermost shell of a carbon atom, carbon can form many covalent bonds with other elements, most notably hydrogen, nitrogen, oxygen, phosphorus, and sulfur. Due to the electrical properties of carbon, it can have many different stable oxidation states.[31,32] Carbon also forms a wider variety of molecular structures than other elements through orbital hybridization. Depending on the number of orbitals used, the bonding modes of sp, sp^2, and sp^3 hybrid orbitals allow carbon to combine with atoms of other elements or other carbon atoms to form an enormous array of stable organic and inorganic materials. There are over 10 million of carbon compounds that are theoretically possible under standard conditions.[33]

Carbon can create bonds with other carbons allowing it to have several allotropes.[34] Diamond, for example, has carbon atoms attached to four neighboring carbon atoms in which all carbons are sp^3- hybridized and tetrahedrally coordinated (**Figure 2.1**a). Thus, it forms a cubic crystal structure, which accounts for its characteristic hardness (Mohs hardness = 10), extraordinary durability, and a wide bandgap. On the other hand, graphite consists of a stack of layers in which each carbon atom is bonded to three other atoms to form an extended sp^2- hybridized structure (**Figure 2.1**b). Arranging a regular two-dimensional structure of carbon hexagons leads to black, brittle, and electrical conductors.[35] Graphene, which is a single layer isolated from graphite, is well known for

its superior electron mobility due to the delocalized electrons in sp^2- conjugated structures. Thus it is used in many applications such as solar cells and light-emitting diode (LEDs; **Figure 2.1**c).[36-40] When the graphene is rolled up in a cylindrical, long and hollow shape, it becomes a carbon nanotube (**Figure 2.1**d).[41] As a semiconductor with metallic properties and a moderate bandgap, it not only has specific properties in terms of electrical and thermal conductivity but also significantly high stiffness (Young's modulus ~ 4 TPa).[42-45] While Graphene and carbon nanotubes are 2-dimensional and 1-dimensional carbon allotropes, respectively, fullerene is a 0-dimensional shaped carbon in which 60 or more carbon atoms form a soccer ball-like hollow structure (**Figure 2.1**e).[46] Carbon is not only a very abundant element, but also exhibits different physical and chemical properties for each allotrope, so it theoretically has numerous applications in a wide range of fields such as electronics, sensing, medicine, and quantum computing.

Porous carbon is one of the carbon types that has a less-defined atomic construction. Compared to graphene, porous carbon has a lower degree of ordering and contains high amounts of defective motives such as 5-rings, n-rings ($n \geq 7$), heteroatoms, and atomic loss sites which eventually cause the distortion in the entire structure (**Figure 2.1**f). However, sp^2- carbon bonds are still dominant in the materials, so it has high electrical conductivity as well as chemical and thermal stability.[47,48] Furthermore, due to their incredibly high specific surface area and porous structure created by the abundant defects, porous carbons are used in a wide range of applications (e.g., molecular sieves,[49] gas storage,[50,51] adsorbents,[52] catalysts,[53] fuel cells,[54,55] electrodes for batteries,[56] supercapacitors,[57] water/air purifications,[58] and medical/biomedical devices[59,60]). They are particularly suitable where large interface areas are required. For each application, the porous carbon materials must be differently designed depending on the purposes and consideration of

various factors such as specific surface area, pore volume, geometry, hydrophilicity, conductivity, and durability.

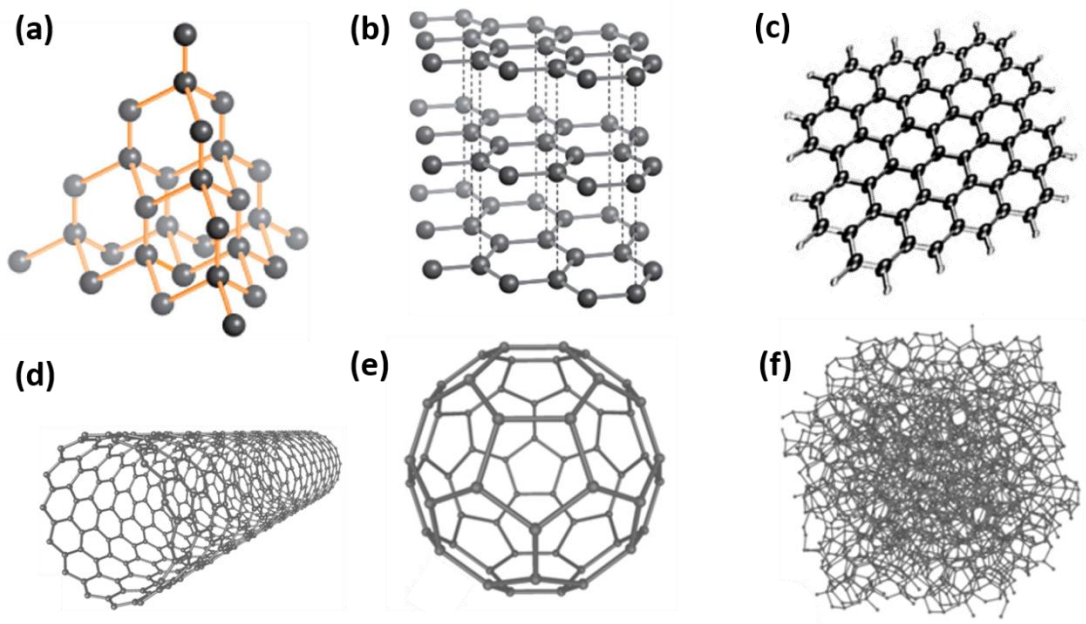

Figure 2.1 Different carbon allotropes. (a) Cubic diamond, (b) graphite, (c) graphene, (d) carbon nanotube, (e) fullerene and (f) nanoporous carbon materials (adapted with permission from (a,b,c)[61], (d-f)[62], respectively)

Novel porous carbon structures can be synthesized from inorganic/organic substances as precursors. Templating methods are often applied, as they are one of the facile methods to control the porosity of nanoporous carbon materials.[63-65] The polarity of the surfaces can be adjusted by introducing heteroatoms into the previously synthesized porous carbon materials or by carbonizing a carbon precursor containing a specific heteroatom element in advance.[66,67] These factors will be discussed in detail in the next sections (**Chapter 2.2**, and **2.3**).

2.2. The pore structure of porous carbon materials

In order for carbon to be utilized as a functional material, a specific pore system needs to be formed. Porous carbon materials are classified by their pore width which can be characterized by physisorption. The International Union of Pure and Applied Chemistry (IUPAC) divides the pores into micropores (a pore width of 2 nm or less), mesopores (a pore width from 2 nm to 50 nm), and macropores (a pore width of 50 nm or more).[68] As porous carbons generally have an irregular pore structure as mentioned, various methods of synthesizing porous carbons have been developed to control the pore structures as well as analyze the properties of the specific pore size. The suitable pore size depends on the purpose of the targeted application.

Micropores occupy the largest portion of the specific surface area, at least 90 %, and often have a large pore volume, and therefore have high capacity of adsorption of gases or liquids in carbon materials.[69,70] In electrochemical double-layer capacitor (EDLC) systems, for example, it has been shown that the specific capacitance sharply increases when the pore size is lower than 1 nm.[71,72] Besides the adsorption of micropollutants, for example, small halogenated organic compounds were also adsorbed in small carbon pores with width below about 1.5 nm.[73] When a carbon structure is constructed, a specific gas (e.g., CO_2) fitting to the present pore size from a mixture can be selectively and preferentially adsorbed on the materials. In other words, via a molecular sieving effect, it is possible to conduct a selective adsorption towards a specific desired gas species, which eventually requires low energy for selective adsorption as well as recovery of that gas at low pressure.[74-76] However, controlling strictly the desired pore size is a big challenge in porous carbon materials while a unique pore size is available in ordered functional microporous materials such as zeolites. Therefore, a lot of research has been conducted toward the pore size control and

pore distribution of porous carbons over the conventional pristine carbon with high complexity.[77-80]

Meanwhile, the demand for mesopore materials with larger pore-sized has grown as micropores have limitations in applications including lagged mass transport in the confined space of narrow pore size, low conductivity coming from high amount of defects or functional groups on the surface especially in large particles, and the destruction of the pore structure during carbonization at high temperature.[63,81] For instance, in the case of the EDLC mentioned above, the capacitance performances at high current density, which can be limited in the micropore structure, was highly improved when mesopores or meso/macropores are introduced into porous carbon forming a so-called hierarchical structure.[82-84] Moreover, in various electrochemical energy conversion reactions, such as methanol oxidation[85,86] and oxygen reduction reaction (ORR)[87-89], ordered mesoporous carbons (OMCs) have been reported to benefit from an interconnected pore network as well as tailorable surface chemistry, outperforming the specific activity of commercial catalysts.[90] Therefore, control over the design of the pore architecture is important for the use of porous carbon materials in different applications. Various synthetic approaches to construct these pore structures are described in the next chapter (**Chapter 2.2.1**).

2.2.1. Synthetic approaches to porous carbon materials

2.2.1.1. Activation

The porosity can be formed via carbonization of precursors obtained from natural or synthetic sources, followed by an activation process which enhances the porosity. The latter is a method of obtaining activated carbon with an increased surface area and pore volume through a chemical or

physical treatment on carbonaceous materials. In **physical activation**, the materials are activated in the presence of activating agents such as CO_2[91,92] and H_2O[92,93]. A relatively higher temperature is needed and the elimination of resulting carbons is inevitable, but the method is simple and the damage to the material itself can be minimized.[94] On the other hand, **chemical activation** is a single step process where carbonization is carried out in the presence of a chemical activating substance such as KOH[95,96], $ZnCl_2$[97,98], and H_3PO_4[98,99], which accompanies the additional chemical treatments and residuals of chemical agents on materials, but still has the advantages of enhancing the yield of porous carbons and demanding rather low temperatures.[94] The methods of generating porous carbon via activation are widely used in industry because of their cost efficiency.[100,101]

2.2.1.2. Templating methods

On the other hand, carbonization in the presence of templates can be carried out in order to attain a more defined and in some cases even ordered porous structure. The resulting carbon materials often have high surface area and uniform pores, making them suitable as catalyst supports, adsorbents, for electrical applications, and in many other applications where defined and uniform porosity are needed. While activation mostly induces microporous, templating methods can be used to synthesize highly sophisticated structures from microporous and/or mesoporous even to hierarchical pore systems.[102,103] Replication, the basic principle of templating, involves filling the internal or external of a specific solid with a target material, then followed by carbonization and physically or chemically separation the resulting materials from the template.

The basic principle of templating nanostructured materials is to precipitate molecular species on surfactants as a template to form a specific porous structure.[104] In other words, due to the amphiphilic properties of surfactants in which both hydrophilicity and hydrophobicity exist in one

molecule, a micelle-like structure tends to form resulting in specific porous structures. This sol-gel chemistry was further developed into **soft-templating** in the late 90s. In soft-templating for carbon synthesis, a block copolymer (BCP) as an organic template and precursor species are mixed in dilute solution followed by evaporation induced self-assembly (EISA).[105,106] After the heat treatment and carbonization process, the ordered mesoporous carbon structure is obtained (**Figure 2.2**). Ordered mesoporous silica materials are formed from soft templating in solution in which silicate precursors were used to form the resulting inorganic materials such as SBA-x (Santa Barbara Amorphous type material, the University of California, Santa Barbara)[107,108] and KIT-x (Korea Advanced Institute of Science and Technology, KAIST)[109]. For the reason of the controllable and tunable pore size and pore structures by a rich variety of soluble BCPs, soft-templating has been widely used in the synthesis of mesoporous materials.[110] However, there still were weaknesses such as poor thermal stability of BCP and limited material composition. These drawbacks can be circumvented by using **hard-templating**.[49,111] Inorganic molds which are usually the resulting materials of soft-templating are used as a "hard-template" and filled with various precursor materials to be converted into a framework around or within the templates. Subsequently, the hard-template, in most cases silica, is removed with a strong base or acid solution such as HF or NaOH (**Figure 2.3**). For instance, CMK-3 (carbon mesostructured by KAIST)[112,113] has been synthesized as a replica of SBA-15, and CMK-8[112,114] with a structure of cubic Ia3d and rod-type from KIT-6.

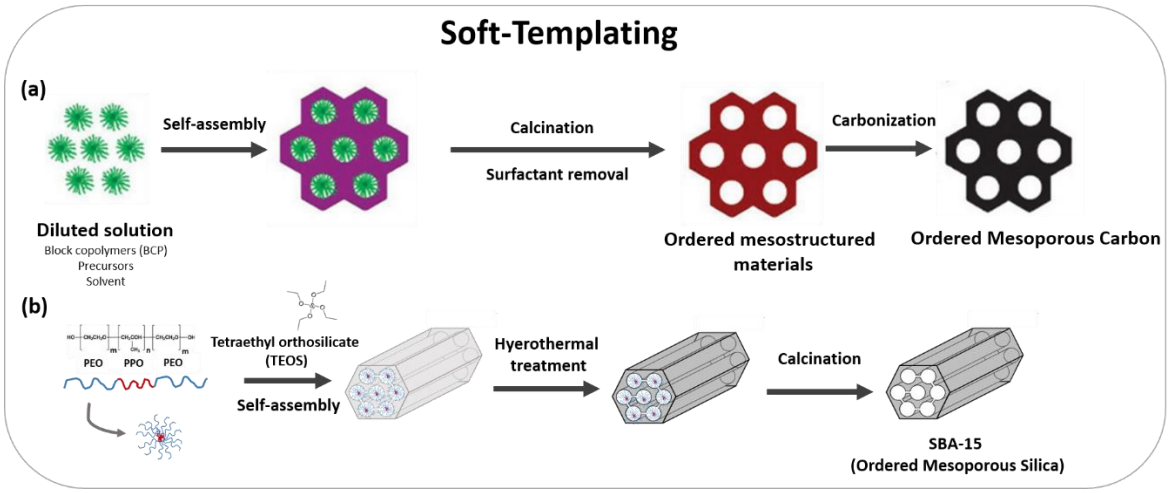

Figure 2.2 (a) Synthesis methods of ordered mesoporous carbon materials *via* soft- templating (adapted with a permission from reference [115]) and (b) the soft- templating procedure on the example of SBA-15.

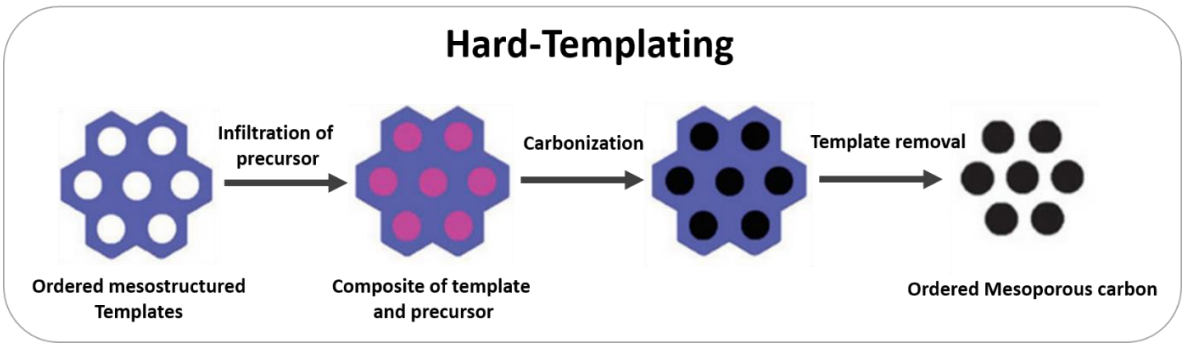

Figure 2.3 Synthesis methods of ordered mesoporous carbon materials *via* hard- templating (adapted with a permission from reference [115]).

Salt-templating using molten salts as a reaction medium is a suitable approach for obtaining a well-defined porous structure especially with micropores as well as mesopores. As its dictionary definition of 'a chemical compound consisting of an ionic assembly of cations and anions'[116] indicates, salt has quite a high solubility in water as ionic substances so templates can be removed by simply washing without harsh conditions and there is even a possibility to reuse these

substances directly for further salt-templating synthesis. A carbon precursor in the presence of the molten salts is condensed, resulting in a high specific surface area with small porosity corresponding to the cluster size of the salts.

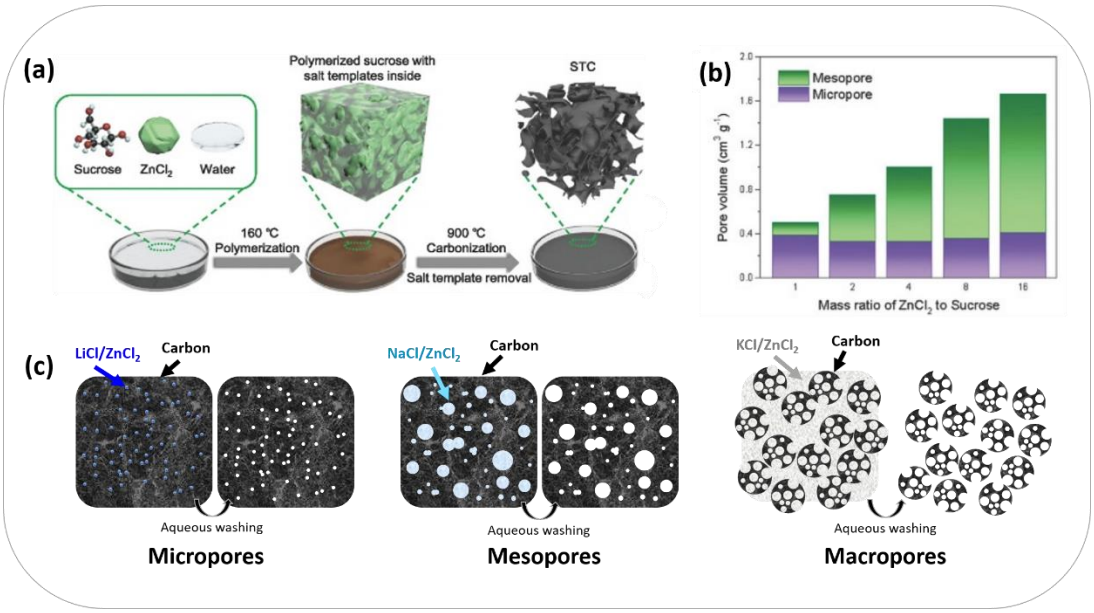

Figure 2.4 (a) Scheme of preparation of salt-templated carbons (STCs), (b) micro-/mesopore ratios in various STCs depending on the mass ratio of salts ($ZnCl_2$) and carbon precursors (sucrose) calculated based on the N_2 (at 77 K) and CO_2 (at 273 K) physisorption. (adapted with permission from reference (a,b)[57]), and (c) schematic illustration of porosity and morphology in carbon materials obtained from salt-templating by using various mixture of salts.[117]

The salt-templating method for the synthesis of porous carbon materials involves only three simple steps: a) mixing of the salts and carbon precursors, b) carbonization at a specific temperature with the carbon sources homogeneously immersed in the liquid salts, and c) removing the salts by water or diluted acid.[118] One of recent studies suggested the mechanism to generate the porosity in the resulting carbon materials, the carbon precursor is dissolved in molten salt, and then miscibility is formed, which is maintained during the whole carbonization process.[118] During

this process, the size and morphology of the pore are constructed depending on the size of the ion pairs and the clusters of salts as a template/porogen.

For the synthesis of porous carbon materials, salt-templating is especially attractive for the following reasons: i) controllable structures can be achieved by various operating parameters (e.g., kind of salts, carbon precursors, ratio of salt to carbon sources, heating temperatures, and additives), ii) possibility to use a wide range of the carbon sources including biomass, iii) possibly high yield of the resulting carbon materials, iv) additional self-activation by the emitted gas from the reactants, and v) sustainable synthesis due to the recycling of salts.[118]

Zinc chloride ($ZnCl_2$), known as one of the most widely used salts, has a relatively low melting point of 280 – 310 ℃ and boiling point above ~ 450 ℃.[119,120] $ZnCl_2$ has been known not only as an acid catalyst in organic chemistry but also as a dehydration agent. It accelerates the dehydration of the carbon precursor at low temperature, promoting the formation of char and aromatization and thus resulting in a higher yield compared to other synthesis methods. The salts are sort of captured in the carbon precursor domains so that the pore structure during the carbonization at rather higher temperature is remained and can be opened when the salt is removed by water-based solutions.[118,121,122]

It has been shown that the micro/mesopores can be controlled by the volume of impregnated $ZnCl_2$ (e.g., salt templated porous carbon described in **Figure 2.4**a and **2.4**b) which is why this synthesis method has been recently named as “salt-templating” by Fellinger *et al.*[123] Regarding the control of pore structure, when a high salt/precursor ratio is applied, it is described as a sol-gel reaction and leads to interconnected meso/macropores structure while the microporosity is still generated inside of the particles from the nanoscopic clusters of the salts.[97,124]

The mixture of two or more salts can also generate different pore structures. The different ratio of salts affects the pore system as well. This mixture of salts can further lead to a lower melting point in comparison to individual salts, thus creating a minimum melting point (i.e., eutectic point) in each composition of salts.[125,126] For example, when $ZnCl_2$ and KCl with a melting point of 290 °C, and 770 °C, respectively, are combined to a salt mixture at a molar ratio of 0.54/0.46, this mixture has a melting point of 230 °C which is lower than the melting point of the individual compounds. Similarly, the porosity of carbon materials can be controlled by introducing different kinds of salts. The carbon materials synthesized by eutectic molten salts made from zinc chloride ($ZnCl_2$)/lithium chlorid (LiCl), has exclusively microporous structure reaching 1497 m^2 g^{-1} of specific surface area and 0.81 cm^3 g^{-1} of pore volume, while the potassium chloride (KCl)/zinc chloride ($ZnCl_2$) further generates a mesopore system with 2013 m^2 g^{-1} of specific surface area and a pore volume of 1.7 cm^3 g^{-1} (**Figure 2.4**c).[117,127]

In **Chapter 2.2**, an overview over porosity in carbon materials was given. Porosity is the first factor that should be considered when a porous carbon material is designed for a given application. In order to be used as a functional material, a sufficient surface area and pore volume is demanded to allow the guest species to find enough adsorption and reaction sites. Of course, a proper pore size needs to be adjusted depending on the size of the guest species. Thus, various synthesis methods for controlling pore structure, such as activations and templating were described. In order for porous carbon to be effective in various applications, the chemical structure of the pore walls is another important factor in addition to the porosity. By introducing specific bonding motives and heteroatoms on the porous carbon materials, it is possible to induce a specific “chemistry” towards the guest species which is essential in performing as a functional material.

2.3. Functionalization of porous carbon materials

Functionalization of carbon materials including graphene, graphite, porous carbon, and carbon nanotubes has widely attracted attention because it is a fascinating tool to improve the electronic properties of carbon and consequently modify their chemical properties. Among various strategies to achieve the charge modulation such as doping of heteroatoms, doping of metals, and introduction of defective sites, especially the doping of heteroatoms is a straightforward method to couple a carbon framework directly to electron acceptors/donors. In heteroatom doping, non-carbon atoms (e.g., N, B, S, O, P, F, Br, Cl) replace the carbon atom sites of the original carbon skeletons or they are introduced as surface functional groups.[128] One or multiple dopants can be selected based on their size or electronegativity. This allows the modification of electronic properties over a wide range.[129-132] For example, doping electron donor (n-type doping, e.g., nitrogen) and electron acceptor (p-type doping, e.g., boron) into a layer of graphene materials affects the band structure differently with unique shifts in the Fermi levels.[133,134] A volcano plot can be drawn with overpotentials or current density of carbon materials with various dopants, indicating that heteroatom doping can modify the electronic properties of carbon materials and implying the possibility of replacing the noble metal or metal-based nanomaterials.[135,136]

Nitrogen is the most widely used atom as a heteroatom dopant into carbon materials because it can charge the carbon positively or negatively carbon, enhancing the adsorption of anions or cations when it is incorporated into carbonaceous materials.[137] It has been found that nitrogen-containing carbon materials exhibit large capacity for acid gases, have high activity in oxygen reduction reaction, high capacities in supercapacitors, and can achieve high selectivity in gas separation and so on.[138-141] These changes in comparison to pristine carbon materials are becoming

possible due to the widely adjustable stoichiometric ratio of nitrogen and carbon which form stable covalent bonds due to their comparable atomic sizes.[27,142-145] Also, the conjugation between the lone-pair electrons of nitrogen and the π-bonds of carbon structures seems to generate tailored electronic properties when nitrogen is doped on the nanostructured carbons, though it still needs to be further studied to be fully understood.[146-148]

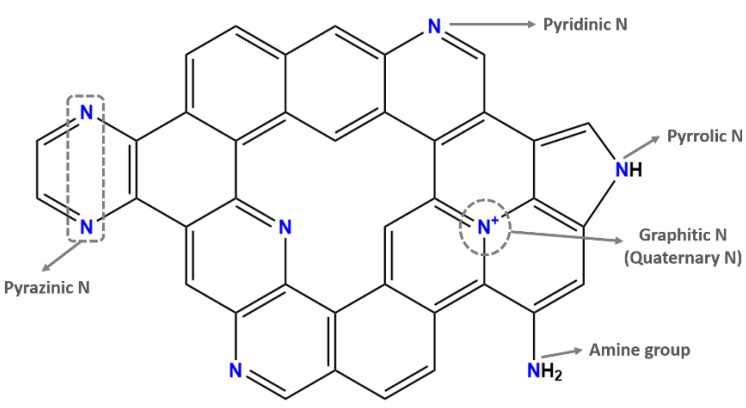

Figure 2.5 Scheme illustration of various nitrogen functionalities in nitrogen-containing graphitic carbons.

The doped nitrogen can be bonded to carbon in different forms, resulting in different electron density transfers. For instance, pyridinic N, and graphitic N which is sp^2- hybridized species substituting the carbon sites can be incorporated at the edges of structures, and in the middle of hexagonal rings of the carbon surfaces, respectively. The type of functional group and the amount of nitrogen depend on the precursor and the pyrolysis temperature, and among them, the graphitic nitrogen is known as a functional group obtained at the highest temperature.[149,150] Pyridinic nitrogen, which is generally known as a site to provide highly improved electrochemical activities, has low binding energies (~ 398.6 eV)[151] of N 1s electrons when characterized by X-ray

photoelectron spectroscopy (XPS)[152-154], whereas higher binding energies have been observed for other functional nitrogen groups such as pyrrolic nitrogen (~ 400.5 eV), graphitic nitrogen (~ 401.4 eV), and pyridinic nitrogen oxide (402 ~ 405 eV) [151,155] (**Figure 2.5**). Such heteroatoms play an important role in electrochemical reactions and especially in ORR.[156,157]

Meanwhile, materials consisting of carbon and nitrogen can be separated into two classes by the ratio of carbon and nitrogen: Nitrogen-rich compounds and nitrogen-doped carbon (C/N ≥ 1:1).[158] While nitrogen-rich carbons indicate a high nitrogen to carbon ratio (C/N ≤ 1:1, e.g., g-C_3N_4, C_2N_3, or C_3N_5), usually resulting from the thermal condensation of nitrogen-rich precursors, and shows totally new properties from bulk carbon structures such as superhardness or semiconductivity,[159,160] the functionalization of nitrogen-doped carbon that is most often obtained during direct synthesis or post-treatment of carbon materials in the presence of nitrogen-containing precursors at rather high temperature does not change but modifies the properties of the bulk carbon materials.[158]

In general, there are two different approaches to nitrogen-doped carbon materials: the post-treatment processing of heteroatom species on preformed carbon materials, and the direct *in-situ* synthesis from nitrogen-containing carbon precursors during the carbonization of the skeleton carbon materials. Various synthetic approaches to functionalize and therefore to change the atomic construction of the porous carbon materials by using nitrogen as an example heteroatom are introduced in the next chapters (**Chapter 2.3.1** and **2.3.2**).

2.3.1. Various approaches to synthesize heteroatom-doped porous carbon materials

2.3.1.1. The post-treatment processing on the porous carbon materials

Nitrogen-doped carbon materials can be obtained when a reagent is used as a nitrogen source. Examples of reagents include ammonia, which is most frequently used, urea, nitric acids, hydrogen cyanide, melamine, *N*,*N*-dimethylethanolamine, and polyaniline.[161-163] The basic principle of this method is that nitrogen-containing reagents are thermally decomposed and the nitrogen from the resulting species is doped into a preformed carbon material. When ammonia, for example, is subjected to specific carbon materials, ammonia decomposes into radicals such as $^{\cdot}NH_2$, $^{\cdot}NH$ so that the nitrogen functional groups are formed in between carbon atoms sporadically. Not only the atomic configuration but the porosity in materials can also be changed by the nitrogen treatment because of the possible etching effect of these radicals.[164,165] The nitrogen functional groups or the amount of doping are affected by various factors such as the oxygen contents in the starting materials, the activation of preformed carbon, the carbonization temperatures, and the process order of the preparation for the activated carbons.[166,167] For instance, Pietrzak *et al.* has reported pyrrolic-N and pyridinic-N are dominant functional groups when the precursor of carbon materials is exposed to the nitrogen sources, while the further surface nitrogen functional groups such as imine and nitrile are dominant when the treatment is conducted after the activation of carbons.[166] In addition, this doping strategy does generally lead to highly heterogeneous doping due to the chemically ill-defined structure of porous carbon materials.[168,169] Therefore, direct synthesis of nitrogen-doped carbon allows preparation of nitrogen species with more control.

2.3.2.2. The direct carbonization from nitrogen-containing carbon precursor

Well-defined ordered or crystalline materials (e.g., SBA-15, Zeolite 13X, or Zeolite Y) are used as templates to obtain nitrogen-doped porous carbon. The nitrogen-containing carbon precursors such as diaminobenzene, acetonitrile, polyacrylonitrile, polypyrrole, and pyrrole exhibit ordering replicated from selected templates.[170-172] Indeed, the resulting nitrogen-doped porous carbon synthesized from acetonitrile as a carbon precursor and zeolite 13X or zeolite Y as template exhibits a high amount of nitrogen content (5 – 8 %), preserving the high porous structure (~ 1920 m^2 g^{-1} of surface area and ~1.4 cm^3 g^{-1} of pore volume) *via* chemical vapor deposition even at 550 – 1000 °C.[170] The nitrogen sources after physical and chemical activations are also used to synthesize nitrogen-doped porous carbons.[171,173] These activation mediums convert the precursors from the polymer into complexes so that the heterogeneous functionalities are distributed throughout the carbon materials.[174] Further detailed examples will be described in **Chapter 2.3.2**.

2.3.2. Electronic properties of heteroatom-doped carbon materials

As mentioned earlier, by introducing heteroatoms into the carbon materials, properties such as resistance against the high temperatures or oxidations can be obtained. The reason for that is the polarization of the carbon atoms in the presence of an element with a different electronegativity. The resistance against oxidation, which is defined as 'nobility', can be quantified using ultraviolet photoelectron spectroscopy (UPS) by measuring the specific energy it takes to emit electrons out of a surface. It can be similarly determined in electrochemistry by measuring the driving voltage required to donate/accept electrons.[175] When these data are presented in a standard electrode potential related to reference hydrogen electrode (RHE; $E^0_{RHE} = 0$), it shows that each element has

a certain potential position (**Figure 2.6**). The lower, i.e., the more negative potential, the element is placed, the more likely it is to emit electrons (e.g. E^0 (Li) = − 3.1V is close to − 4.4 V at which emission of electrons even to vacuum happens spontaneously).

$$E = E^0 + \frac{RT}{nF} ln \frac{[Ox]}{[Red]} \tag{2.1}$$

$$\Delta G^0 = -n \cdot F \cdot \Delta E^0 \tag{2.2}$$

The Nernst equation (**Equation (2.1)**) that calculates the electrochemical potential according to the concentration of the oxidation/reduction species can be combined with **Equation (2.2)**, which acts as a bridge between the Gibbs-free energy and the standard potential, so that the thermodynamic scale can be directly connected to a potential voltage scale. That is, a substance with thermodynamically positive free energy will have a negative electrochemical potential with respect to E^0_{RHE} = 0, and vice versa, aside from any kinetic hindrance. From this point of view, any material above the potential of oxygen with E^0 (O_2) = 1.23 V, e.g., gold with E^0 (Au) = 1.8 V, is not oxidized in the presence of oxygen, which means it is not combustible or "noble".[175] That is, the materials at more positive potential than the oxygen is in an electron-deficient state so they tend to show high affinity to electrons and therefore accept them. Certain materials have very high oxidation strength, such as the Fukuzumi dye (E_{HOMO} ≈ 2.1 V), nucleobases (E_{HOMO} (adenine)≈ 1.6 V, E_{HOMO} (thymine) ≈ 2.1 V), ionic liquids (E_{HOMO} ≈ 5.9 V), solid state organic materials (E_{HOMO} ≈ 1.6 ~ 2.1 V).[176-180]

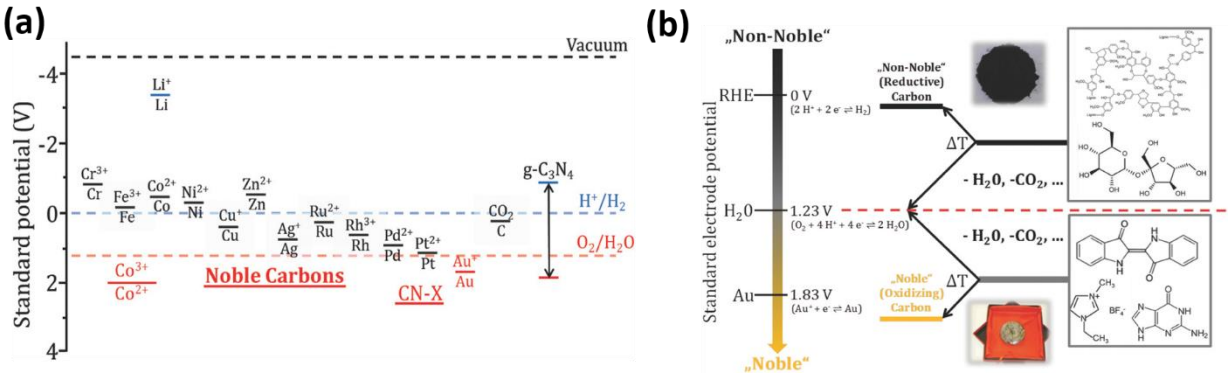

Figure 2.6 (a) Electrochemical potentials for some known materials and (b) two reaction paths of carbonization for non-noble (reaction to upwards) and noble carbons (reaction to downwards) (adapted with permission from reference (a,b)[175])

Carbonaceous materials can also have high potential and are not easily oxidized. The range of possible work functions of carbon materials is widely spread and can even exceed 2 V. However, in order to obtain oxidation-stable carbon materials, there are some things to consider.[175] When carbohydrates (e.g., cellulose) are carbonized, stable water molecules are eliminated, and thus the internal energy of the resulting materials is higher than before, according to the first law of thermodynamics (**Figure 2.6**). This causes the electrochemical potential to move to lower values. Thus, a carbon material non-resistant to oxidation is obtained from such precursors. However, there is another reaction path to get more noble resulting materials. When starting from least oxidizable precursors (e.g., nucleobases, ionic liquids, or indigo), the elimination of molecules such as H_2O, CO, CO_2, or NH_3 lets the internal energy of resulting product to move downwards, i.e., to more positive potential. This is also the case for the direct carbonization for many of the nitrogen-containing carbon precursors previously mentioned in **Chapter 2.3.2.2**. As a result, these carbon materials are further resistant to oxidation. In short, it results in non-noble carbon materials

when the carbonization is started from easily oxidizable precursors, while noble carbon materials are able to be obtained when the starting materials are non-oxidizable precursors.[175] From the thermodynamic point of view, the deductions of the resulting carbon materials are as follows: a) energetically optimized aromatization or aromatic packing, b) increased specific cohesion energy such as enhanced polarization than the precursors, and c) optimized incorporation of heteroatom species (e.g., N, O, or S) at the favored positions in which each atoms have optimal distance due to band confinement.[181]

2.4. Porous carbon materials on various applications

Generally, gas separation proceeds by passing the gas mixture through the adsorbents and then following up with desorption of adsorbed species to be separated. The regeneration process, which is one of the most important factors determining the energy needed for a given gas separation process, is often done by heating the adsorbent to desorb the adsorbed gas (in thermal swing adsorption; TSA), or by lowering the partial pressure of the adsorbed substances (in pressure swing adsorption; PSA).[182] The equilibrium and continuous contact of the gas and adsorbent determine the separating power of the adsorbent, which means it is essential for the adsorbent to not only have high adsorption capacity and selectivity to the gases but also favorable mass transport kinetics.[183] That is why a high surface area and sufficient size of pores are needed within the adsorbent materials. The mechanisms of the adsorptive gas separation usually include these possibilities: a) certain gas species are allowed to enter into the pores because of the exclusive pore size and shape, also called the molecular sieving effect, b) certain gas components have preferential adsorption depending on their interactions between adsorbate and surfaces of adsorbents, called the thermodynamics equilibrium effect, c) certain gas components enter faster over others due to their higher diffusion rate, known as the kinetic effects, and d) some light molecules have the quantum effect in a narrow micropore so that separated adsorption is allowed, called the quantum sieving effect.[182] Among them, the equilibrium effects are determined by the surface characteristics of the adsorbents and adsorbates (including but not limited to polarizability, magnetic properties, dipole/quadruple moments). For the kinetic effects, precisely controlled pore structure need to be designed in order to separately capture the certain gas components from the

mixture gases in which undesirable component (e.g., oxygen) diffuses faster than target components.

Crystalline microporous adsorbents such as zeolites and MOFs have been the most well-known substances for gas separations and purifications in the past few decades.[184-186] ASRT 5A zeolite, which is manufactured by Allied Signal and studied by the group of Lila *et al.*, for example, is suitable to remove CO_2 in spacecraft cabins even at high temperature and pressure up to 250 ^{o}C and 1000 Torr, respectively.[187] Due to their well-defined crystalline and thus uniform pore structure ranging from 0.3 to 1 nm, zeolites have the ability to separate specific molecules via the molecular sieve effect. In general, three factors of the properties in these adsorbents affect gas separation and adsorption, i) the cations present, ii) the structure and composition of the frameworks, and iii) the purity of the zeolites.[188] This can be described by the general chemical formula of $M_{2/n}OAl_2O_3{\cdot}xSiO_2{\cdot}yH_2O$, where M, x and y indicate the cation M with valence n, a natural number 2.0 or more, and the moles of water in the voids, respectively,[189] also expressed as $[(M_{1-x}^{2+}M_x^{3+}(OH)_2))^{x+}{\cdot}(A_{x/n}^{n-}{\cdot}mH_2O)^{x-}]$, in which M^{2+}= Ni^{2+}, Zn^{2+}, Cu^{2+}, Mg^{2+}, Mn^{2+}, M^{3+} = Al^{3+}, Fe^{3+},Cr^{3+},and A^{n-}= SO_4^{2-},NO^{3-}, CO_3^{2-}, Cl^-, OH^-, etc. There are numerous combinations of these materials and the mechanism of the gas separation varies depending on their composition properties (e.g., contents of cations, type of anions, water content, and temperature).[188,190] However, there are drawbacks in the applications of zeolites. The gas adsorption is impeded in the presence of vapor which reduces the adsorption capacity over time. Because of the high adsorption enthalpy of CO_2, it demands relatively high temperature (ca. 135 °C) for the desorption of the gas components.[191-193] These challenges led to the demands for the adsorbents with a different range of pore size and surface properties.

MOFs are another class of candidates for gas capture and separation, especially for their possibility to selectively adsorb CO_2.[182,194] Unlike zeolites where pores are confined by the inelastic tetrahedral oxide skeletons, MOFs can easily modified and optimized by tuning the building blocks from a variety of choices of metal-based clusters and organic linkers, followed by a facile self-assembly reaction of metal ions and organic molecules forming networks with exceptional high porosity.[19,195,196] The whole MOF framework consists of coordinated bonds and relatively weak interactions (e.g., hydrogen bonding, π–π stacking, and van der Waals interactions) which render certain MOFs (which are usually categorized as flexible MOFs) flexible in structure during adsorption.[182] Tens of thousands of different MOFs have been synthesized with surface area, pore size and electronic properties all precisely controlled to suit their needs.[182,197] However, it still has limitations with difficulties in gas separation, low stability in the presence of water, and low durability at high temperatures.[198]

Porous carbon materials, such as activated carbons or templated carbons, have been widely studied recently because of their high thermal/chemical stabilities, resistance against water, incredibly low cost, and sustainable synthesis using various carbon sources.[4,199] Their adsorption properties can be enhanced when nitrogen or heteroatoms are incorporated as this changes the electric properties on the surfaces. High specific surface areas/pore volumes, various distribution of pore sizes, and proper interactions with adsorbate components make porous carbons a promising candidate to substitute other porous materials.[198]

Two different possible applications of carbons are introduced in the following chapters. In **Chapter 2.4.1**, porous carbon's selective gas adsorption and separation ability for CO_2 are

represented. In **Chapter 2.4.2**, the application in supercapacitor electrodes as electrochemical energy storage systems will be described.

2.4.1. The selective CO_2 adsorption over N_2

As chemisorption requires high energy for regeneration and exhibits vapor sensitivity, the physisorption of CO_2 gas in porous materials is a more promising and attractive approach due to its lower adsorption enthalpy, higher reversibility, and the lower energy needed for regeneration. There are particular requirements to materials to be used as adsorbents in CO_2 adsorption: a) high selectivity over the other gas species from the mixture of gases, b) high adsorption capacity for CO_2 in the atmosphere of adsorption as well as c) easy regeneration with low pressure and temperature swings, d) high resistance against moistures/impurities, and e) fast adsorption kinetics in relation to the contact time with the gas mixture.[4]

Removing CO_2 from air demands high selectivity of CO_2 over N_2 and/or O_2 because of its low concentration at around 400 ppm. The selectivity of CO_2 over O_2 (CO_2/O_2) and the selectivity of CO_2 over N_2 (CO_2/N_2) can be calculated form simple volumetric physisorption experiments by using the ideal adsorption solution theory (IAST).[68]Oxygen at cryogenic temperatures is dangerous to handle and as the selectivity of CO_2/O_2 and CO_2/N_2 are usually comparable, CO_2/N_2 is generally used as a reference.[4] In order to achieve highly selective CO_2 adsorption, two important parameters need to be met. One is the aspect of thermodynamic principles where the polarizability is the most important issue, and the other is the aspect of kinetic principles, in which the pore size is main crucial modulation. In short, when designing a porous carbon material for selective CO_2 adsorption, not just the porosity for the CO_2 capacity and the diffusion of the adsorbates, but the surface

chemical composition for easy regeneration and CO_2 capacity should also be considered (**Figure 2.7**a).

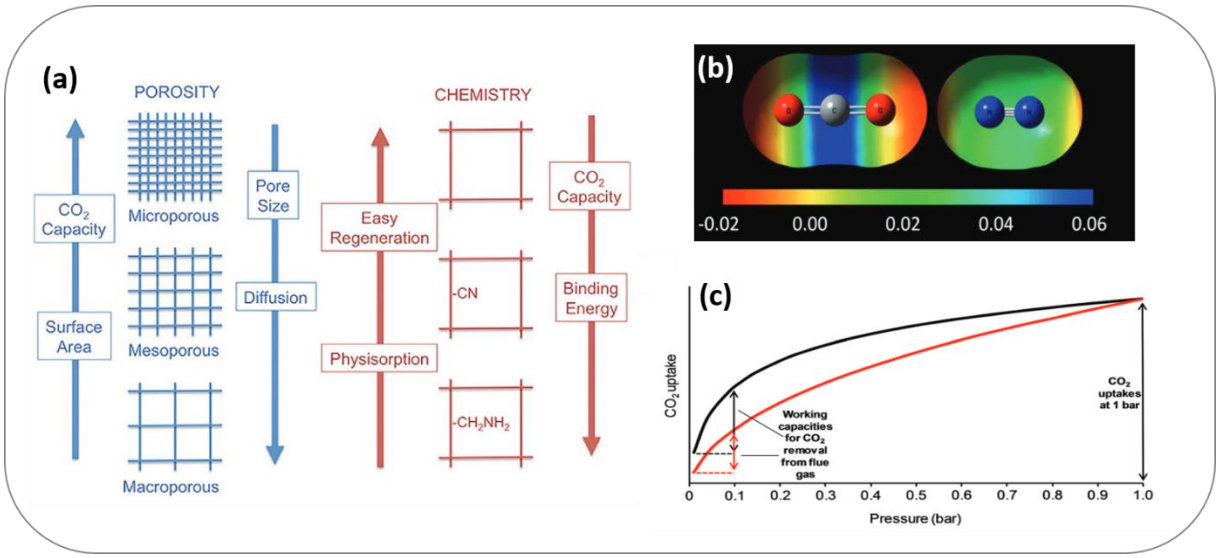

Figure 2.7 (a) Scheme of porosity and surface chemistry for optimization of sorbent, (b) electrostatic potentials for CO_2 and N_2 mapped against the iso-electron density value of 0.005 a.u., and (c) representative CO_2 adsorption isotherms of 2 materials with similar uptake at 1 bar but different CO_2 capacity at low partial pressure (i.e., different gaps of CO_2 uptake between adsorption and regeneration conditions). (adapted with permission from reference (a)[200], (b)[201], and (c)[4])

While the interaction of adsorbate-adsorbate is mainly predominant in high pressure conditions, the interactions of adsorbent-adsorbate, is dominant at low pressure or low concentration of CO_2. That is, the adsorption enthalpy is a main parameter, and it can be made stronger by introducing yet stronger interactions (e.g., dipole-dipole interactions, or donor-acceptor couples). Considering the van der Waals interaction as opposed to chemical bonds is dominant in physisorption, the adsorption enthalpy is correlated to the polarity of the surface of adsorbent materials. The polarizability and the quadrupole moment of CO_2 are 26.3×10^{-25} cm^3 and 13.4×10^{-40} C m^2,

respectively, while N_2 have slightly lower values of 17.6×10^{-25} cm^3 and 4.7×10^{-40} C m^2, respectively (**Figure 2.7**b).[4] These slight differences of the adsorbates give the adsorbents with more polar properties the ability to differentiate the guest molecules. Therefore, it has been often seen that porous carbons (i.e., nitrogen or heteroatom doped carbons) with increased surface polarity have greater affinity toward CO_2 than pristine carbon .[202,203] For examples, as the nitrogen content increased from 3 wt.% to 6 wt.%, the CO_2/N_2 selectivity increased in the best case from 10 to 100, indicating the functional groups of nitrogen are playing an important role in selective affinity of CO_2.[204]

Meanwhile, in the CO_2 physisorption, a high uptake at a partial pressure in the range of 0.1 – 0.2 (i.e., more convex or upwards shape of curves in isotherms) is usually caused by specific chemical interaction preferred for better selectivity because in the van der Waals interaction, the adsorption enthalpy is does not contribute to selective adsorption (**Figure 2.7**c).[4] As the minimal heat of adsorption around 19.5 kJ mol^{-1} is demanded to take in a gas at 400 ppm conditions and the thermodynamic limit due to the adsorption enthalpies of the other species is considered, an optimal heat of adsorption (Q_{st}) is ~35 – 50 kJ mol^{-1}.[4,200] Weak binding causes low capacity when Q_{st} is below 35 kJ mol^{-1}, while regeneration energy becomes too energy intense when Q_{st} is above 50 kJ mol^{-1}.[200] Recently, a breakthrough MOF material, SIFSIX-3-M (M=Zn, Cu), synthesized using unsaturated metal, pyrazine units, and silicon hexafluoride has been reported. It has comparable structure with the substance responsible for CO_2 fixation in plants (i.e., Rubisco; Ribulose-1,5-bisphosphatecarboxylase/oxygenase) with an incredibly high CO_2/O_2 selectivity of ~ 1500, showing enormously high CO_2/N_2 selectivity of 2000, heat of adsorption for CO_2 of around

52 kJ mol^{-1}, which is between the chemisorption and physisorption, but still allowing for reversible CO_2 adsorption.[24]

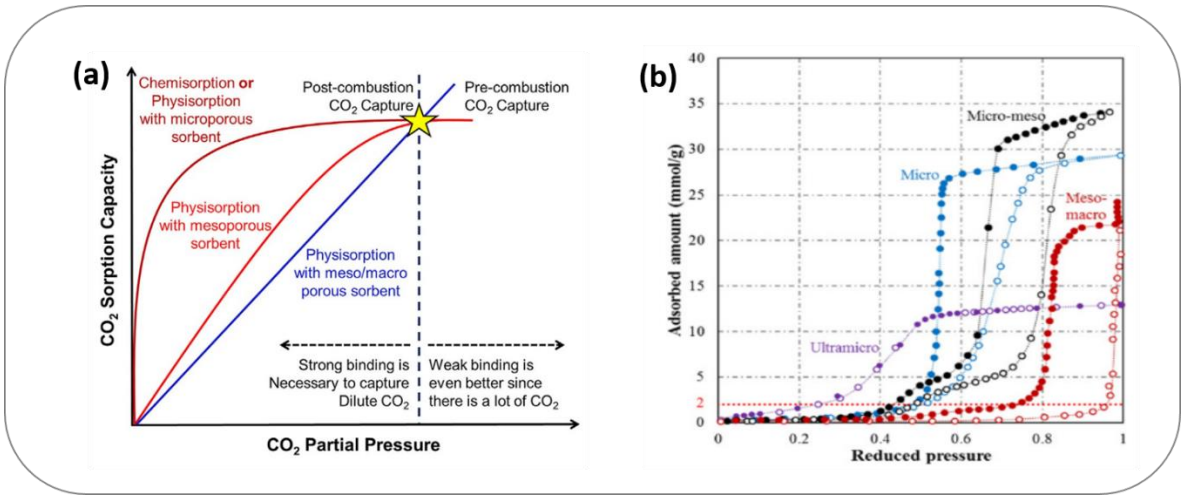

Figure 2.8 (a) CO_2 isotherms from different types of pore structure of sorbent, and (b) water isotherms from different types of pore structure carbons. (adapted with permission from reference (a)[200], and (b)[205])

The kinetic principle is related to the controlling of pore size and their modulations. The ultramicropores (pore size of 0.5 – 0.7 nm) are geometrically more favorable for CO_2 adsorption and thus the optimal pore size compared to supermicropores (0.7 – 2 nm) and mesopores (> 2 nm).[206-208] That means the pore size itself can affect the CO_2 adsorption capacity as well as the hydrophilicity (**Figure 2.8**). Furthermore, as the kinetic diameter of CO_2 (0.33 nm) is relatively smaller than that of N_2 (0.364 nm) and O_2 (0.345 nm), a material with pore size of larger than CO_2 but smaller than N_2 or O_2 can exclude the bigger molecules, which is called 'molecular sieving'. In this approach, however, H_2O remains a problem as it not only has a smaller kinetic diameter of 0.265 nm but also a higher quadrupole moment of 3.336×10^{-30} C m^2 so that any effort to improve

the adsorption of CO_2 automatically leads to the enhanced adsorption of H_2O.[4,209] The kinetic aspects from pore diffusion need to be considered because of its influence on the rate of adsorption. In other words, when the pore size of the material is the same or close to the kinetic diameter of CO_2, it would result in overall sluggish adsorption. There have been reports solving this challenge by introducing larger mesopores or macropores.[204,210] Although the larger pores can improve transport and diffusion, it eventually reduces the portion of micropores for CO_2 adsorption, and therefore this trade-off must be considered when designing a porosity structure in materials for selective CO_2 adsorption.

2.4.2. Capacitors with nitrogen-doped porous carbon in aqueous electrolyte

Supercapacitors are energy storage devices which store electrochemical energy by using adsorption mechanisms or fast redox reactions of ions on the electrodes with high specific surface area (**Figure 2.9**a).[211] They are well known for their high power density, long life cycle, short charge and discharge time, and broad range of possible operating temperature. Also the electrosorption mechanisms allows highly reversible storage compared to batteries which demand the diffusion of ions into the bulk of the electrodes. Electrochemical double later capacitors (EDLCs), one of the categories of supercapacitors, store the electric charge through physical adsorption and desorption of ion at the interfaces between the electrodes and electrolytes (**Figure 2.9**b).[211,212]

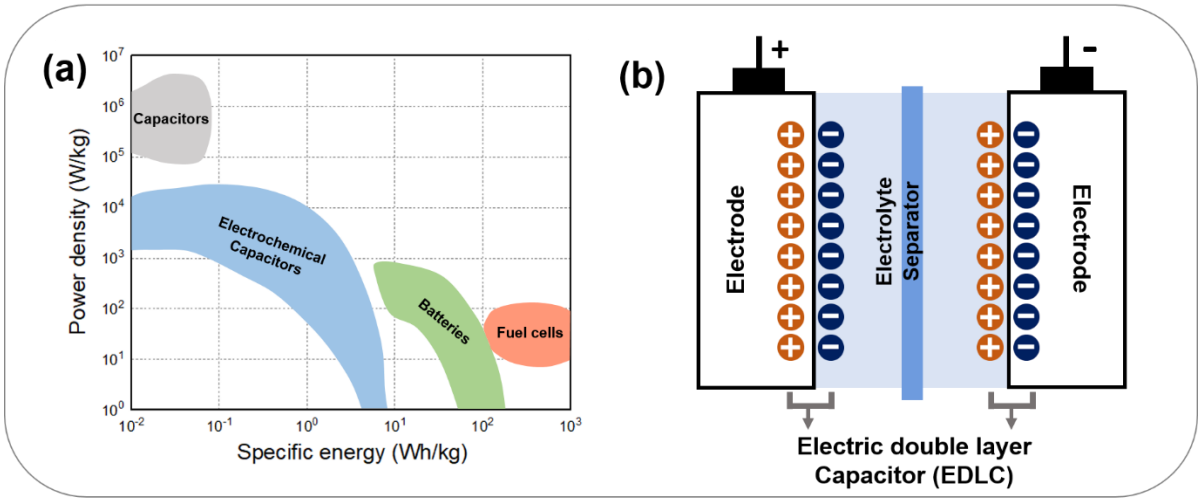

Figure 2.9 (a) Specific power against specific energy for various electrical energy storage devices and (b) schematic of an electric double layer capacitor.

Porous carbons are promising materials for the electrodes of EDLCs due to their numerous advantages, such as abundance, thermal/chemical stability, a low manufacturing cost, an environmental friendliness. High specific surface area of porous carbon materials is one of the most important properties for EDLCs, as the capacitance are basically obtained by the Equation (2.3) where A (unit in m^2) represents the ion-accessible surface area of the electrode material (ε_r, ε_0, and d represent the electrolyte dielectric constant, the permittivity of vacuum, and the effective thickness of the EDL, respectively).[212]

$$C = \frac{\varepsilon_r \, \varepsilon_0}{d} \times A \qquad (2.3)$$

2.4.2.1. Crucial factors for electrochemical storage on porous carbons

As mentioned earlier, the principle of electrochemical energy storage on the porous carbon is based on electrosorption. Therefore, the specific surface area and the pore size distribution play important roles for the capacitance. Theoretically, the capacitance should increase as the specific surface area increases, but this is not always the case. For example, according to the report from group of Gamby *et al.*, only 44% of the BET surface area of a carbon material with surface area of 920 m^2 g^{-1} contributed to the capacitance, recording only 80 F g^{-1} compared to the theoretical 182 F g^{-1}.[213] One explanation would be that BET surface area is usually measured by specific probe gases, such as N_2, Ar, or CO_2, and the measured pores cannot be used for energy storage due to the mismatch occurring when the probe gases are smaller than the size of the ion of the capacitor system. Even though high surface area has to be considered to improve the capacitance, a balance between the factors is required because an excessive increase of surface area could rather lower the density of the materials and the volumetric specific capacitance.[212]

Pore sizes and their distribution are also crucial for ion and charge transport. While some studies suggested that the pores smaller than the solvated ions cannot contribute to the capacitance, newer findings show that materials with rather narrow micropores below 1 nm in size (e.g., carbide-derived carbons; CDCs) have increased capacitance because the distorted solvation shells allow the center of the ions to be closer to the wall of pores.[71,72,212] The effectiveness of such so-called sub-nanometer pores for the capacitance is improved by the ion desolvation effects in which pores with reduced size only accept the desolvated ions.[214,215] In general, when designing porous carbon materials for electrochemical energy capacitors, not only the micropores for the higher capacitance but also the broader pore channels for the kinetically fast ion transfer need to be considered.

As the introducing of heteroatoms into the porous carbon materials modifies the electronic properties of the materials, it can be concluded that heteroatom doping affects the electrochemical performance. Nitrogen in carbon materials especially can provide electroactive sites as electron-donor species, and improve the polarity and wettability of surface as well as the electrical conductivity by modifying the valence electron orbital energy levels of the surrounding carbons. A recent study has reported that area-normalized capacitance increased up to 22 uF cm^{-2} when nitrogen-doped carbon materials (here activated microwave expanded graphite oxide; a-MEGO) were used compared to carbon without nitrogen-doping with only 6 uF cm^{-2}.[216] A nitrogen-rich carbon with 6.05 wt % of nitrogen exhibited a highly enhanced capacitance of 392 F g^{-1} at 1 A g^{-1}, and 222 F g^{-1} at 20 a g^{-1}.[217] Also, oxygen functional groups (e.g., carboxyl, hydroxyl, and carbonyl) are generally known to improve the wettability of surface and the capacitance of supercapacitors in aqueous electrolyte system. It has been shown that porous carbons synthesized by pyrolysis of seaweed with oxygen contents of 10 – 15 % revealed electrochemical performances where both of the oxygen functionalities on the surface and the pH of the electrolyte affected to the stable potential window as well as the capacitance.[218]

The type of electrolyte plays another important role in addition to the properties of the electrodes for the capacitance. Each electrolyte influences the adhesive of the electrode particle, charge conduction, and ion supplementary. A wide range of voltage window, low resistance, high electrochemical stability, and low toxicity are required for the electrolyte.[219] The electrolyte for an electrochemical device is largely divided into aqueous electrolytes (e.g., Na_2SO_4, H_2SO_4, or KOH) and an organic electrolyte (e.g., acetonitrile, or propylene carbonate). Although the latter have the advantage of having a high voltage window up to about 4 V, they show drawbacks such as high

resistance and moisture sensitivity. Therefore, there are many interests in aqueous based system due to its lower cost, non-flammability, higher ionic conductivity and low resistance, safety, and stability when exposed to air.[219] Furthermore, as mentioned above, the heteroatom doped carbon materials are only beneficial in aqueous electrolyte as the enhanced electrolyte wetting is typically not a critical issue inorganic electrolyte systems.[212,220]

2.5. Outline

Nanoporous carbon is a promising solution to modern society's biggest problems – including air pollution and the lack of energy storage. Despite intense research, there is still much more to be learned about the structural, physical, and chemical properties of porous carbons in order to be utilized in a wider range of applications. In particular, the correlation between the adsorption of certain substances and the properties of pore size of carbon materials needs to be studied in order to understand the mechanism of adsorption of specific substances on carbon surfaces (**Chapter 2.2**). In addition, further research is necessary to enhance the 'chemical function' of porous carbon materials through surface functionalization (**Chapter 2.3**). Thus, the aim of this dissertation is to broaden the fundamental knowledge of porous carbons materials based on the understanding of the atomic structure of the pores and determine the application of those properties in various physical and electrochemical fields (**Chapter 2.4**).

In this context, the synthesis of sp^2-conjugated, heteroatom-rich, "carbonaceous" materials from easily accessible raw materials using abundant salt templates will be presented (**Chapter 3.1**). By controlling the salt template which acts as a pore stabilizer during carbonization, the differences in the pore structure and the atomic construction of the materials during carbonization can be determined, and furthermore the effect of structure and chemical properties on synthesis can be shown. The performance of heteroatom-rich carbon materials will be further investigated in different adsorption applications based on their architecture and electronic properties (**Chapter 3.2**). The modified pore and atomic structures by changing the carbonization temperature influence on the adsorption properties in the gas adsorption such as CO_2 and H_2O as well as an aqueous electrolyte based electrochemical energy storage. In **Chapter 3.3**, another set of sp^2-based carbon

nanomaterials obtained from molecular precursors (denoted as "HAT-CN") with stoichiometry close to the ideal C_2N will be investigated. Conducting carbonization under vacuum and investigating the adsorption of various gases of varying sizes gives insight into the previously-unknown pore formation mechanism of HAT-CN.

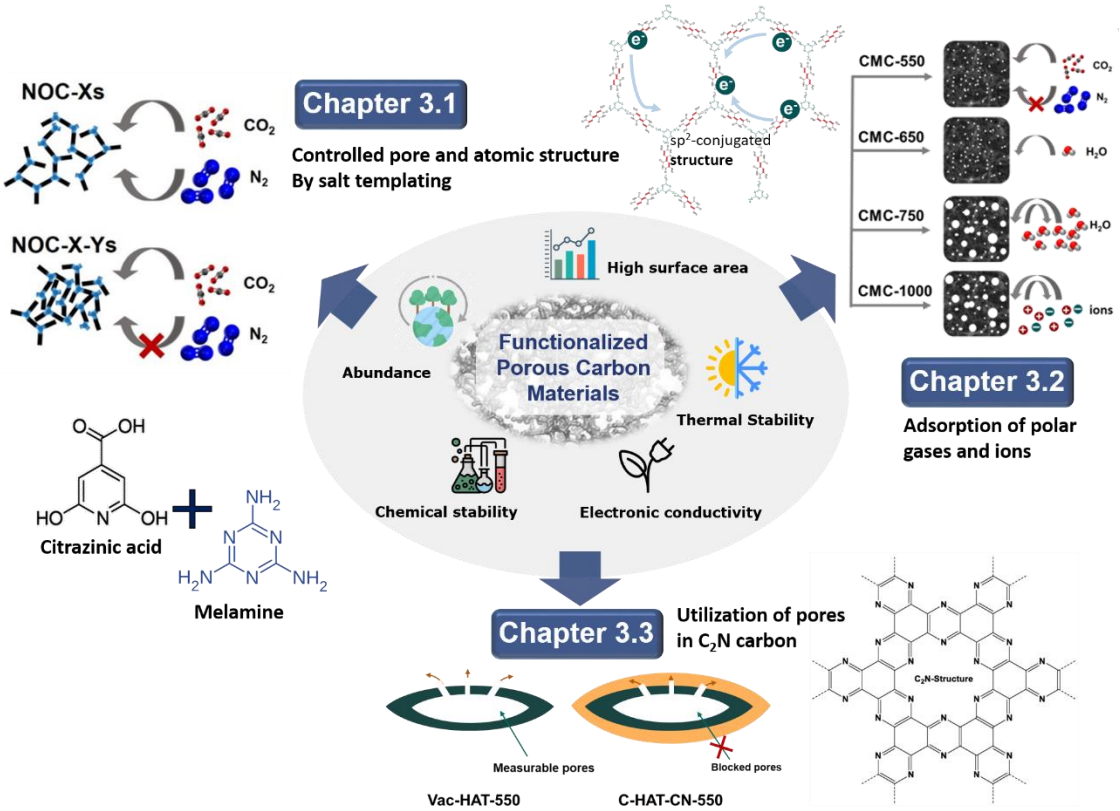

Figure 2.10 Graphical overview of the functionalized porous carbon materials in this thesis.

3. Results and Discussions

3.1. Controlling pore size and pore functionality in sp^2- conjugated microporous materials by precursor chemistry and salt templating*

3.1.1. Background and state-of-the-art

Porous carbons are crucial in many applications of modern science and industry such as water and air purification, catalysis, gas separation, and energy storage/conversion due to their high chemical and thermal stability, and in particular due to the possible combination of electronic conductivity with high specific surface area (**Chapter 2.1**).[25-30] All of these applications are related to adsorption processes, and precise control over the origin and strength of interaction between carbon and the surrounding phase mixtures is needed. This is of particular importance when high selectivity between a target molecule and the medium is desired.[48,145] Different templating methods towards such materials have been developed to achieve a certain control over the pore architecture and pore surface chemistry, and by that over the strength of adsorption of a given fluid (**Chapter 2.2**).[221,222]

Salt-templating into which a temperature-stable ionic compound is present during carbonization, is one strategy for the introduction of porosity which is also described in **Chapter 2.2.1.2.**[57,117,223] It is particularly attractive as it only demands abundant and potentially reusable, simple inorganic salts as pore-forming agents. No amphiphilic molecules or nanostructured inorganic materials are

* This chapter is adapted with permission from the original paper published by the author of this thesis as: Sol Youk, Jan P. Hofmann, Bolortuya Badamdorj, Antje Völkel, Markus Antonietti, Martin Oschatz, "Controlling pore size and pore functionality in sp2- conjugated microporous materials by precursor chemistry and salt templating", *Journal of Materials Chemistry A,* **2020**, 8, 21680

required and the salts can be removed by simply washing with water or by evaporation during carbonization.[224] In addition, $ZnCl_2$ can also catalyze reactions between molecular carbon precursors, which can decrease the necessary temperature to induce condensation.[225,226] Carbon materials with well-defined porosity can be produced by this method and the pore structure can be controlled by changing the amount, type, and mixture of salt template used, using mixtures of salts, varying the salt content, or by changing the carbon precursor.[123,227]

Control over pore structure is meanwhile rather elaborated, while the second key property of carbon materials in adsorption processes, chemical surface functionality, is still difficult to access. This is mostly due to the involved high temperature processes and/or consecutive etching steps ("activation") to increase porosity which however removes functionality (**Chapter 2.2.1**). The only effective tool left is the doping of carbon materials with heteroatoms such as nitrogen and oxygen by appropriate choice of precursors. Such doping can significantly change the polarizability and can even lead to adsorption properties which are rather typical for inorganic materials such as metal-organic frameworks or zeolites (**Chapter 2.3.2**).[18,129,163,228-231] Increased polarizability, but also more specific interactions such as acid-base character or hydrogen-bridge donor/acceptor sites increase the binding energy between pore walls and a given adsorbate. In consequence, high isosteric heats of adsorption of more than 50 kJ mol^{-1} are often observed in carbon dioxide or water adsorption on such heteroatom-doped carbons.[18,175,204,232,233] Physical adsorption, i.e. van der Waals binding between adsorbents and adsorbate, is proportional to the increase of polarizability of the two partners. In other words, stronger binding of all molecules can be expected when moving to a more polar carbon, but not higher selectivity. For that reason, optimization of physisorption is restricted, as optimization of polarizability does not sufficiently

increase the interactions to handle the exciting binding and separation problems – especially when the entropy contributions to the free energy of adsorption are considered which are becoming more influential at higher temperatures. Values of 50 kJ mol^{-1} imply that there is indeed a significant contribution of chemical interaction (i.e., chemisorption) in the process, and this part is different for different target molecules. To maximize this difference for a given problem, a defined atomic construction of the pore surface is needed.[175]

From this it can be concluded that the potential of heteroatom-doped carbon materials can only be fully utilized in a given application when the surface chemistry and the pore structure can both be adjusted. The former can be achieved by using molecular precursors for carbon synthesis which already contain heteroatoms in a desired specific bonding motive and can undergo controlled condensation towards an extended structure with defined atomic construction (**Chapter 2.3.1**).[234] Considering possible scalability of this approach, precursor molecules should be abundantly available and free of complicated chemical synthesis procedures. Regarding introduction of functionality on top of porosity in such heteroatom-doped carbons, salt-templating is an attractive method as well. Interaction with the salt phase locates interactive and the later pore surface, and the interaction energy with the salt phase (mostly the chosen metal ions) stabilizes them against thermal decomposition. This is why indeed salt-templated materials show a systematically higher heteroatom content than similar products made with classical templates.[127,235,236]

Choosing precursors in a rational fashion, pore size and pore functionality can be controlled by "edge termination", i.e. not only providing a meaningful, directed condensation chemistry, but at the same oxygen and nitrogen functionalities terminating the growth at the edge of the as formed 1d- or 2d structures can be inserted (**Chapter 2.3.1**).[237] Most of the edges will show up as pore

surface in the final covalent material, while only a minor fraction is buried within the covalent walls of the porous system. The efficiency of this process is again controlled by the interaction with the salt phase.

In this chapter, the feasibility of these concepts by the synthesis of supermicroporous covalent, sp^2-conjugated materials with high heteroatom content from a mixture of citrazinic acid and melamine in which heteroatoms are already bonded in specific motives are illustrated. $ZnCl_2$ is used as potentially reusable salt template. By controlling the removal procedure of the salt-template and the condensation temperature, the role of salts in the formation of porosity and as coordination sites for the stabilization of heteroatoms is proven. A high amount of nitrogen of up to 20 wt. %, oxygen contents of up to 19 wt.%, and a high CO_2/N_2 selectivity with maximum CO_2 uptake at 273 K of 5.31 mmol g^{-1} is achieved. The presented materials represent by the applied synthesis tools a new class of heteroatom-lined carbons with extended performance, while of course heteroatom contents of the order of the carbon content forbid the notation “doping” and indicate the presence of a new type of heterogeneous sorption material.

3.1.2. Nitrogen- oxygen- lined porous carbon by salt-templating

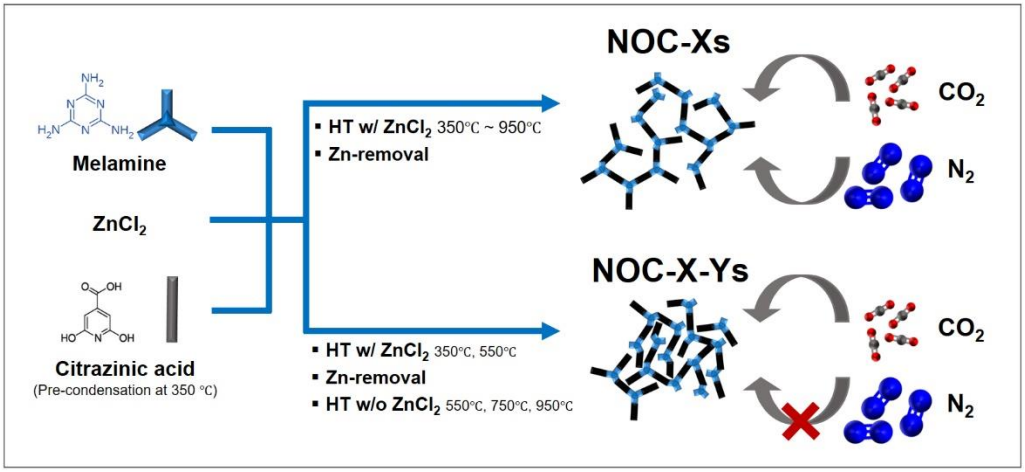

Figure 3.1 Preparation of nitrogen- and oxygen-lined salt-templated carbons with (NOC-Xs) and without (NOC-X-Ys) $ZnCl_2$ as pore stabilizer.

Table 1. EA summary of samples with and without pre-condensation.

	N-content (wt.%)	C-content (wt.%)	H-content (wt.%)	C/N	SSA_{BET} [$m^2 g^{-1}$]
NOC-550	18.0	54.6	3.1	3.5	532
NOC-550 without pre-condensation	11.3	57.0	3.5	5.1	457
NOC-550 Without pre-condensation and melamine	9.3	57.8	3.0	6.2	290

Abundant and low cost citrazinic acid (the condensation product of citric acid and ammonia) was at first heated to 350 °C for partial condensation. The color changed from yellow to black and elemental analysis is showing that the condensate is composed of 16.0 wt.% nitrogen, 55.7 wt.% carbon, and 2.2 wt.% hydrogen. The corresponding oxygen content of 26.0 wt.% (calculated by assuming oxygen as the only element present in addition to C, N, and H) and the atomic C/N ratio of ~4 are indeed lower than in citrazinic acid showing that larger condensate structures can be

formed by this preheating. After reaction with melamine as cross-linker and additional nitrogen source in molten $ZnCl_2$ at 350 °C or 550 °C, the materials were heated to 550 °C, 750 °C, and 950°C (**Figure 3.1**) to prepare the covalent, disordered frameworks with abundant oxygen- and nitrogen-lined edges by controlled condensation of these precursors. When citrazinic acid is used without the preheating step and without melamine, the final products are still porous but have lower nitrogen content and a higher C/N ratio (**Table 1**). Addition of melamine to the uncondensed citrazinic acid leads to a product with even lower heteroatom content and porosity (**Table 1**). FT-IR measurements further show apparent differences between citrazinic acid and the product of pre-condensation (**Figure S1**). The main peaks of citrazinic acid[238] in range of 1690 – 1640 cm^{-1} and 1290 – 1190 cm^{-1} almost disappeared after pre-condensation.

Table 2. EA and yield of NOC-Xs and NOC-X-Ys materials.

	C-content (wt.%)	N-content (wt.%)	Total O-content* (wt.%)	Adsorbed O-content** (wt.%)	Covalent O- content (wt.%)	C/N (at. ratio)	Yield (%)***
NOC-350	50.3	20.4	26.4	7.5	18.9	2.9	78
NOC-550	54.6	18.0	23.3	13.3	10	3.5	53
NOC-750	46.4	11.6	37.3	26.1	11.2	4.7	38
NOC-950	59.8	4.8	32.1	19.0	13.1	14.5	27
NOC-350-550	45.7	21.1	30.0	7.8	22.2	2.5	49
NOC-550-750	64.8	15.6	16.3	11.5	4.8	4.8	32
NOC-550-950	77.0	7.5	13.0	11.9	1.1	12.0	26

* Calculated by assuming oxygen as the remaining weight from integrated element weight of C, N, H, and S measured by EA.

** Calculated from the mass loss of TGA at 100°C assuming water as the only physisorbed species.

*** Calculated relative to the amount of melamine and pre-condensed citrazinic acid used.

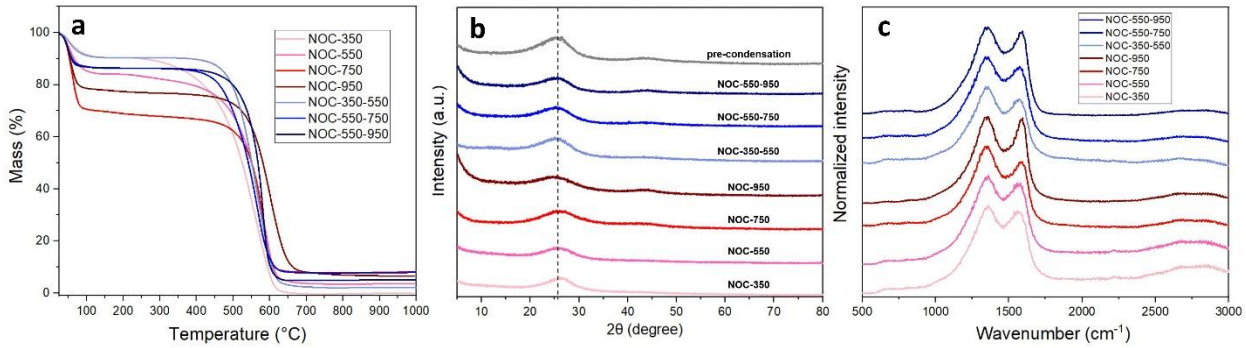

Figure 3.2 (a) TGA curves under synthetic air, (b) XRD patterns, and (c) Raman spectra of NOC-Xs and NOC-X-Ys.

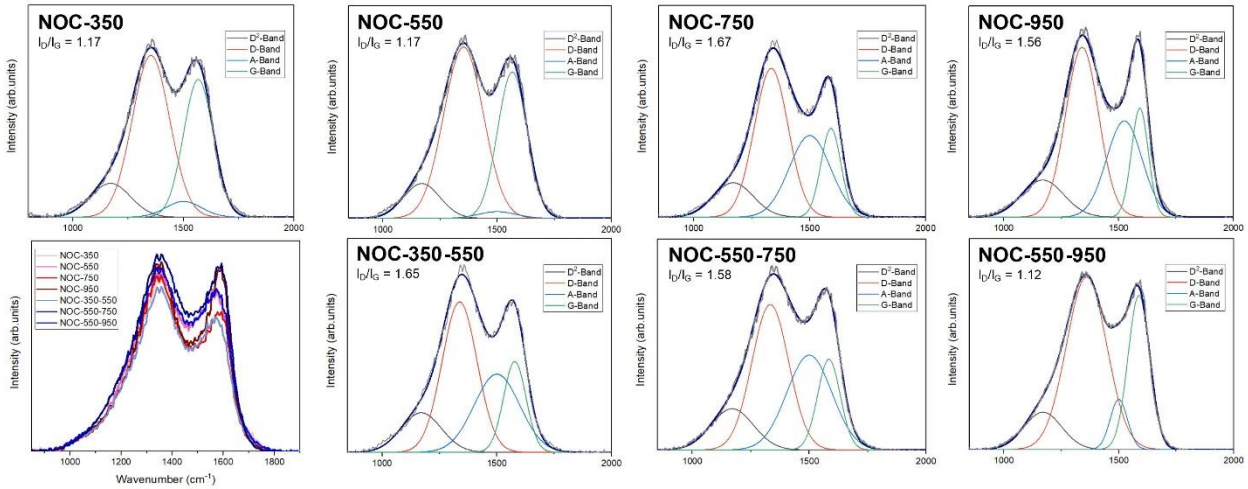

Figure 3.3 Fitted Raman spectra of NOC-Xs and NOC-X-Ys.

Elemental analysis (EA) of the obtained samples (**Table 2**) is a first simple, but very powerful tool to follow the condensation chemistry. Very importantly, EA of such heteroatom rich porous carbon materials always has to be analyzed considering the possibility of contribution to oxygen and nitrogen content from water adsorbed by the samples from air and possible contributions from other species present in such pore-confined water. In order to decouple the oxygen from physically adsorbed water, oxygen contents have to be discussed in relation to the thermogravimetric analysis (TGA) data of all samples (**Figure 3.2**a). In all samples, but especially in the high surface area

materials NOC-750 and NOC-950, a distinct mass loss occurs around 100 °C. This is indicating that a high amount of water and/or gases from air are physically adsorbed in the pores of the materials at ambient conditions which has to be subtracted from the oxygen content from EA to determine the amount of oxygen that is covalently bonded in the framework. In case of NOC-750, nearly 30 % of mass loss takes place due to this reversible evaporation of adsorbates, which is in a good agreement with the water vapor physisorption data discussed later. As the 350 °C sample is not porous, we consider it as a reference to monitor the condensation chemistry. The nitrogen content in NOC-350 sample is higher and the oxygen content is slightly lower than in the preheated citrazinic acid, indicating the ongoing condensation with melamine. The 550 °C sample is already structurally porous, so that this sample can be understood as the first fully condensed species with heteroatom-lined pores to discuss. The nitrogen content of 18 wt.% is still very high and 10 wt.% of oxygen remain covalently bonded. Heating these samples further in the presence of salt leads to a decrease of the nitrogen content in away typical for C_3N_4 (at 600 °C) or C_2N (at 800 °C), the oxygen stays in the sample and thereby gets relatively enriched. The 750 °C and 950 °C samples then have a fully developed pore system with a SSA of about 1200 $m^2\ g^{-1}$ (**Table 3**). Summing the heteroatom content of both species shows~23 wt.% and ~18 wt.%, respectively. These are unusually high heteroatom contents well beyond the typical “doping” exercises.

To figure out the role of $ZnCl_2$ in generating and stabilizing the micropore functionality, salts were removed by HCl solution immediately after the first heating at a rather lower temperature, and then the salt-free samples were heated again. The samples loose both surface area as well as the high-heteroatom functionality and turn into “ordinary” heteroatom doped carbons. Obviously, the presence of Zn ions is stabilizing the oxygen at the pore surfaces, while heating the former

frameworks without $ZnCl_2$ results in pore collapse. The final yield decreases independent of presence or absence of salt template at high temperature (**Table 2**).

Table 3. Ar physisorption at 87 K (specific surface area, pore volume, micropore volume), and CO_2/N_2 selectivity at 273 K data of NOC-Xs and NOC-X-Ys materials.

	SSA_{BET} [$m^2 g^{-1}$]	$V_{p/p0=0.95}$ [$cm^3 g^{-1}$]	$V_{Ar (<2 nm)}$ [$cm^3 g^{-1}$]		CO_2/N_2 selectivity at 273 K	Yield (%)***
			cylindr./sphere pores adsorption branch	slit pore, equilibrium model		
NOC-350	n.a.	n.a.	n.a.	n.a.	130.1	78
NOC-550	532	0.20	0.20	0.21	60.1	53
NOC-750	1265	0.59	0.39	0.56	30.3	38
NOC-950	1151	0.60	0.32	0.54	31.5	27
NOC-350-550	n.a.	n.a.	n.a.	n.a.	52.1	49
NOC-550-750	399	0.16	0.15	0.18	47.3	32
NOC-550-950	319	0.12	0.11	0.13	49.0	26

TGA under synthetic air shows that all materials are remarkably stable against oxidation by artificial air and decomposition, until temperatures well above 500 °C (**Figure 3.2**a). This is the typical behavior of a “noble” organic compound and secures applicability,[175] say in catalysis or for swing sorption, even at elevated temperatures. The mass of all samples stabilizes at round 700 °C without significant change upon further heating. Minor residual masses of ~10% ash content or below are measured for some samples indicating the nearly complete removal of $ZnCl_2$. The presence of traces of inorganic residuals can not be ruled out from these measurements and can be quantified by X-ray photoelectron spectroscopy (XPS) as discussed below.

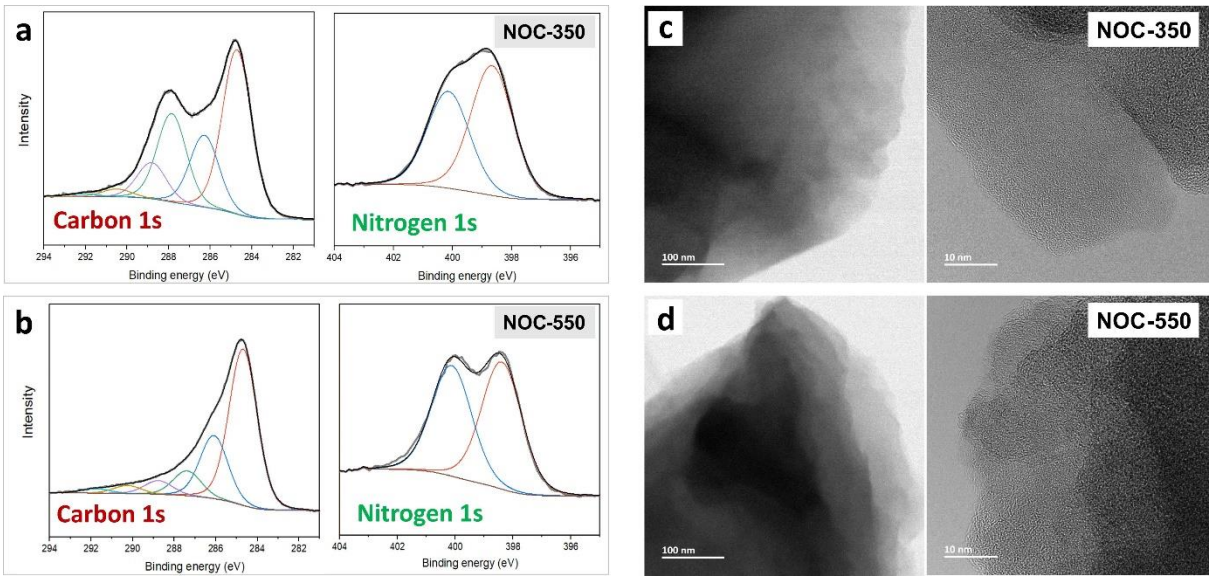

Figure 3.4 High-resolution C1s and N1s XPS spectra with corresponding fitting curves of (a) NOC-350 and (b) NOC-550 as well as and HRTEM images of (c) NOC-350 and (d) NOC-550.

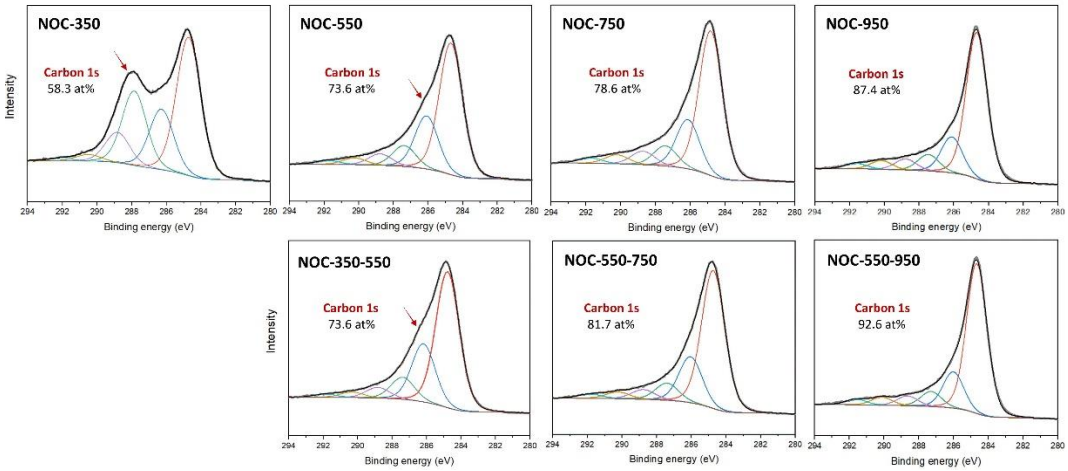

Figure 3.5 High-resolution C1s XPS spectra and corresponding fitting curves of NOC-Xs and NOC-X-Ys.

XPS is a useful tool to investigate the bonding characteristics of the different elements present at the surface of the materials (**Table S1**, **Figure 3.4**a-**3.4**b, and **Figure 3.5-3.7**).[204,239] The residual Zn content is approximately 0.2 at.% and less than 1.5 at.% of elements other than C, N, and O

(mainly halogens) have been detected on the surface of the samples (**Table S1**). The peaks in the C 1s spectra at lower binding energy around 285.4 eV and at higher binding energy around 286.1 eV can be assigned to electron-rich and to electron-poor carbon atoms, respectively.[240,241] In agreement with the EA analysis, the content of non-carbon elements decreases with temperature and it can be seen that the carbon materials condensed at low temperature such as NOC-350 or NOC-550 have a relatively higher content of electron-poor carbon arising from bonds with more electronegative nitrogen or oxygen (**Figure 3.5**). In comparison, the materials treated at higher temperatures have a larger C 1s peak at lower binding energy. In the fitted N 1s spectra, the nitrogen content decreases with increasing condensation temperature (**Figure 3.6** and **Table S1**). With the exception of NOC-350 with apparently higher concentration of nitrogen on the external surface, the overall nitrogen content and C/N ratio are comparable to the EA results. Except NOC-550-950, all samples show a dominant peak for electron-rich nitrogen around 398.4 eV. Such electron-rich nitrogen atoms are typically bonded to carbon as amine groups or in pyrazinic/pyridinic structure motives.[230] Notably, although the nitrogen contents in NOC-550-950 and NOC-950 are comparable, it appears that the latter has a relatively higher content of electron-rich nitrogen. In contrast, the majority of nitrogen present in NOC-550-950 is bonded as electron-poor (quaternary/graphitic) nitrogen, as well known form nitrogen-doped carbon materials prepared at higher temperatures.[230] This is supporting the assumption that the Zn template can stabilize pyrazines and pyridinic sites, i.e. edge nitrogen functionalities at higher temperatures. In contrast to elemental analysis, the oxygen contents in the materials can be more directly determined from the XPS spectra as only the oxygen and oxygen-containing compounds strongly bonded to the materials surface (i.e., covalently bonded to the material or bonded with the most

strongly attached water molecules) is present during the measurements (**Figure 3.7**). The oxygen contents determined from XPS follow the same trends as those from EA but are in general slightly lower in absolute number. One possible reason could be that oxygen-containing species and functional groups are less concentrated on the external surface. However, especially the significantly lower oxygen content of the partially condensed NOC-350 could relate to the ongoing condensation of the materials under the X-ray beam exposure and high vacuum XPS conditions. Similar to the case of nitrogen, the oxygen atoms become more electron deficient at higher condensation temperature, i.e., the binding energies in average shift to higher values. For NOC-X-Ys, the oxygen content continuously decreases with increasing the condensation temperature. In contrast, the NOC-Xs maintain a constant oxygen content which gets relatively enriched at high temperature.

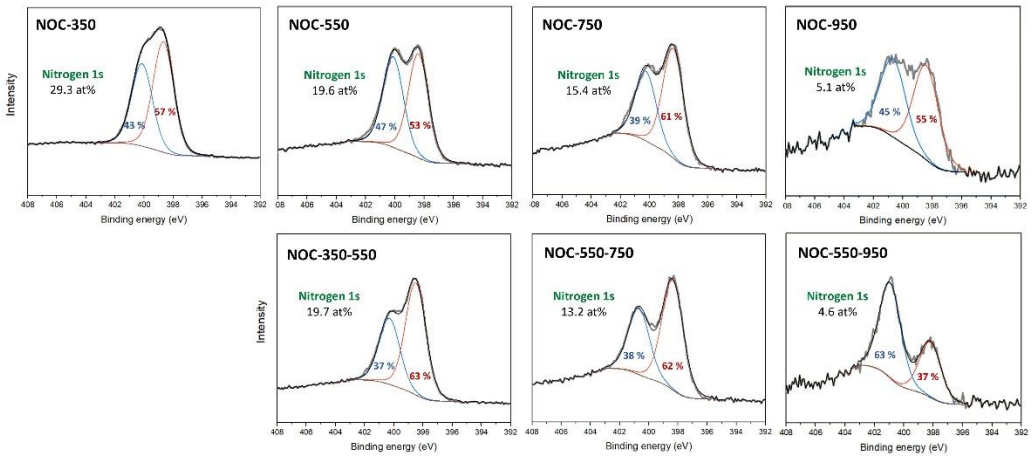

Figure 3.6 High-resolution N1s XPS spectra and corresponding fitted curves of NOC-Xs and NOC-X-Ys.

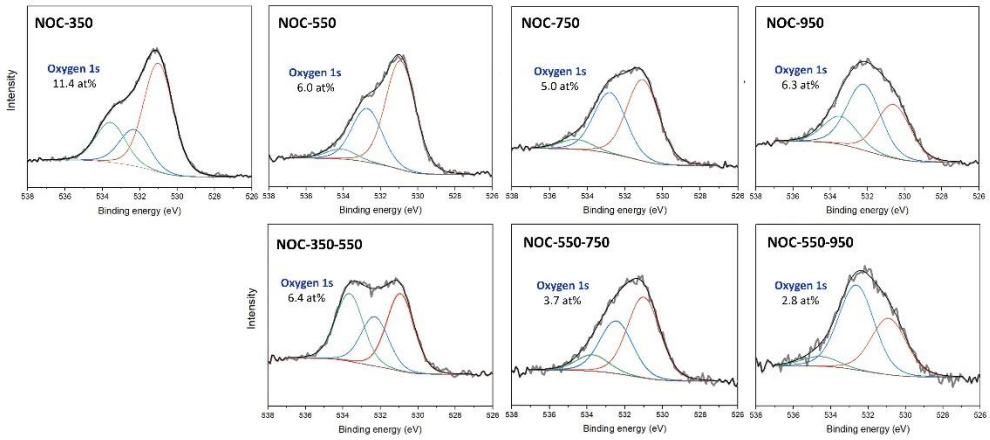

Figure 3.7 High-resolution O1s XPS spectra and corresponding fitted curves of NOC-Xs and NOC-X-Ys.

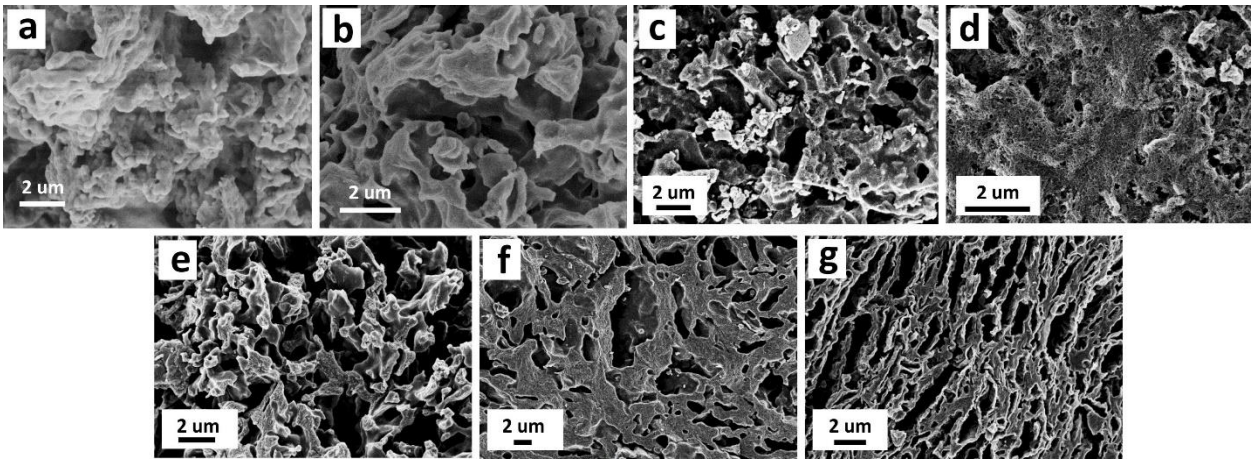

Figure 3.8 Scanning electron microscopy (SEM) images of (a) NOC-350, (b) NOC-550, (c) NOC-750, (d) NOC-950, (e) NOC-350-550, (f) NOC-550-750, and (g) NOC-550-950.

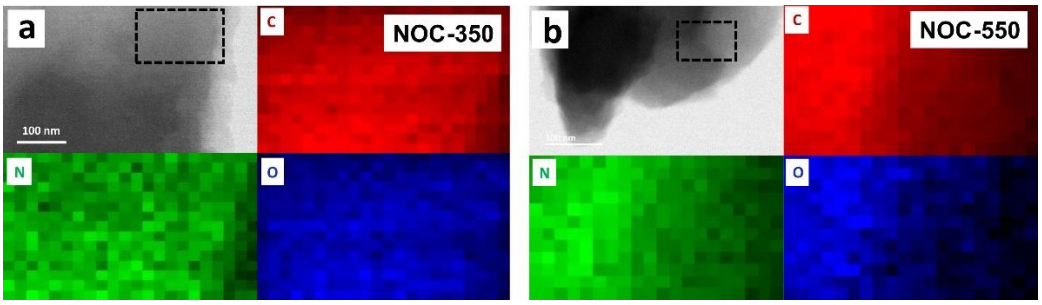

Figure 3.9 EDX elemental mapping of C (red), N (greed), and O (blue) of (a) NOC-350 and (b) NOC-550.

X-ray diffraction (XRD) patterns show a broad peak with low intensity in the 2θ range of 25°-30° for all materials representing the (002) plane of graphitic carbon stacking as it is typical for highly porous carbon materials without significant long-range ordering (**Figure 3.2**b). The absence of other peaks for all samples indicates that no major crystalline inorganic residuals remained independent of the method for removal of $ZnCl_2$, which is in line with the XPS and TGA results (**Table S1** and **Figure 3.2**a). Raman spectroscopy measurements (**Figure 3.2**c and **Figure 3.3**) of the NOC samples show the typical spectra of disordered carbon nanomaterials dominated by the disordered (D-band) peak at 1360 cm^{-1} and the graphite-like band (G-band) at 1600 cm^{-1}. The D-band arises from the breathing mode of sp^2 carbon atoms in aromatic rings at defect sites while the G-band is caused by any sp^2 carbon atoms organized in chains or rings. Unlike as for pristine carbons, the degree of graphitization or disorder cannot be simply estimated by the ratio of I_D/I_G as heteroatoms bonded to carbon cause dissymmetry of vibrations between the bonds.[242,243] However, all of them show the appearance that is typical for disordered carbon-based materials. NOC-X materials have sharper and separated D- and G-bands at higher temperatures, which does in such a case not necessarily originate from increased "carbon ordering" but rather from the dominance of carbon-carbon-bonds at high temperature.

In accordance with Raman spectroscopy, high-resolution transmission electron microscopy (HRTEM) analysis of the NOC-X materials (**Figure 3.4**c-**3.4**d, **Figure S2**, and **Figure 3.9**) is showing a random arrangement of carbon fringes as it is typical for porous carbon materials independent of the synthesis temperature. EDX elemental mapping, which has been exemplarily performed for NOC-350 and NOC-550, shows a homogeneous distribution of carbon, nitrogen and oxygen throughout both samples without any obvious zoning or gradients in the distribution

of these elements (**Figure 3.9**). SEM images are showing that all materials contain additional macropores and have a generally comparable morphology (**Figure 3.8**). Neither the synthesis temperature nor the presence or absence of $ZnCl_2$ at high temperatures has a major influence on the macrostructure of the materials, for which the large amount of $ZnCl_2$ that was used during the initial condensation seems to be the most important.

3.1.3. Structural characterizations for nitrogen- oxygen- lined carbons

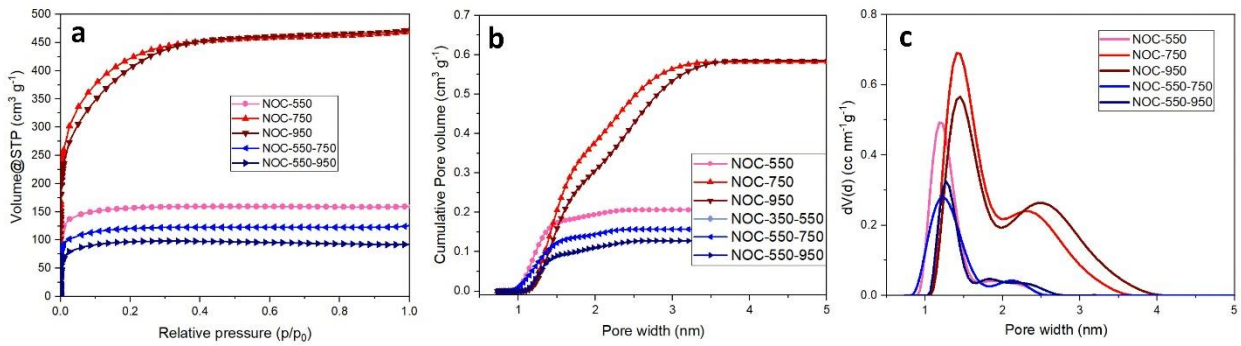

Figure 3.10 (a) Ar physisorption isotherms (87 K), (b) corresponding cumulative pore volume distribution, and (c) differential pore size distribution calculated with QSDFT (argon on carbons with cylindrical/sphere pores at 87 K) of NOC-Xs and NOC-X-Ys.

Ar (87 K) physisorption isotherms (**Figure 3.10** and **Table 2**) of NOC-Xs and NOC-X-Ys exhibit a shape of type I_a according to the IUPAC classification[68] with a high gas uptake at low relative pressure. For similar reasons as for zeolites, Ar physisorption is more appropriate to analyze microporous carbons with high content of heteroatoms compared to N_2 physisorption (**Figure S3-S4**).[244] N_2 with slightly larger kinetic diameter and higher quadrupole moment can have limitations to access the smallest micropores in the materials and specific interactions with the polar sites on the energetically heterogeneous surface can cause underestimation of pore sizes. Only samples NOC-350 and NOC-350-550 show no significant porosity that is detectable with Ar physisorption. As condensation temperature increases, the porosity of NOC-X materials becomes more developed and thus the pore volume detectable with argon increases up to 0.60 $cm^2\ g^{-1}$ for NOC-950. Pore size distributions have been calculated with two different DFT models. The trends in pore sizes and pore volumes are similar for assumption of mixed spherical and cylindrical pores from the adsorption branch and when the equilibrium model for slit-shaped pores is used (**Table**

2, Figure 3.10 and **Figure S4**). The pore size increases from the mainly microporous NOC-550 to NOC-750 and NOC-950 into which a significant volume of porosity is present in the form of small mesopores (**Figure 3.10**b and **3.6**c). In contrast, the specific surface area and the pore volume decrease from NOC-550 to NOC-550-750 and decrease even further to NOC-550-950. Materials with significantly lower pore volume and smaller pores below 1.5 nm in size are obtained when $ZnCl_2$ is removed in advance. As expected, $ZnCl_2$ plays a major role in the stabilization of micropores – especially at high temperatures before it decomposes and evaporates.

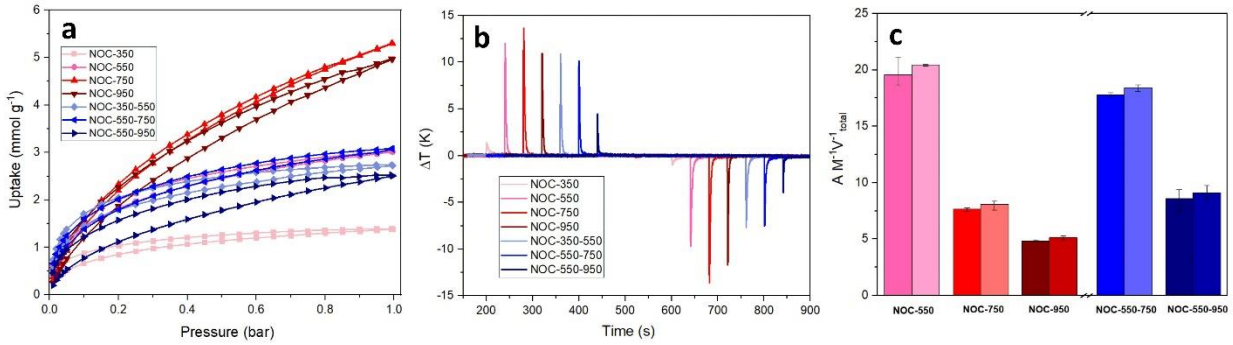

Figure 3.11 (a) CO_2 physisorption isotherms at 273 K, (b) CO_2 thermal response adsorption and desorption measurements at 1 bar and 25 °C, and (c) integrated adsorption and desorption (left bar and right bar, respectively) temperature peak area normalized by the mass and the total pore volume from Ar physisorption of NOC-Xs and NOC-X-Ys.

CO_2 (273 K) physisorption measurements (**Figure 3.11**a) are showing that NOC-350 and NOC-350-550 have a total CO_2 uptake of 1.38 mmol g^{-1} and 2.72 mmol g^{-1}, respectively, although both samples have no porosity that is detectable with Ar physisorption. Apparently, the pores in both materials are large enough to adsorb CO_2, but too small to be accessible for Ar. NOC-750 and NOC-950 with larger pores have a total CO_2 uptake of 5.3 mmol g^{-1} and 5.0 mmol g^{-1}, respectively, which is remarkably high and comparable to or higher than in many of the known nitrogen-doped

carbons prepared from more sophisticated precursors.[204,230,233] NOC-550 and NOC-350-550 show more convex shape of the CO_2 physisorption isotherms at low pressure (< 0.1 bar) where the effect of heteroatom doping leading to specific interactions between carbon dioxide molecules and pore walls is more apparent (**Figure 3.11**a and **Figure S5**a). Polarizable CO_2 molecules can specifically interact with functional groups or heteroatoms and in combination with size exclusion of larger molecules. This can improve the adsorption selectivity of materials.[245,246] The higher uptake of NOC-550 and NOC-350-550 at low pressure is in line with their high nitrogen and oxygen content and low porosity in Ar physisorption (**Table 2** and **Figure 3.6**).

Thermal response measurements with CO_2 as the test gas were carried out with the InfraSORP technology which provides further information about pore structures as well as CO_2 adsorption capacities and kinetics (**Figure 3.11**b).[208] It is obvious from the distinct temperature increase that all the samples have high affinity to CO_2 as significant heat release takes place during adsorption. Areas and shapes of the thermal response peaks are nearly similar during adsorption and desorption. This is confirming full reversibility of CO_2 adsorption in all samples by simple pressure swing due to purging with nitrogen. When the peak areas of the thermal responses are normalized by the sample masses and the total pore volumes derived from Ar physisorption, NOC-550 and NOC-550-750 have significantly higher peak areas compared to the materials condensed at the higher temperature, indicating higher heat of adsorption of CO_2 for these materials (**Figure 3.11**c). In other words, NOC-550 and NOC-550-750 release higher amount of heat during the adsorption of CO_2 per pore volume due to the small micropores with high heteroatom content in which the heat of adsorption and desorption is dominated by adsorbent–adsorbate interactions instead of

adsorbate-adsorbate interactions which are dominating in larger pores with less heteroatoms in the pore walls.[201]

Analysis of the IAST CO_2/N_2 selectivities of the NOC-X samples is showing that NOC-550 has the highest selectivity (60.1) among all samples except NOC-350, which reaches a value of 130.1 due to the stronger contribution of molecular sieving, that is, size exclusion of N_2 with a slightly larger kinetic diameter than CO_2 by the small pores. The CO_2 selectivity of NOC-750 (30.3) and NOC-950 (31.5) is significantly lower despite their high total uptake of CO_2 over 5.0 mmol g^{-1} at 1 bar. This is supporting the general observation that materials with high specific surface area usually do not achieve a high selectivity in CO_2 adsorption due to the significant contribution of non-discriminative surface.[4,233] In contrast, the NOC-X-Y samples maintain a relatively high selectivity around 50, regardless of the condensation temperature. As the selectivity is determined by the pore size which has to be small enough to kinetically accept CO_2 molecules (3.30 Å ; kinetic diameter) but not N_2 molecules (3.64 Å) and the content of nitrogen inside as mentioned in **Chapter 2.4.1**,[4] CO_2 can selectively be adsorbed in the samples with the highest ratio of micro pore volume over total pore volume such as NOC-550, NOC-550-750, and NOC-550-950. Further analysis is showing that there is a proportional relationship between the ratio of micropore volume and the CO_2/N_2 selectivity (**Table 2** and **Figure S5**b). From the combination of these geometrical considerations and the elemental compositions of the materials it can be seen that the presence or absence of the salt template can be used as a “regulation screw” to adjust these properties within a certain window and thus the properties of the materials in adsorption-related application such as selective removal of CO_2 from N_2 or CO_2 storage. This is of particular importance in a practically relevant case such as the one discussed here, where a sustainable templating method is combined

with abundantly available precursors the condensation of which yields highly heteroatom-rich carbon materials. CO_2 physisorption was additionally measured for NOC-550 and NOC-750 at 298 K (**Figure S5**c). Just like at 273 K, NOC-550 has a higher CO_2/N_2 selectivity of 81 in comparison to NOC-750 which as a selectivity of 35. Stronger binding of CO_2 is also expressed by the higher isosteric heat of adsorption at a CO_2 uptake of 1 mmol g^{-1}, which is ~40 kJ mol^{-1} for NOC-550 but only ~27 kJ mol^{-1} for NOC-750 with larger pores and lower heteroatom content.

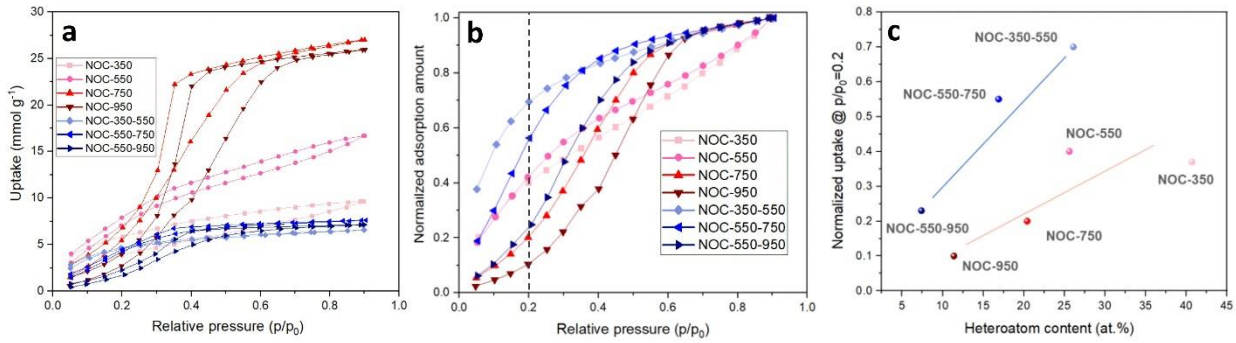

Figure 3.12 (a) Water vapor physisorption isotherms at 298 K, (b) normalized amount adsorbed relative to the maximum H_2O uptake at 298 K, and (c) the normalized uptake at relative pressure $p/p_0 = 0.2$ as a function of the nitrogen and oxygen content of NOC-Xs and NOC-X-Ys from XPS.

H_2O vapor physisorption isotherms (**Figure 3.12**a) are of type I for all samples with small micropores. NOC-750 and NOC-950 have larger pores and a less polar surface allowing for phase transitions of water molecules during adsorption thus resulting in a hysteresis loop that is typical for microporous carbon materials. Most NOC-Xs and NOX-X-Ys show high water adsorption capability. For example, the high H_2O uptake of NOC-750 at $p/p_0 = 0.9$ (27.10 mmol g^{-1}) corresponds to ~32 wt.%. These uptakes are in good agreement with the mass loss due to water desorption observed by TGA around 100 °C (**Figure 3.2**a). Taking the water loss in TGA at 100°C as a measure, the water adsorption capacities of NOC-750 and NOC-950 both correspond to a

relative humidity of ~35% that was exposed to the samples before they were subjected to TGA. Considering the pore volume of NOC-550 (0.2 cm^3 g^{-1} from Ar physisorption), the H_2O uptake of 7.14 mmol g^{-1} at a relatively low relative humidity of 20 % (corresponding to $p/p_0 = 0.2$ or ~6000 ppm water) is remarkable. Under these conditions, adsorption of water is dominated by adsorbent-adsorbate interactions and the uptake corresponds to a density of 22-23 water molecules per nm^3. Such a dense packing of water molecules in carbon-based materials has previously been reported for materials from synthetic molecular precursors and/or with more difficult templating procedures.[247] The nitrogen- and oxygen-lined pore walls support the binding of water molecules at low pressure by the formation of hydrogen bonding networks whereas the micropores allow for high water uptakes close to 100% humidity.

To further investigate the affinity between water and pore walls of the carbons, the relation between heteroatom content and the normalized uptake of water at $p/p_0 = 0.2$ is plotted (**Figure 3.12**b and **Figure 3.12**c). The higher normalized uptake at $p/p_0 = 0.2$ shows strong affinity toward H_2O at low relative humidity. Both NOC-Xs and NOC-X-Ys series show a trend of increasing normalized uptake as the heteroatom content or the N content from EA (**Figure S5**d) increases, which also has been shown in previous studies.[204,248] NOC-Xs, which have larger pores in comparison to NOC-X-Y, however, have overall a lower water uptake than NOC-X-Y, indicating a higher affinity to water for materials with smaller pores due to similar reasons as discussed above for carbon dioxide. NOC-X samples with larger pores have a notable but less pronounced relationship between water adsorption capacity and heteroatom content.

In summary, a novel synthesis pathway towards heteroatom-rich nanoporous carbon materials with high specific surface area and pore volume by using economically practical citrazinic acid

and melamine as precursors and $ZnCl_2$ as salt template has been reported. It has been shown that the presence or absence of salt template is a possible regulation screw to tailor the pore structure and atomic construction of the materials during heat treatment. Especially the bonding type of nitrogen and the oxygen content are significantly influenced by the salt template due to coordinative stabilization. By measuring Ar, CO_2, and H_2O physisorption, it has been shown that the presence of Zn at high temperature stabilizes the micropores and heteroatoms in the carbon material, thus contributing to higher total uptake in the adsorption of gases. At the same time, however, the CO_2/N_2 selectivity decreases due to the formation of larger micropores. With a very simple parameter of the removal of the salt template, heteroatom content, pore volume, or pore sizes can be controlled. Citrazinic acid, melamine, and $ZnCl_2$ have been chosen as synthetic case examples here along with CO_2 and H_2O vapor adsorption to show the relationships between synthesis, structure, and properties. The general principles, however, will likely also be applicable for other precursor molecules, other heteroatoms, other salt-templates, and other applications related to adsorption processes on carbon surfaces. For the system investigated in this work, more precise control and more detailed knowledge about the condensation product of citrazinic acid would be necessary to realize a more controlled condensation and possibly the synthesis of ordered porous networks.

3.2. Molecular designed nanoporous carbon from citrazinic acid and melamine for physisorption and energy storage of various polar adsorbates†

As the control over pore structure and atomic configuration provided by salt templates was elaborated in **Chapter 3.1**, the system of molecular-derived carbon materials (from citrazinic acid and melanine) was further investigated improving their adsorption ability and the results of these experiments will be presented in **Chapter 3.2**. By introducing a mixture of two salts as a template, the pore system can be generally enlarged in the samples in which the different structures were generated depending on the different condensation temperature. By examining the properties of the precursor materials, the material in the annealed state before the heat treatment, and the sample after carbonization in various analysis techniques, a possible mechanism of the formation of the carbon structure can be proposed (**Chapter 3.2.2**). Based on the structural information about the materials, the structure related properties of the adsorption of gases and ions will be discussed. The physisorption of CO_2 and H_2O especially revealed the zeolite-like properties of the samples showing the enhanced CO_2 selectivity over N_2 and the higher heat of adsorption in H_2O (**Chapter 3.2.3**). Besides, the electrochemical performance for energy storage devices based on other adsorption processes beyond the gas physisorption on the carbon materials will be presented for supercapacitors based on aqueous electrolytes in the same chapter. Furthermore, it is suggested that the capacitance appears due to change of the water configuration in a strongly adsorbing pore

† This chapter is adapted from manuscript in preparation for the publication : Sol Youk, Edina Šić, Bolortuya Badamdorj, Antje Völkel, Ivan K. Ilic, Wuyong Zhang, Torsten Gutmann, Markus Antonietti and Martin Oschatz "Salt-melt synthesis of molecularly designed nanoporous carbon from citrazinic acid for physisorption and energy storage" *Manuscript in preparation,* **2021**

system. This will be of great importance to understand the mechanism of energy storage, which is a substantial issue in the coming years.

3.2.1. Background and state-of-the-art

Nanomaterials have been widely investigated in recent years as already discussed in **Chapter 2.2** and **3.1**. One reason is their large interface area available for interactions with species from a surrounding phase.[249-251] Especially nanoporous carbon materials provide attractive properties as they can combine large surface areas and high porosity with chemical and thermal stability, as well as electronic conductivity.[252,253] They do not contain metals and are thus lightweight as well as in most cases environmentally friendly. This makes them attractive for various fields of application including but not limited to air purification, catalysis, energy storage, and gas separation.[254-259]

Several strategies are available to tailor the atomic construction and pore architecture of carbons.[27,175,260] This is crucial for their application as the kinetics and thermodynamics of adsorption of molecules, atoms or ions from surrounding fluids are mainly determined by pore sizes and polarizability of the pore walls. The latter is in most cases tuned by functionalizing the carbon framework with heteroatoms such as nitrogen and oxygen. Synthesizing these heteroatom containing nanoporous carbon materials by controlled condensation of abundant simple molecules to macroscopic objects is likely the most promising strategy for controlled insertion of heteroatoms and functional groups and by that for precise control over the chemistry of the pore walls and/or edge sites of individual carbon fringes.[145,175,230] While this chemistry is already widely applied for the synthesis of covalent-organic frameworks (COFs), its use for the production of heteroatom-

rich carbon materials at higher temperatures must be regarded as a different kind of chemistry. Here, a defined insertion of functional groups can lead to collective stabilization and higher heteroatom contents can be retained even after condensation at temperatures exceeding classical conditions of COF synthesis. This approach typically requires not only controlled condensation but also the use of molecular precursors which already contain heteroatoms in a specific chemical bonding motive.[117,261]

Once a defined framework has been created by condensation, it can be expected that further condensation to less heteroatom-rich (and by that often more electrically conductive) phases will also follow a more defined thermodynamic route. In that way, the condensation temperature can be applied as a more precise tool to tune the pore structure and the atomic construction of the carbon materials in comparison to synthesis with less defined starting materials. This is of huge importance especially for heteroatom-rich carbon materials which naturally have multiple different reaction pathways available during heating than their pristine counterparts. For that reason, the controlled condensation of abundantly available molecules to a covalent framework that can serve as a uniform and heterogeneous precursor material is a promising approach to establish the condensation temperature as an easily controllable regulation screw to fine-tune atomic construction and porosity of such materials and to retain a high content of heteroatoms at high temperature.

The importance of this kind of structural control in a given application is illustrated by the often-conflictive influence of heteroatom-content and pore sizes on the properties of the carbons. For instance, in selective CO_2 adsorption, high isosteric heats of adsorption can only be achieved if pores in the size range of the adsorptive and a high density of heteroatoms is present. The latter

often leads to low electric conductivity and in general such carbon structures are obtained after condensation at low temperature. In contrast, electrochemical energy storage in most cases requires large available specific surface areas and high electronic conductivity. This is typically obtained after condensation at high temperature when less heteroatom-rich carbon materials are obtained.

In this chapter, the feasible synthesis of sp^2- conjugated materials with high heteroatom content from citrazinic acid and melamine as abundant and simple molecules will be shown. Only by modulating the condensation temperature, the properties of the materials span over a remarkably broad range. Each material has its own specific characteristics that are suitable for a specific application such as gas adsorption (e.g., CO_2 and H_2O) or the capacitive energy storage in supercapacitors.

3.2.2. The physical properties and pore Structure of citrazinic acid and melamine based porous carbon

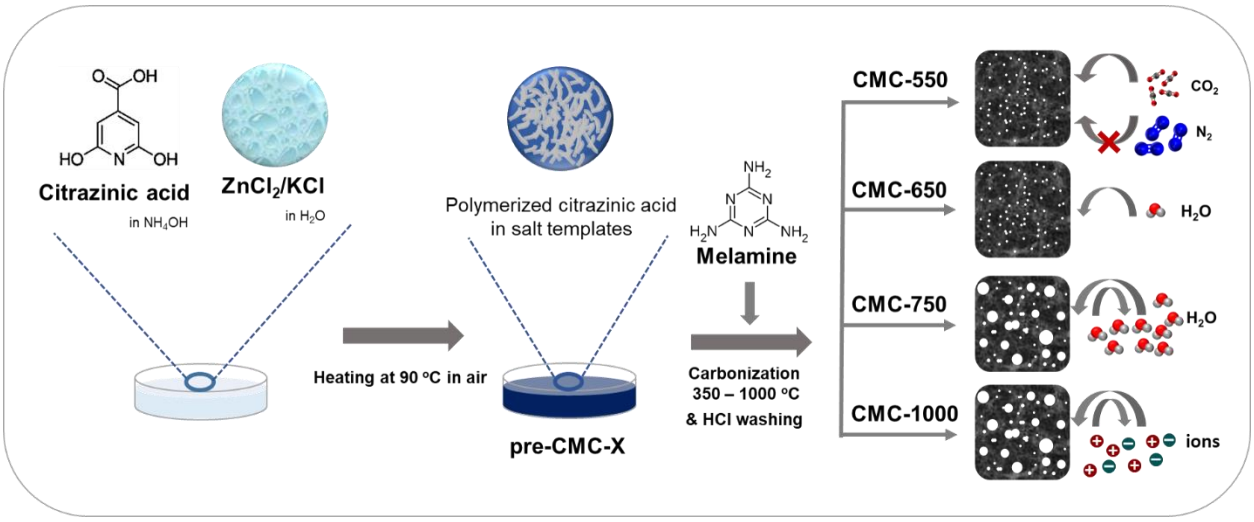

Figure 3.13 Preparation of salt-templated citrazinic acid and melamine based porous carbon (CMC-Xs).

Citrazinic acid dissolved in ammonium hydroxide solution was mixed with $ZnCl_2$ and KCl dissolved in DI water resulting in a homogeneous solution. After heating to 90°C, the mixture dried and gradually changed color to deep blue (**Figure 3.13** and **Figure S6**). The color change is characteristic for slightly condensed forms of citrazinic acid in aqueous solution.[262,263] Indeed, these heated mixture of salts and citrazinic acid shows distinct peaks in FTIR spectra including the signals of sp^2-conjugated or aromatic C=C vibrations (1580 – 1600 cm^{-1}) compared to the pristine citrazinic acid (**Figure 3.14**a). The main peaks in this material associated with several functional groups are usually present in indigoidine molecules which can be synthesized from citrazinic acid.[264] That is, the pre-CMC-X sample contains functional groups such as hydroxyl- or secondary amide- (3440 – 3200 cm^{-1}), ketone- (1680 – 1655 cm^{-1}), carbonamide groups (1670 – 1595 cm^{-1}), C-N binding (1300 – 1260 cm^{-1}), and alkyl amine groups (1220 – 1020 cm^{-1})[265-267] indicating a

structure comparable to indigoidine. After adding an excess of melamine as cross-linker and as additional nitrogen precursor, the condensation in salt-melt has been carried out in the temperature range between 350 and 1000 °C. In FTIR, the condensed samples such as CMC-550 and CMC-750 seem to be dominated by conjugated carbon bonds (1580-1600 cm^{-1}) and have a less intense signal for secondary amine (~3320 cm^{-1}) (**Figure 3.14**a).

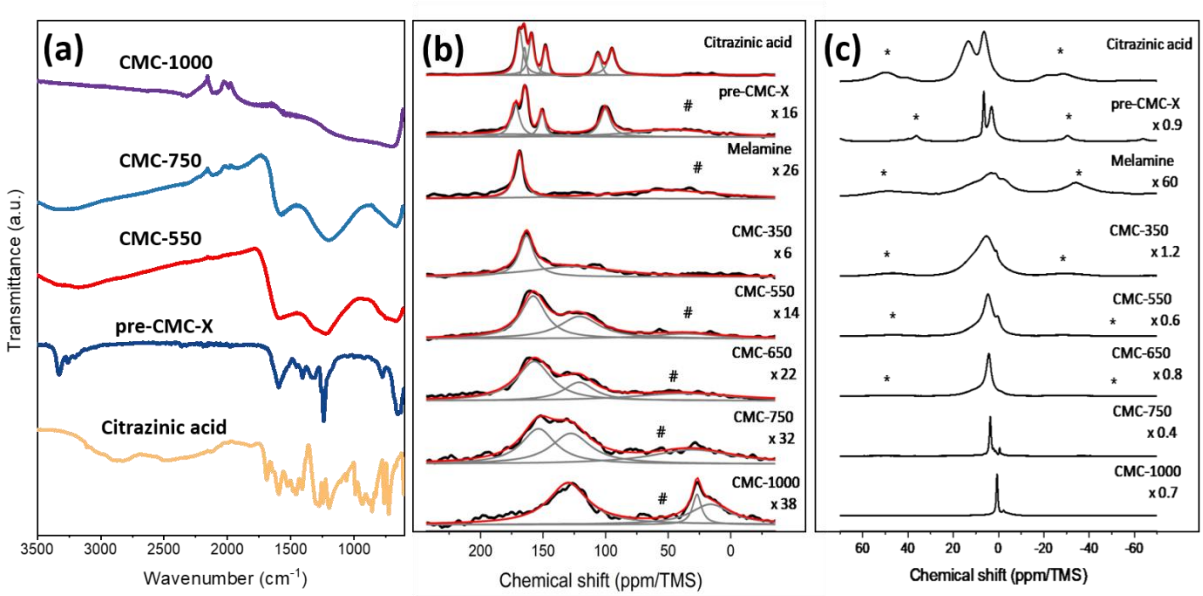

Figure 3.14 (a) Fourier transform infrared (FTIR) spectra of citrazinic acid, the dried mixture of salts and citrazinic acid, CMC-550, CMC-750, and CMC-1000, (b) $^{1}H \rightarrow ^{13}C$ CPMAS NMR spectra and (c) ^{1}H MAS NMR of the precursor materials citracinic acid, pre-CMC-X, melamine, and CMC-Xs. (The black, grey, and red lines are figured by the experimental results, the individual Gauss/Lorentz simulated peaks in the $^{1}H \rightarrow ^{13}C$ CPMAS NMR, and the cumulative fitted curves spectra, respectively, and the signals marked with * and # are spinning sidebands, and a background signal of the probe that could not be suppressed, respectively.)

After adding an excess of melamine as cross-linker and as additional nitrogen precursor, the condensation in salt-melt has been carried out in the temperature range between 350 and 1000 °C. As citrazinic acid and melamine are both the molecules which can easily form a stable hydrogen

bond motif and as it is known that building units are constructed when they are mixed together, a certain participation of non-covalent interactions such as hydrogen bonding or π–π stacking would have been formed in this reaction.[268] SEM images show a macroporous morphology for all condensation temperatures with a tendency for particle growth with increasing carbonization temperature (**Figure S7**). The nanoporous structure of CMC-550 and CMC-750 and the homogeneous dispersion of carbon, nitrogen and oxygen atoms are observed in HRTEM images and EDX elemental mapping (**Figure 3.15** and **Figure S8**). A structure composed of larger pores as well as longer, slightly more expanded and stacked carbon fringes is present in CMC-750.

The ^{13}C CPMAS NMR spectra of the precursor materials (citrazinic acid, pre-CMC-X and melamine) as well of the condensed CMC-X samples including the corresponding fits of their line-shapes are shown in **Figure 3.14**. Comparing these spectra, the chemical conversion of the precursor molecules to carbon-based systems is clearly seen as it is visible by the change of chemical shifts in the spectra (details of ^{13}C chemical shift values and line widths are given in **Table S2**. The spectra of the final products CMC-X exhibit no signal traces in the chemical shift range of the precursor materials. Hereby, it has to be noticed that the temperature has a strong impact on the NMR signal width, shape and signal position for the CMC-X materials. With increasing temperature, a significant signal broadening is obtained which most probably refers to a decreased order in the CMC-X materials. Such disorder is reflected in the signal broadening indicating a broader distribution of isotropic chemical shifts. Furthermore, the carbon signals are occurring in the higher field range of the spectra in CMC-X when the temperature is increased. This effect is most probably related to the formation of sp^2-hybridized carbon species at higher temperature which are expected to resonate in the region between 100 and 160 ppm according to

the literature.[269,270] Finally, in the spectrum of CMC-1000 additional broad signals are visible in the high field region between 50 and -20 ppm. These signals are most probably related to sp^3 hybridized carbon species according to [269,270], however it is also feasible that some of the signals in this region refer to distorted sp^2-hybridized carbon atoms.[271,272]

The ^{1}H MAS NMR spectra obtained for CMC-X presented in (**Figure 3.14**) show a similar trend of the chemical shifts for increasing temperature compared to the $^1H \rightarrow ^{13}C$ CPMAS NMR spectra. On the other hand, the line broadening is diminished with increasing temperature which seems contrary to the $^1H \rightarrow ^{13}C$ CPMAS NMR. The decrease in line width in the ^{1}H MAS NMR spectra (**Table S3**). Furthermore, a shift of isotropic signals to the higher field region of the spectrum is obtained with increasing temperature of the sample preparation as well by noticing additional signals of carbon materials below 0 ppm. The temperature influence on the chemical shift and line broadening behavior is consistent with the observation by Grünberg and co-workers[273] who studied hydrogen bondings of water in mesoporous silica materials applying ^{1}H NMR. According to their work, the estimated chemical shift for free water molecules should be observed between 0.8 and 1.5 ppm. The presence of hydrogen bondings shifts the isotropic chemical signals to the low field range of the spectrum and leads to a line broadening.

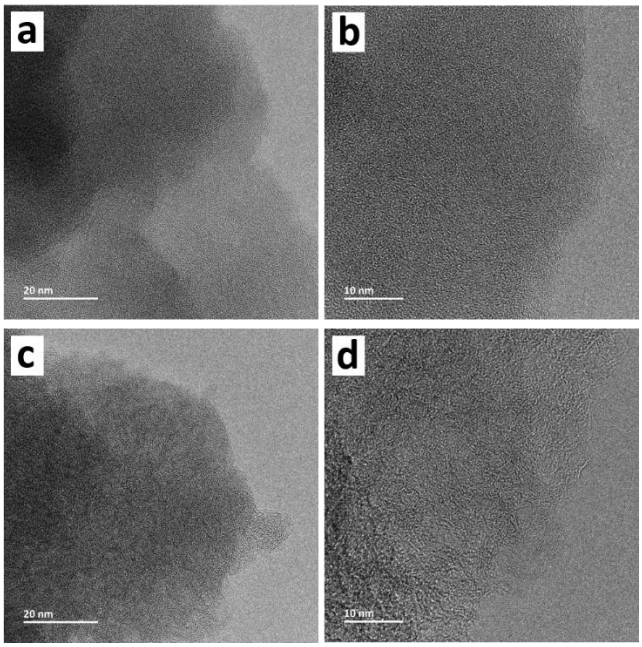

Figure 3.15 HRTEM images of (a,b) CMC-550, and (c,d)CMC-750.

Table 4. N_2 physisorption at 77 K (specific surface area, pore volume), micropore volume from N_2 (77 K) and CO_2 (273 K) physisorption, elemental analysis, and CO_2/N_2 selectivity at 273 K data of the CMC-Xs materials.

	SSA_{BET} [$m^2 g^{-1}$]	$V_{p/p0=0.95}$ [$cm^3 g^{-1}$]	$V_{N2\ (<2\ nm)}$ [$cm^3 g^{-1}$]	$V_{CO2\ (<1.5\ nm)}$ [$cm^3 g^{-1}$]	C [wt. %]	N [wt. %]	H [wt. %]	C/N (at. ratio)	CO_2/N_2 selectivity at 273 K
CMC-350	36	0.086	0	0.048	46.4	25.1	3.5	2.2	-
CMC-550	141	0.12	0.025	0.094	50.6	24.7	3.1	2.4	67.2
CMC-650	505	0.29	0.12	0.17	48.7	23.4	3.2	2.4	37.3
CMC-750	1826	1.3	0.40	0.40	55.1	14.9	3.0	4.3	31.0
CMC-1000	1533	1.4	0.35	0.38	68.4	4.7	2.0	17.1	15.5

Elemental analysis (EA) shows that the samples are all heteroatom-rich carbon materials with high content of nitrogen (**Table 4**). C/N atomic ratios of ~2.4 are present until condensation at 650 °C but increase at higher condensation temperatures (**Table 4**). ICP-OES analysis (**Table S4**)

shows no detectable K content while a small amount of up to 0.2 at.% of Zn was detected in few samples of CMC-650 and CMC-750.

X-ray diffraction (XRD) shows the typical patterns of porous carbon with a broad reflection around 26° 2Theta which represents the (002) plane of graphitic carbon (**Figure 3.16**a). The absence of other peaks shows that there are no impurities present after CMC synthesis. Raman spectroscopy of CMC-Xs is showing the typical signature for disordered carbon nanomaterials including the disordered band (D-band) peaks and graphite-like band (G-band) peaks at wavenumbers of 1360 cm^{-1} and 1600 cm^{-1}, respectively (**Figure 3.16**b). Due to the series of CMC-Xs carbon bonded to the heteroatoms which cause the dissymmetry of vibrations of the bonds, however, the ratio of I_D/I_G doesn't necessarily mean the degree of graphitization or disorder of the carbons.[242,243] The samples with high condensation temperature still have clearer separated D- and G-bands that with low condensation temperature which is because of the carbon-carbon bonds becoming dominant at high temperature.

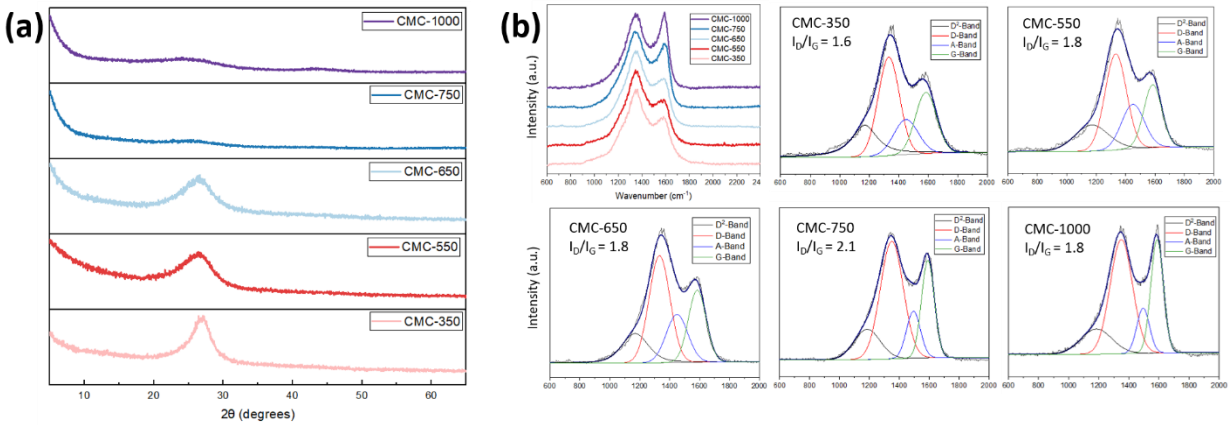

Figure 3.16 (a) XRD patterns, (b) the raw (left, top) and fitted Raman spectra of CMC-Xs.

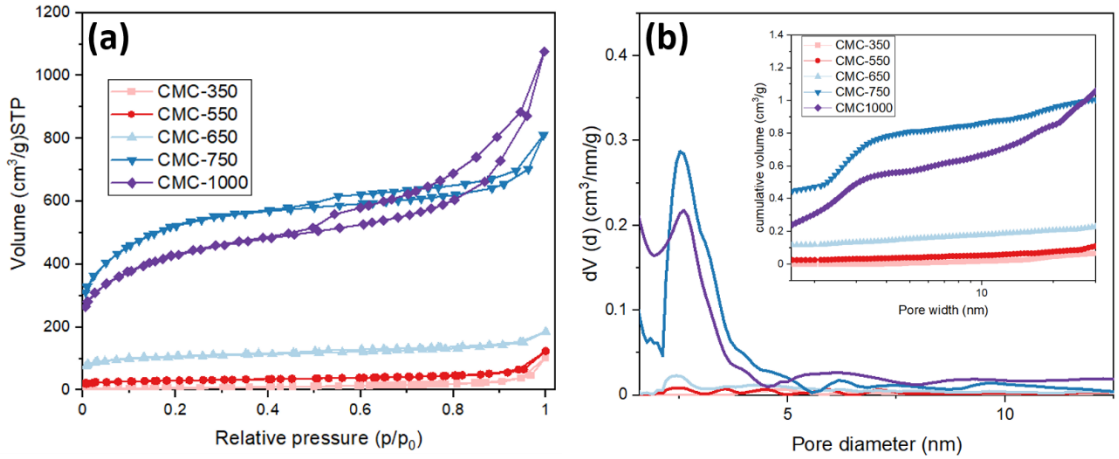

Figure 3.17 (a) Nitrogen physisorption isotherms (77 K) and (b) differential pore size distribution with corresponding cumulative pore volume distribution (inset) calculated with QSDFT (nitrogen on carbons with slit/cylinder and pores at 77 K) of CMC-Xs.

Nitrogen physisorption isotherms at 77 K of all CMC-Xs obtained at 650 °C or below show a Nitrogen physisorption isotherms at 77 K of all CMC-Xs obtained at 650 °C or below show a shape of type Ia acccording to the IUPAC classification revealing their microporous structure (**Figure 3.17**).[68] While CMC-350 and CMC-550 have no significant porosity detectable with nitrogen, CMC-650 has larger micropores and in consequence a signifcantly higher pore volume accessible for N_2 at 77 K. The porosity of CMC-Xs develops further as the condensation temperature increases, leading to the highest specific surface area upto 1826 m^2 g^{-1} in CMC-750 and pore volume of 1.4 cm^3 g^{-1} in CMC-1000 (**Table 4**). These samples even contain a significant volume of mesopores as indicated by the pronounced hysteresis loops in the isotherms. As the condensation temperature goes up to 1000 °C, the micropore volume and the specific surface area are reduced in comparison to CMC-750 while the total pore volume keeps increasing. In other words, the pores in CMC-1000 increase in size. Thus, considerably different pore structures are obtained for each carbonization temperature.

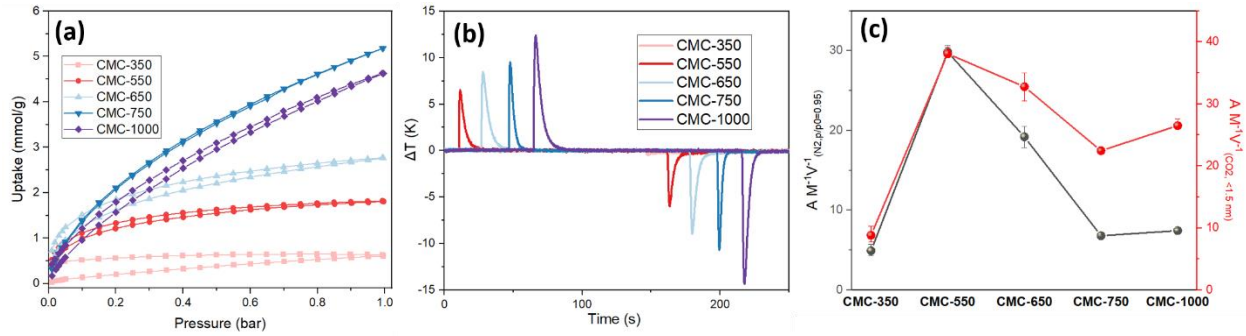

Figure 3.18 (a) CO_2 physisorption isotherms at 273 K and (b) CO_2 thermal response adsorption and desorption measurements from 3rd cycle at 1 bar and 298 K, and (c) integrated adsorption temperature peak area normalized by the mass and the total pore volume from nitrogen physisorption (black line) and by the mass and the micropore volume less than 1.5 nm from CO_2 physisorption (red line) of CMC-Xs.

In CO_2 physisorption experiments at 273 K, CMC-750 and CMC-1000 show a total CO_2 uptake of 5.2 mmol g^{-1} and 4.6 mmol g^{-1}, respectively (**Figure 3.18**a). This is in the same range as for other high surface area nitrogen-doped carbon materials.[203,233,274,275] CMC-550 and CMC-650 instead show a lower total CO_2 sorption capacity but a higher uptake of 1.0 mmol g^{-1} and 1.3 mmol g^{-1} at low pressure (p = 0.1 bar). This is indicating the strongly polarizing structure of the nanoporous carbons due to their higher nitrogen contents introduced by the precursor molecules. In combination with their small micropores, this leads to strong interactions with CO_2 molecules and a high IAST CO_2/N_2 selectivity of CMC-550 of 67.2 (**Table 4** and **Figure S9**). This combination of small micropores possibly contributing to size exclusion of N_2 and high polarizability is a combination that is typically known to push CO_2 sorption selectivity of carbon-based materials in the presence of N_2 to a range that is commonly only achieved by zeolites or other metal-containing materials.[4]

Thermal response measurements with CO_2 as the test gas have been carried out with an InfraSORP optical calorimeter. CO_2 adsorption in all materials obtained at 550 °C or above follow

comparable sorption kinetics and have fully reversible CO_2 uptake (**Figure 3.18**b).[24,208] Of the total pore volume in the materials, the amount occupied by CO_2 is relatively represented by normalizing each temperature peak area by the mass of the materials and by the total pore volume from N_2 physisorption (black line in **Figure 3.18**c). CMC-550 has the highest normalized heat released while other samples, especially CMC-750 and CMC-1000, have significantly lower values. This shows that only a smaller part of the pore volume of the latter samples can be used for CO_2 adsorption despite their high total pore volume. In other words, CMC-750, CMC-1000 have a high volume of pores that is not involved in CO_2 adsorption, whereas most of the pores in CMC-550 are used for CO_2 adsorption. On the other hand, the temperature peak area divided by the mass and the pore volume obtained from CO_2 adsorption (red line in **Figure 3.18**c) are showing higher normalized peak areas especially for the samples obtained at higher temperatures, i.e., those with larger mesopore content.

Due to the highly polarizing surface of the CMC materials, they have a very high affinity to water. All the H_2O physisorption isotherms show a type I shape except for CMC-750 and CMC-1000 (**Figure 3.19**a). Despite its relatively low specific surface area, CMC-650 has the highest water uptake of 6.6 mmol g^{-1} in the relative pressure region below $p\ p_0^{-1}$= 0.2 (6000 ppm) usually representing the surface hydrophilicity of specific materials. This is followed by CMC-550 and CMC-750 with uptakes of 4.7 mmol g^{-1} and 4.5 mmol g^{-1}, respectively (**Figure S10**a). CMC-650 as well as CMC-350 and CMC-550 take up more than 40 % of their H_2O storage capacity already at $p\ p_0^{-1}$= 0.2 showing that surface-water interactions play a more dominant role in these samples in comparison to those prepared at higher temperatures (**Figure S10**b). CMC-650 as well as CMC-350 and CMC-550 take up more than 40 % of their H_2O storage capacity already at $p\ p_0^{-1}$= 0.2

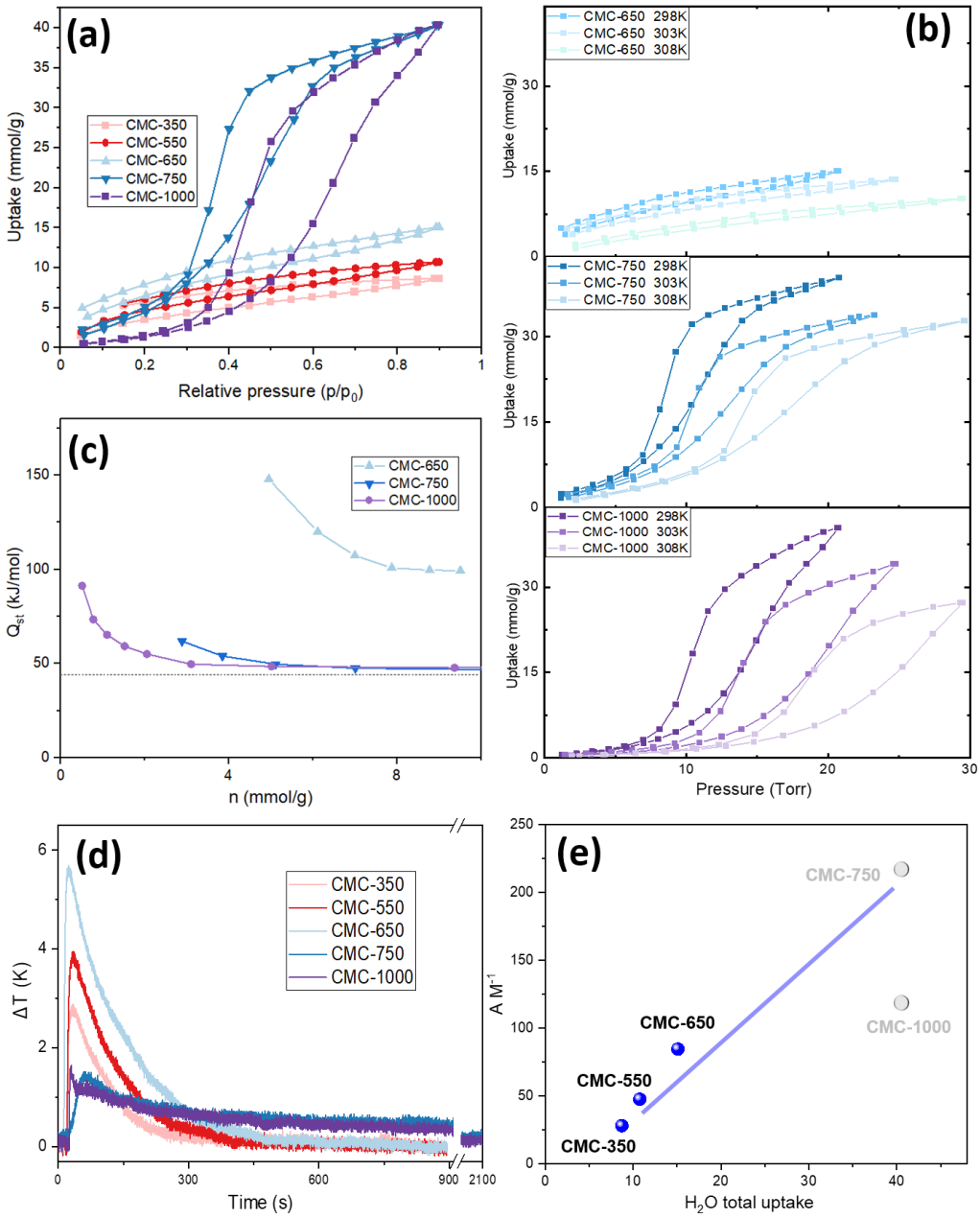

Figure 3.19 (a) H_2O physisorption isotherms at 298 K, (b) various temperatures of CMC-Xs, (c) isosteric heat (Q_{st}) from H_2O desorption curves of CMC-650, CMC-750 and CMC-1000, (d) thermal response measurements of H_2O adsorption (1bar, 298 K), and (e) correlation of H_2O total uptake at p p_0^{-1} = 0.9 from physisorption and normalizing temperature peak area of H_2O from InfraSORP by the mass of CMC-Xs.

showing that surface-water interactions play a more dominant role in these samples in comparison to those prepared at higher temperatures. The heat of adsorption (Q_{st}) of H_2O as a function of the amount adsorbed was calculated by using the desorption curves from measurements at 298, 303, and 308 K [1] (**Figure 3.19**b and **3.18**c). It is obvious that the uptake shifts to higher absolute pressure as the temperature of measurement increases which is typical while there is no certain change of the curves each other in a sample (**Figure 3.19**b). CMC-650 shows a remarkably high Q_{st} of more than 100 kJ mol^{-1} below an uptake of 5 mmol g^{-1} and keeps ~100 kJ mol^{-1} above 5 mmol g^{-1} (**Figure 3.19**c). Despite this high heat of adsorption, the water adsorption remains reversible over the entire relative pressure range investigated. CMC-750 and CMC-1000 instead show a Q_{st} of more than 50 kJ mol^{-1} only in the pressure region where water molecules are directly adsorbing on the pore walls. After a certain loading has been achieved, the heat of adsorption levels of at a value close to the evaporation enthalpy of liquid water, indicating that water-water interactions are then becoming dominant. This is the reason for the pronounced hysteresis loop in these samples. CMC-750 and CMC-1000 have a remarkable total uptake of more than 40.3 mmol g^{-1} at p p_0^{-1}= 0.9 due to their high pore volume.

InfraSORP measurements using water as the adsorptive and nitrogen as the carrier gas were carried out to investigate water adsorption over time by calorimetry (**Figure 3.19**d and **Figure 3.20**). CMC-350, CMC-550, and CMC-650 have a thermal response curve with a shape that is rather comparable to the thermal response curves in CO_2 adsorption. However, the temperature increase is lower and the adsorption process is spanned over a longer time range in CMC-750 and CMC-1000. The most likely reason for that is the slow rate of water supply during the measurement. However, when comparing the peak areas of CMC-350, CMC-550, and CMC-650

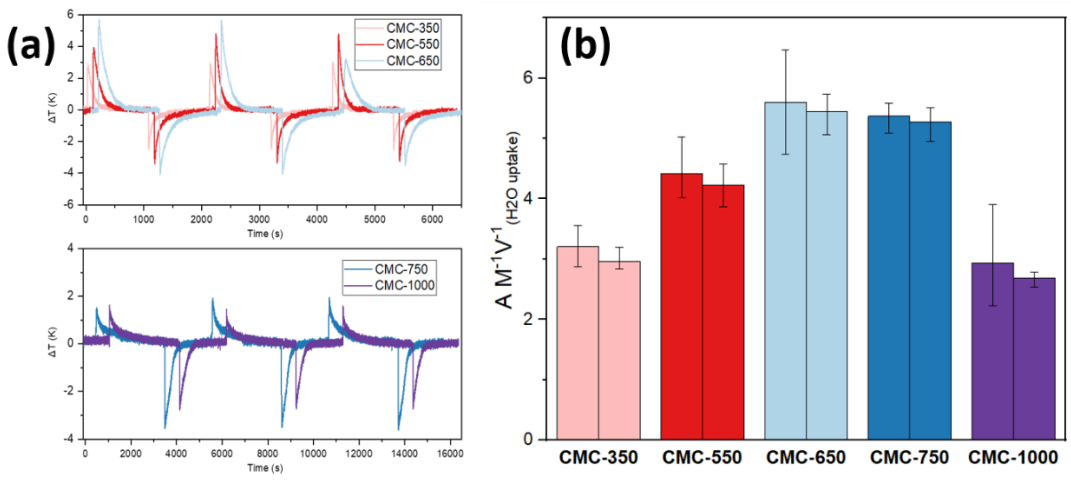

Figure 3.20 (a) Thermal response measurements of H_2O adsorption (1bar, 298K) of CMC-Xs and (b) integrated adsorption (left) and desorption (right) temperature peak area normalized by the mass and the total H_2O uptake from H_2O physisorption at p p_0^{-1} = 0.9 of CMC-Xs.

it becomes evident that these measurements still reflect the differences in the water uptakes of these materials (**Figure 3.19**e). CMC-650 has the highest intensity peak showing a strong affinity with water, while CMC-750 and CMC-1000 show that the adsorption/desorption was not fully conducted even for a long period of time of more than 2000 s (**Figure 3.19**d). The normalized result of this peak area by the weight of the applied sample has a linear correlation with the total water total uptake, except for CMC-1000 which is dominated by water-water interactionsCMC-650 had the highest value when normalizing the peak area by both the sample weight and the total uptake of H_2O from physisorption in **Figure 3.19**a, followed by CMC-550, which means that adsorption/desorption in InfraSORP can be well correlated to that volumetric experiments (**Figure 3.20**). CMC-650 shows particularly strong as well as rapid adsorption of water which is well in line with the physisorption results. In addition, it can be seen that adsorption and desorption have relatively similar values revealing reversible adsorption in all samples (**Figure 3.20**).

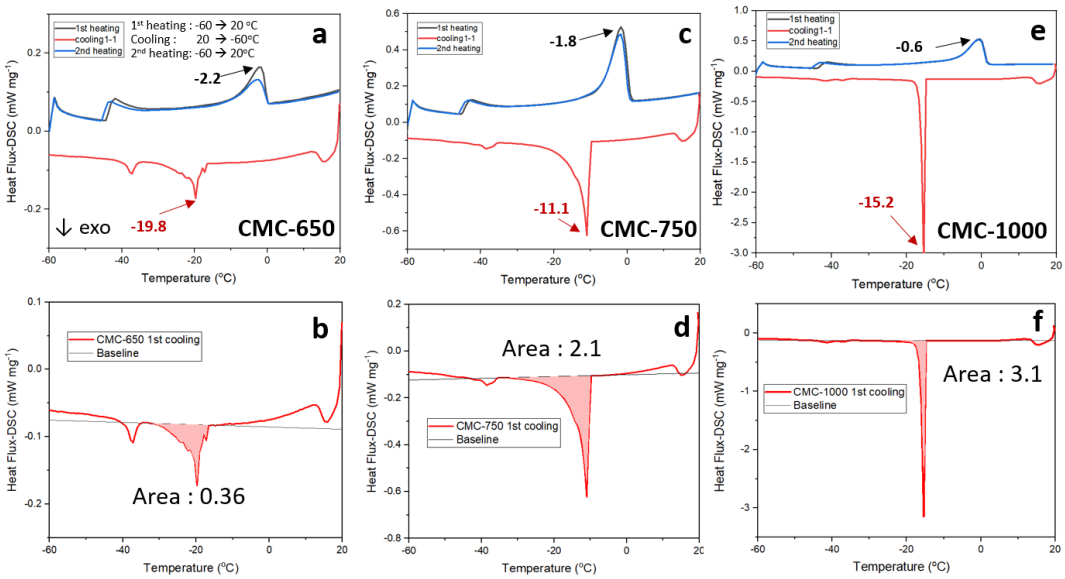

Figure 3.21 DSC curves and the integrated surface area from 1st cooling cycle curve with baseline of water-filled (a,b) CMC-650, (c,d) CMC-750, and (e,f) CMC-1000.

Differential scanning calorimetry (DSC) analysis of water-filled samples under N_2 atmosphere has been carried out between -20 and +20 °C for CMC-650, CMC-750, and CMC-1000 (**Figure 3.21**). The amount of deionized water corresponding to the pore volume of each sample has been impregnated prior to the measurement to observe the phase transition of water in the confined pore systems of the carbon materials. All DSC curves show the presence of phase changes in the adsorbed water which are all fully reversible as can be seen by the almost similar heat flux profile between 1st and 2nd cycle. As expected, water shows significantly reduced freezing points due to the need for nucleation under confinement in the pores.[276] This reduction in the freezing point/melting point is inversely proportional to the pore size. When increased volume of droplet, the freezing temperature would be increased because of its higher probability of nucleation than for the smaller droplet. When confined in the narrow pore structure of porous carbon, the droplets

of liquid water could be supercooled. Besides, all samples have another freezing peak around – 40 ℃. Earlier reports showed the freezing point of water confined in pores was reduced down to ~ – 39 ℃ due to homogeneous nucleation of ice. This effect is comparable to the cavitation effects in the desorption of gas and it depends on the pore structure such as pore shapes or entrance size.[277,278] It is known that the minimum freezing temperature is around – 40 ℃ as it is also observable for CMC-X.[278]

Regarding the freezing temperature between – 10°C and – 20°C, it would be guessed to come from water in the pore structure. CMC-650 shows a particularly low freezing point of – 19.8 °C compared to others, probably because this sample has high N content as well as very narrow pores. The freezing point is not only lowered due to the narrow pores as mentioned earlier, but also due to the high affinity to water on the heteroatom-decorated pore walls. In addition, the result of integrating the area of the water phase transition in CMC-650 is about 0.36 which is about 6 times and 9 times less than those of CMC-750 (area : 2.1) and CMC-1000 (area : 3.1), respectively (**Figure 3.21**b,d,f). This value is significantly lower than water uptake of CMC-650 in comparison to CMC-750 and CMC-1000. Besides, a high N content in CMC-650 could stabilize the water molecules adsorbed on the pore walls. CMC-750, which showed almost the same total uptake as CMC-1000 in H_2O physisorption, had a DSC curve area of only 2.1, which is also smaller than that of CMC-1000 (3.1). As CMC-750 also has a significant amount of N and a high portion of micropore, there is obviously a lower number of water molecules able to undergo a phase transition than in CMC-1000 or the structure of adsorbed in this material is already more close to ice.

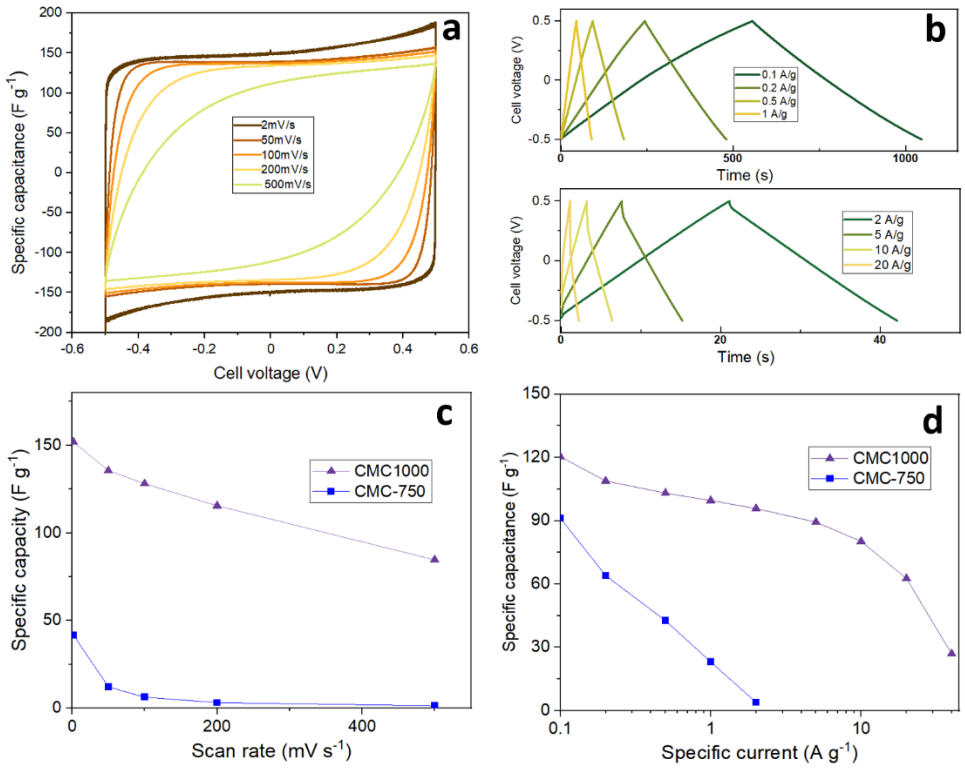

Figure 3.22 (a) Cyclic voltammograms at different scan rates, (b) charge/discharge curves at different specific currents of CMC-1000, (c) specific capacitance with increasing scan rate, and (d) specific capacity with increasing specific current of CMC-750 and CMC-1000 in 1 M Na_2SO_4.

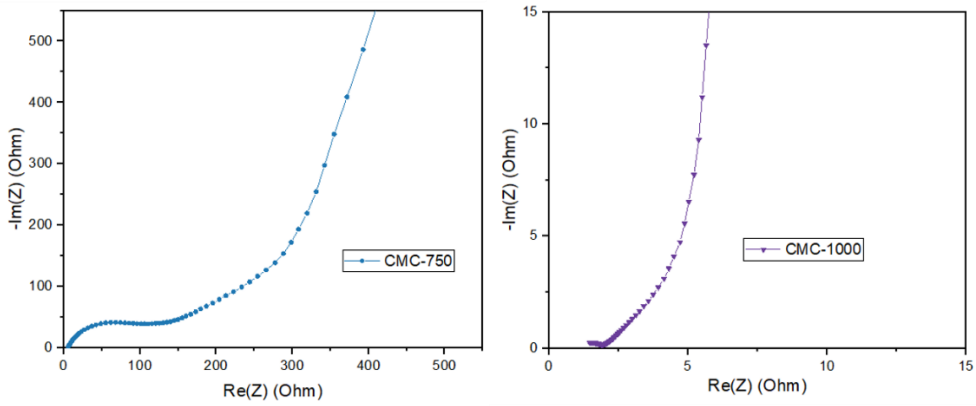

Figure 3.23 Nyquist plots of CMC-750 and CMC-1000 tested in 1 M Na_2SO_4.

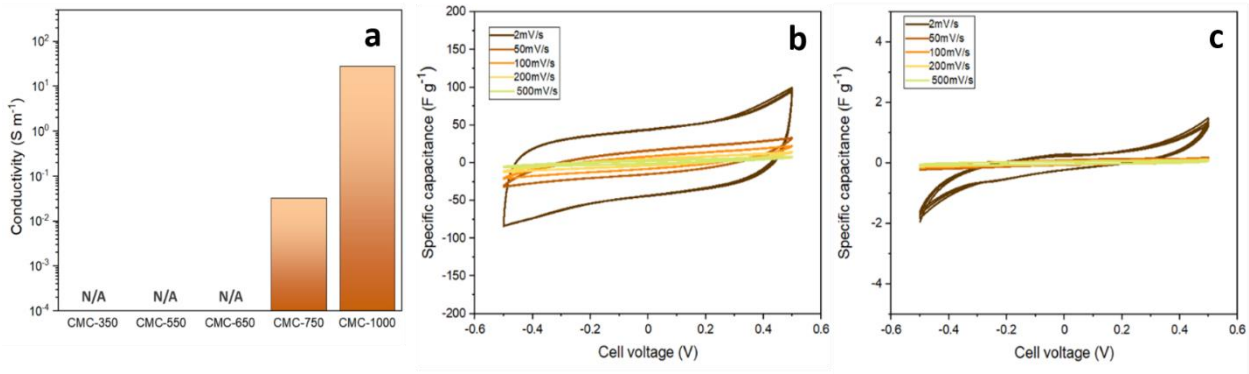

Figure 3.24 (a) Conductivity measurement of CMC-Xs, and cyclic voltammograms of (b) CMC-750, and (c) CMC-650 at different scan rates.

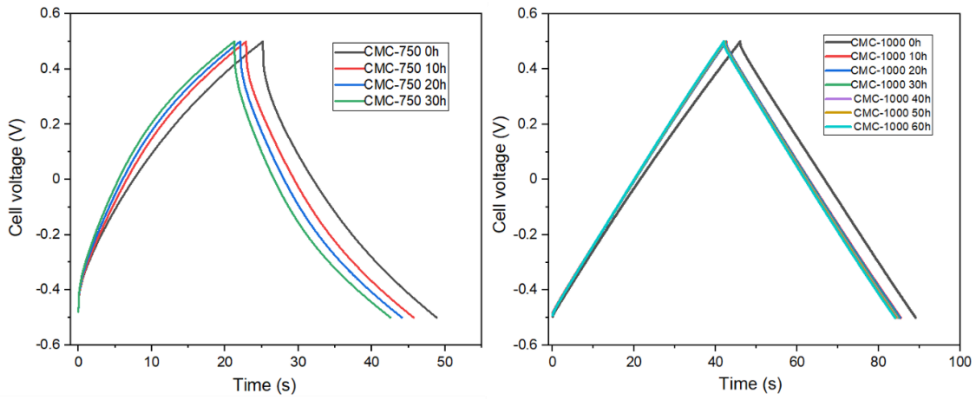

Figure 3.25 Charge/discharge profiles of CMC-750 and CMC-1000 at 1 A g^{-1} every 10 h in 1 M Na_2SO_4.

CMC-750 and CMC-1000, which especially had a high amount of water total uptake, should also have a high electronic conductivity, so their electrochemical performances as EDLCs has been investigated in 1 M Na_2SO_4 neutral aqueous electrolyte (**Figure 3.22**). CMC-1000 exhibits a clear rectangular CV which is typical for a predominantly capacitive charge storage mechanism (**Figure 3.22**a). This material shows a symmetric triangular shape in galvanostatic cycling with potential limitation (GCPL) with a small voltage drop of 0.19 V at 10 A g^{-1} and a specific capacitance of 120 F g^{-1} at 0.1 A g^{-1} (**Figure 3.22**b). Meanwhile, CMC-750 has a small area and no obvious

rectangular shape in CV and the capacitance immediately decreases when the current density passes 0.2 A g^{-1} (**Figure 3.22**c, and **3.22**d) because of its low conductivity (**Figure 3.24**). The Nyquist plot of CMC-1000 has a relatively vertical curve in the low-frequency region representing the capacitive behavior of EDLCs, whereas CMC-750 shows a more inclined curve (**Figure 3.23**). The low conductivity of CMC-750 is due to the high N content (**Table 4**). Accordingly, in the case of CMC-650, it can be seen that the capacitance is almost invisible in both CV and GCPL (**Figure 3.24**). In cycling stability test by charging and discharging (from – 0.5 to 0.5 V) at 1 A g^{-1} of specific current, CMC-1000 and CMC-750 demonstrate 97 % and 89 % of the first cycle capacitance, respectively, only CMC-1000 showing with maintaining the symmetrical triangular curves after 60 h (**Figure 3.25**). Overall, it can be concluded that even though it has a lower affinity to water, CMC-1000 is a more suitable material for supercapacitor applications in comparison to CMC-750 and CMC-650 as it has a balance between hydrophilicity and electric conductivity. On the other hand, the charge of CMC-750 is convex upward and the discharge is convex downward, which is hardly the phenomenon of supercapacitor. In the middle between the behavior of supercapacitors and batteries, it implies that there is a chemical interaction beyond the electric double layer.

In conclusion, porous carbon materials containing high content of heteroatom and high sp^2-conjugated were feasibly synthesized from simple molecules of citrazinic acid and melamine via salt-templating. Their well-defined pore structure as well as atomic construction led to strong affinity toward guest adsorptive molecules. Especially, by regulating the condensation temperature each material has suitable adsorption properties. Not only are they significantly good at selective CO_2 adsorption over N_2, but they have particularly strong affinity for water thermodynamically,

which outperforms well-known desiccants such as conventional zeolites. Some of these had high water uptake that could fill a significant portion of the pore structure with water molecules. In addition, when heat treated at high condensation temperature, they showed prominent electrical energy storage capacity in aqueous electrolyte-based EDLCs. As all of the presented results of gas adsorption (e.g., CO_2 and H_2O) or the capacitive energy storage are based on physicochemical adsorption processes for polar adsorptive species, it represents that the properties of the materials span over a remarkably broad range of applications.

3.3. Carbon materials with kinetically favorable pore structure by direct pyrolysis of a preorganized hexaazatriphenylene precursor ‡

As described in the previous chapter (**Chapter 3.1** and **Chapter 3.2**), the synthesis of functionalized porous carbon from pre-organized molecular precursors have many advantages. The materials synthesized from simple molecules and salt templating can be utilized in physical adsorption applications with enhanced performances due to the functionalized surface as well as highly defined porosity (**Chapter 3.2**). In **Chapter 3.3**, the adsorption kinetics of a series of nitrogen-doped carbon materials obtained by using pyrolysis of hexaazatriphenylene-hexacarbonitrile (HAT-CN) under different atmospheres will be introduced. With a stoichiometry close to C_2N and a homogeneously well-distributed pyrazinic nitrogen, these template-free materials have shown ultrahydrophilic properties.[230] Although the pore system can be obtained through condensation at a certain temperature, there is a weakness that a portion of inner pores of the particle cannot be accessed by gases in the application process due to the disc-shaped particles including an outer shell blocking the invasion of gases into the pore network. Through the carbonization under vacuum, the formation of the outer shell can be avoided, as described in this chapter. In that way, materials with attractive gas adsorption properties can be combined with sufficient adsorption kinetics.

‡This chapter is adapted from manuscript in preparation for the publication : *Sol Youk, Nadja Tarakina, Markus Antonietti, and Martin Oschatz* "Noble Carbon with Enlarged and Kinetically favorable Pore Structure by Direct Pyrolysis of a Preorganized Hexaazatriphenylene Precursor" *Manuscript in preparation,* **2021**

3.3.1. Background and state-of-the-art

Template-free microporous carbon materials have been synthesized recently by direct carbonization of the hexaazatriphenylene-hexacarbonitrile (HAT-CN) precursor.[230,233] HAT-CN itself has an aromatic structure with a π–π stacking which is already electron-deficient so that has significant resistance against oxidation in air. In addition, the carbonized materials have a stoichiometry close to ideal C_2N through the controlled condensation mechanism. With the highly polarized molecular structure, they are the outstanding materials leading to not only the enhanced adsorption properties toward various gas species such as N_2, CO_2, and H_2O but also to high selectivity to specific species (e.g., CO_2/N_2) representing the potential for the catalytic conversions.

The morphological structure of carbonized HAT particles, however, tend to interfere with their possibilities in adsorption with limited contact time due to their spherical disk-shaped particles with graphitic shells.[233] In other words, their shells, which are developed during high-temperature treatments can lead to slow mass transport to the inner pores and may even lead to geometrical exclusion of molecules that are too large to pass the shell. It is important to figure out how the formation of such a shell can be prevented so that the inner pores can be reached in order to maximize the use of all available pores.

Here the synthesis of HAT-CN-derived materials by direct carbonization at two different temperatures under different atmospheres is reported. The application of a vacuum can prevent the formation of the outer shell during condensation, so that the inner areas of the particles are becoming more easily accessible.

3.3.2. The pore structure properties of Vac-HAT-Ts and C-HAT-Ts

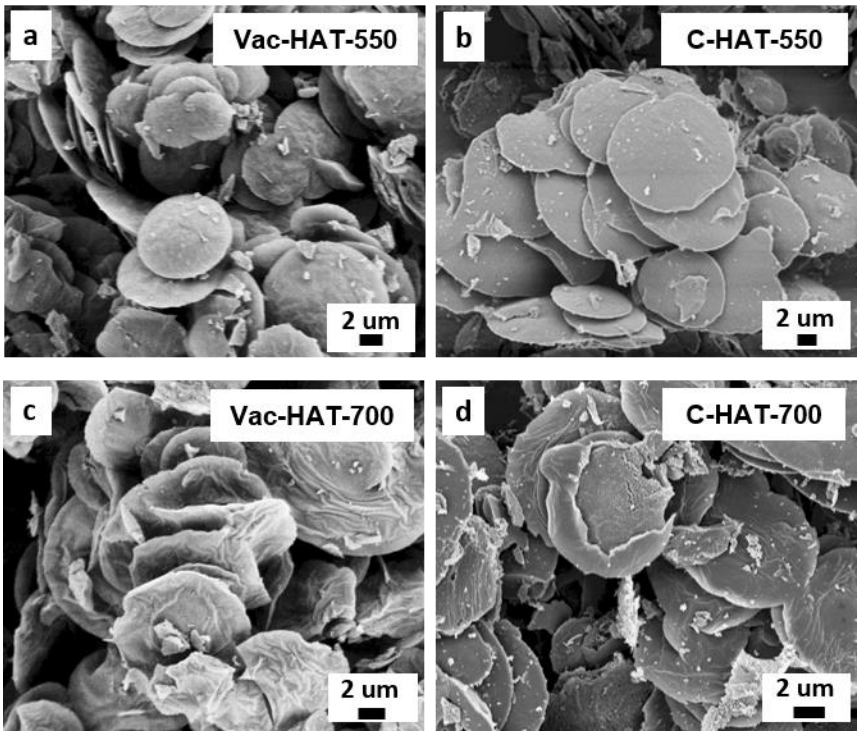

Figure 3.26 SEM images of (a) Vac-HAT-550, (b) C-HAT-550, (c) Vac-HAT-700, and (d) C-HAT-700.

Table 5. N_2 at 77 K (specific surface area, pore volume), Ar at 87 K (specific surface area, pore volume) micropore volume from N_2, Ar and CO_2 physisorption, EA, and yields of Vac-HAT-Ts and C-HAT-Ts.

	SSA_{BET} (N2) [$m^2 g^{-1}$]	$V_{p/p0=0.95}$ (N2) [$cm^3 g^{-1}$]	$V_{<2\ nm}$ (N2) [$cm^3 g^{-1}$]	SSA_{BET} (Ar) [$m^2 g^{-1}$]	$V_{p/p0=0.95}$ (Ar) [$cm^3 g^{-1}$]	$V_{<2\ nm}$ (Ar) [$cm^3 g^{-1}$]	$V_{<1.5\ nm}$ (CO2) [$cm^3 g^{-1}$]	C-content (at.%)	N-content (at.%)	C/N (at. ratio)	Yield
Vac-HAT-550	785	0.44	0.26	552	0.28	0.19	0.28	45.0	26.9	1.7	9.2%
C-HAT-550	352	0.22	0.09	473	0.29	0.15	0.21	50.4	29.9	1.7	50%
Vac-HAT-700	809	0.35	0.29	666	0.25	0.25	0.3	48.6	22.6	2.1	30%
C-HAT-700	762	0.33	0.27	695	0.26	0.26	0.37	51.1	23.1	2.2	33%

The pre-synthesized HAT-CN precursor consists of flat, disk-shaped particles with diameters in the micrometer range.[230] After condensation, particle shape is maintained in all samples regardless of temperature and the use of argon flow or vacuum (**Figure 3.26**). However, the surface appears rougher and defective for some individual particles of Vac-HAT-700 and C-HAT-700. This is not the case for the samples condensed at 550°C which have a rather smooth and less fractured particle surface. Especially in C-HAT-700 it can be seen that the defective particles consist of a dense shell and a more porous core which has already been observed in one of our recent studies.[233]As condensation in vacuum does apparently not affect the particle shape itself, the fracture of the surface must be caused by the higher temperature. The C/N ratio does also not change for a given synthesis temperature depending on the presence or absence of vacuum (**Table 5**). As the C/N atomic ratio of Vac-HAT-550 and C-HAT-550 are 1.7 while Vac-HAT-700 and C-HAT-700 have about 2.2, it is shown that the element composition is more dependent on the temperature rather than the environment of the heat-treatment. The nitrogen contents of the samples condensed at 550 °C are expectedly higher and the C/N ratios are lower than after condensation at 700 °C. This trend is reasonable as the condensation proceeds via the formation of dicyan especially when the condensation degree of C-HAT-CN is higher at 700 °C.[230] This further indicates that more gaseous byproducts are formed during condensation at 700°C. These molecules would diffuse out of the particles because the repolymerization of these carbon-nitrogen species to a paracyan-like network is likely to occur on the external particle surface.

It is notable that the condensation yield of Vac-HAT-550 is only 9.2 %. Indeed, when the various samples that are carbonized at different temperatures from 200 °C to 700 °C under vacuum, the yield tends to decrease as the temperature increases except for Vac-HAT-550 which have

significantly low (**Figure S11** and **Table S5**). It could be seen that the removal of gaseous condensation products from the particle surface at lower temperature under vacuum is faster than repolymerizing and stacking on the particles at 550 °C. That is, the decomposed by-products are removed right away due to the atmosphere of the vacuum, thus a significantly low yield can be shown. On the other hand, as repolymerization of the decomposed species on the particles is rather faster at 700 °C regardless of the environment of heat-treatment, no significant difference in yield can be observed between Vac-HAT-700 and C-HAT-700.

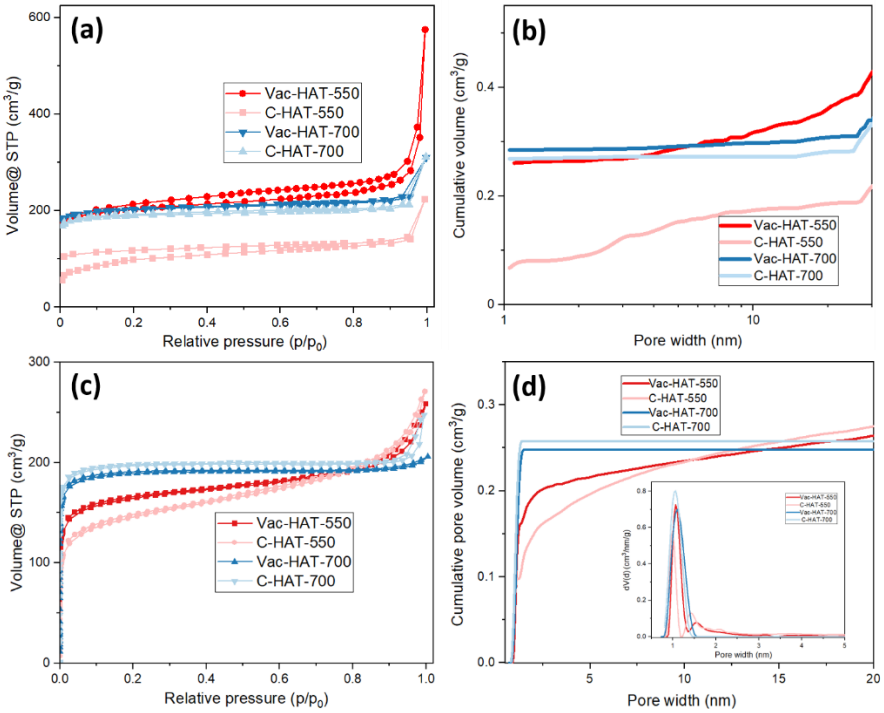

Figure 3.27 (a) N_2 isotherms at 77 K, and (b) corresponding cumulative pore volume distribution, (c) Ar isotherms at 87 K and (d) corresponding cumulative pore volume distribution (insets: differential pore size distribution) of Vac-HAT-Ts and C-HAT-Ts.

Although the morphology and the heteroatom contents of each material are similar, the difference in the pore structure system has been shown. N_2 physisorption isotherms of all C-HAT-

Ts and Vac-HAT-Ts show the type Ia with a remarkable uptake at low relative pressure according to the IUPAC classifications[68] which reveals the exclusive microporous structure performing a similar trend to previously reported ones (**Figure 3.27**a).[230,233] The Vac-HAT-550, however, included a highly increased curve in the range of high relative pressure representing the presence of large micropore or mesopore. The specific surface area of Vac-HAT-550 is 720 $m^2 g^{-1}$ which is even about as twice as those of C-HAT-550 with 430 $m^2 g^{-1}$ even though the condensation temperature of those two samples is same (**Table 5**). The total pore volume of Vac-HAT-550 and C-HAT-550 are 0.5 $cm^3 g^{-1}$ and 0.25 $cm^3 g^{-1}$, respectively, indicating the higher amount of larger pores is formed in Vac-HAT-550. Thus, it is obvious that the condensation condition in the vacuum has the effect on the formation of pores. On the other hand, in both Vac-HAT-700 and C-HAT-700 using the same temperature of 700 °C, there is no noticeable difference with the specific surface area of ~ 800 $m^2 g^{-1}$ as well as the total pore volume ~ 0.35 $cm^3 g^{-1}$ that indicates that the temperature of 550 °C is particularly affected by the vacuum conditions.

Ar physisorption results, however, show somewhat different isotherms. In N_2, the isotherm of Vac-HAT-550 is similar to that of Vac-HAT-700 or C-HAT-700, but in argon, it shows a curve located rather lower than them (**Figure 3.27**c). In the total pore volume, there is a larger difference between Ar and N_2 measurements in the samples carbonized at 550 °C than those carbonized at 700 °C. The total pore volumes of Vac-HAT-700 and C-HAT-700 are similar each other showing 0.25 $cm^3 g^{-1}$ and 0.26 $cm^3 g^{-1}$, respectively, which is the similar trend in the N_2. Vac-HAT-550 and C-HAT-550 are also quite similar each other with 0.28 $cm^3 g^{-1}$ and 0.29 $cm^3 g^{-1}$, respectively, which is, however, significantly different from the N_2 result (**Table 5**). In addition, the micropore volume result is more conspicuous, because Vac-HAT-550 and C-HAT-550 reveal comparable

micropore volume of 0.19 $cm^3 g^{-1}$ and 0.15 $cm^3 g^{-1}$, respectively, in Ar, whereas Vac-HAT-550 has almost three times larger than that of C-HAT-550 in N_2. This is because N_2 has accessibility limitations due to its slightly larger molecule size and higher quadrupole moment at low temperature which interfere with measuring the very small micropores.[233] The micropores measured with CO_2 which will be discussed later also reveal a slightly less difference than the results of N_2 between Vac-HAT-550 and C-HAT-550, it is more likely because significantly smaller size of CO_2 molecules take less restriction to reach very small pores than N_2. Nevertheless, it is still apparent that Vac-HAT-550 shows higher micropore volume ratio in it regardless of the measured gas (i.e., N_2, Ar and CO_2). Indeed, in the pore size distribution C-HAT-550 has obviously smaller sized pores while Vac-550 has further broader pore width whose pore size is similar to that of Vac-HAT-700 or C-HAT-700 which is also clearly shown on the curves in log scale (**Figure 3.27**d and **Figure S12**).

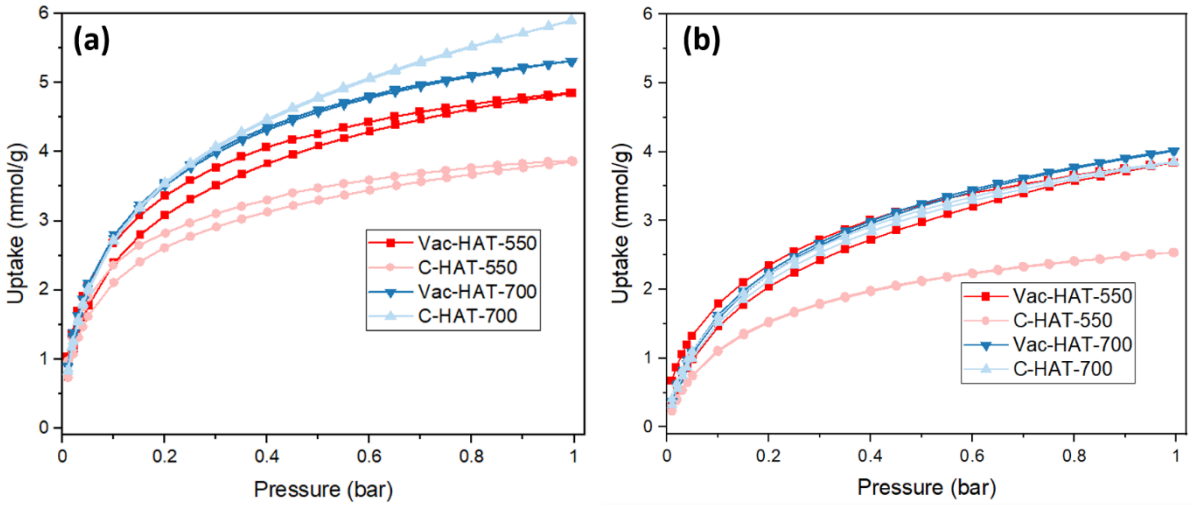

Figure 3.28 CO_2 physisorption isotherms of Vac-HAT-Ts and C-HAT-Ts at (a) 273 K, and (b) 298 K.

CO_2 physisorption measurements were carried out to further understand the micropore structure (**Figure 3.28**). Since it is measured up to 1 bar (p/p_0 ~ 0.03), the level of mono/multilayer is filled in the micropores of materials. The total uptake of CO_2 in Vac-HAT-550 at 273 K (**Figure 3.28**a) is 4.9 mmol g^{-1} which is significantly higher than C-HAT-550 of 3.9 mmol g^{-1}. On the other hand, at higher temperature of 298 K, the total uptake in all samples overall decreased compared to 273 K because raising the temperature brings the increased internal energy of CO_2, the fast diffusion, but it also brings the decreased fixed adsorption sites at the same time (**Figure 3.28**b).[279] Vac-HAT-700 and C-HAT-700 have comparable amount of pores reaching by CO_2 in 273K (5.3 and 5.8 mmol g^{-1}, respectively) and 298K (3.8 and 3.9 mmol g^{-1}, respectively) showing the pore construction independency of vacuum.

When the pore volume distribution of samples are calculated with NLDFT model (CO_2 at 273 K on carbon) from the CO_2 isotherms (**Table 5**), the micropore volume is different with that of from N_2 results. For example, a micropore volume of C-HAT-550 is 0.21 $cm^3\ g^{-1}$ from CO_2 isotherm, but only 0.09 $cm^3\ g^{-1}$ from N_2 isotherm. Considering that very small micropores are approachable by CO_2 due to the adsorption condition of the CO_2 gas at 273 K up to 1 bar, it can be concluded that a very narrow micropore system in which the N_2 molecules can not access exists in C-HAT-550 so that resulting in a difference between the micropore volume from N_2 and CO_2 physisorption.

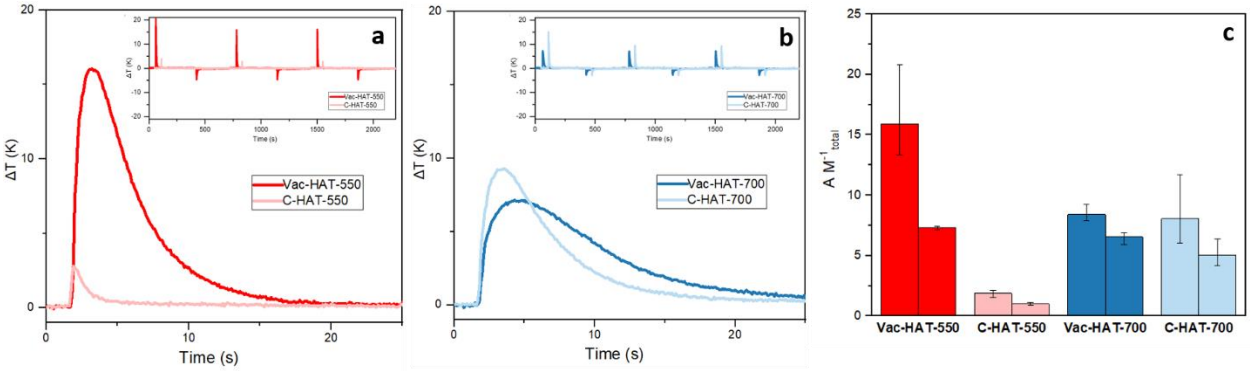

Figure 3.29 Thermal response measurement of n-butane (1 bar, 298 K) of (a) Vac-HAT-550 and C-HAT-550, (b) Vac-HAT-700 and C-HAT-700 of adsorption in 3rd cycle (insets: 3 cycles of thermal response measurements), and (c) integrated adsorption and desorption peak areas (left and right bar, respectively) normalized by the total mass.

Thermal response measurement with the InfraSORP technique using n-butane as a test gas reveal further details of the pore structure of the four samples (**Figure 3.29**). In the measurement conditions of 1 bar at 298 K corresponding to the relative pressure of n-butane is p/p_0 =0.4, the micropores and partial mesopores of materials are filled with this test gas during adsorption leaving the bigger mesopores empty as only mono/multilayers of adsorption would take place.[208] That is, the larger peak of temperature change in graph represents the big micropores and mesopores are rapidly filled with the gas out of their interior. The height of adsorption peak of Vac-HAT-550 (ΔT = 15 – 20K) coming from the release of heat during the adsorption of gas molecules in the pores are significantly higher than that of C-HAT-550 (ΔT < 2.5 K). The integral area of Vac-HAT-550 is also about as 8.5 times as that of C-HAT-550, indicating that Vac-HAT-550 has a portion of big micropore and small mesopore system than C-HAT-550 even if the same carbonization temperature is used. As there is no enough time to reach to the equilibrium in the measurement, only kinetically favorable adsorption could happen.[208,280] By introducing the vacuum during condensation the different pore structure has been formed and the amount of pores

available for utilization has considerably increased in Vac-HAT-550. Meanwhile, the ΔT between adsorption and desorption is asymmetric especially in Vac-HAT-550 and C-HAT-550 as the diffusion of n-butane out of the narrow pores is relatively slower during the desorption. Regarding to Vac-HAT-700 and C-HAT-700, both peaks and their area integrals are similar each other, which can be seen that a similar micropore or small mesopore structure is formed at this temperature regardless of vacuum or inert conditions. One noticeable difference is that the C-HAT-700 shows a higher peak (ΔT ~10 K) at the beginning of the adsorption, this might be because of a relatively large micropore structure in C-HAT-700 as mentioned earlier. According to the normalized peak area by the weight of the measured sample, the heat-treated samples at 700 °C are similar revealing about ~ 8.4, while Vac-HAT-550 and C-HAT-550 show 16 and 1.9, respectively (**Figure 3.29**c). As a higher value in it means to have a large pore accessible by butane gas, it can be seen that Vac-HAT-550 has the higher amount of large pores in the same line as the pore structure analysis from isotherms.

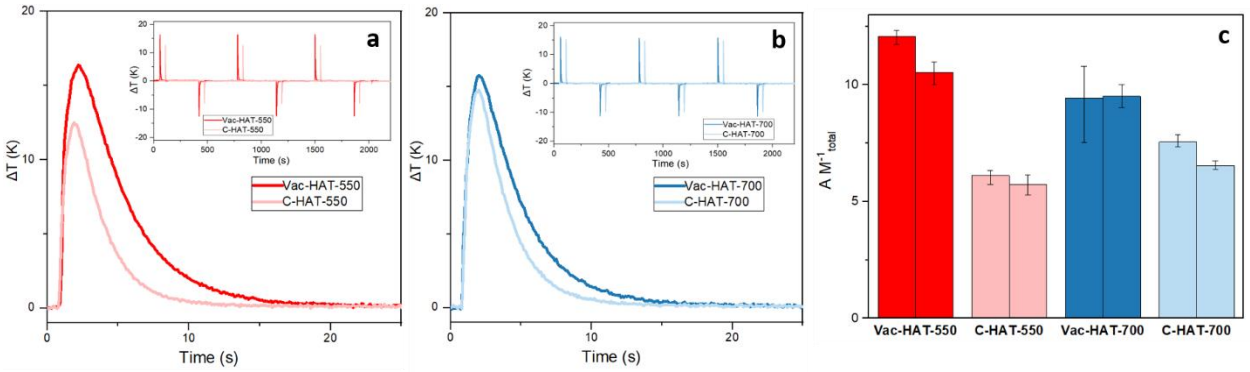

Figure 3.30 Thermal response measurement of CO_2 (1 bar, 298 K) of (a) Vac-HAT-550 and C-HAT-550, (b) Vac-HAT-700 and C-HAT-700 of adsorption in 3rd cycle (insets: 3 cycles of thermal response measurements), and (c) integrated adsorption and desorption peak areas (left and right bar, respectively) normalized by the total mass.

The thermal response measurement is measured using CO_2 as another test gas that has smaller kinetic molecular size (0.34 nm) than n-butane (0.42 nm) to figure out the kinetic trends of the materials. Under the measurement conditions of 1 bar and 298 K, the relative pressure of CO_2 is $p/p_0 \sim 0.02$ in which the micropores are partially filled with the gas and the sufficient diffusion in the micropores pathways are available. All the samples show the relatively symmetrical curves of adsorption and desorption, revealing more rapid diffusions of the molecules are reversibly taking place in adsorption/desorption (**Figure 3.30**). When it comes to the integrated peak area, i.e., adsorption capacity, the value of Vac-HAT-550 (12.1) is as two times higher than that of C-HAT-550 (6.1). This difference is significantly large considering the pore volume of Vac-HAT-550 (0.28 $cm^3\ g^{-1}$) calculated from CO_2 isotherm is only 1.3 times higher compared to that of C-HAT-550 (0.21 $cm^3\ g^{-1}$). This means that the higher amount of micropores can be utilized as an adsorption capacity on Vac-HAT-550 than C-HAT-550 in the thermal response measurement where kinetic aspects are dominant in the short duration time of adsorption/desorption of gases. This is an important factor in terms of the utilization of the porous materials, because no matter how large the capacity, it is not ideal in various applications if the adsorption or desorption reaction takes such a long time.[24,281] On the other hand, this phenomenon can be seen in two samples carbonized 700 °C. The micropore volumes of Vac-HAT-700 from CO_2 physisorption is lower than C-HAT-700 showing 0.3 $cm^3\ g^{-1}$ and 0.37 $cm^3\ g^{-1}$, respectively, but in the peak area of the CO_2 infraSORP result, Vac-HAT-700 (9.4) is rather higher than C-HAT-700 (7.6). Although it is not a significant difference, this implies that CO_2 is highly accessible to the inner pores of C-HAT-700 in the equilibrium state, while it can be easily and highly utilized in Vac-HAT-700 in a quick

time duration. It is apparent that the pore structure is affected by the atmosphere of condensation, it seems that the effect is more obvious on the samples heat treated at 550 °C.

4. Conclusions and Perspectives

The aim of this thesis was to provide a profound understanding of nanoporous carbon materials by precisely designing their atomic construction and pore architecture by using molecular precursors. The structure-property relationships of the resulting materials have been tested in various environmental- and energy- related applications so that a profound structure-related performance can be understood. Ultimately, the advanced design of the heteroatom-containing porous carbon materials and their insights for the fundamentals on gas adsorption and electrochemical energy storage were addressed. Three main topics were complementary examined separately which are related to synthesis, structural characterization, and applications.

In the first topic (**Chapter 3.1**), the synthesis of sp^2-conjugated, heteroatom-rich, "carbonaceous" materials from economically feasible raw materials and salt templates was reported. In this topic, the porosity and polarity affected by salts and the role of the salts in heteroatom stabilization have been especially shown. Low cost citrazinic acid (2,6-dihydroxy-4-pyridinecarboxylic acid) and melamine are used as components of a microporous, amorphous framework, where edges of the covalent frameworks were tightly terminated with nitrogen and oxygen moieties. $ZnCl_2$ as the porogen stabilized structural microporosity as well as nitrogen and oxygen heteroatoms up to comparably high condensation temperatures of 750 and 950 °C (**Chapter 3.1.2**). The specific surface area up to 1265 $m^2\ g^{-1}$ was in the 1.5 nm supermicropore range and typical for heteroatom-rich carbon materials (nitrogen of up to 20 wt. %, oxygen contents of up to 19 wt.%,) with such structural porosity (**Chapter 3.1.3**). The unusually high heteroatom content revealed that the edges

and pores of the covalent structures are tightly lined with heteroatoms, while C-C or C-H bonds are expected to have a minor contribution.

Adsorption of water vapor and carbon dioxide were exemplarily chosen to illustrate the impact of this heteroatom functionalization under salt-templating conditions on the adsorption properties of the materials. 27.10 mmol g^{-1} of H_2O uptake of (at $p/p_0 = 0.9$) can be achieved, which also proves the very hydrophilic character of the pore walls, while the maximum CO_2 uptake (at 273 K) is 5.3 mmol g^{-1}. At the same time the CO_2/N_2 adsorption selectivity at 273 K reached values of up to 60. All these values were beyond ordinary high surface area carbons, also differ from N-doped carbons, and are much closer to organized framework species, such as C_2N.

The controlled thermal condensation of precursor molecules and advanced functional properties on applications of the synthesized porous carbons has been described (**Chapter 3.2**). The porous carbon materials with high heteroatom content from pre-condensed citrazinic acid and melamine as abundant and simple molecules in salt melts were synthesized and analyzed by various structural characterization techniques. The structural characterization of synthesized materials revealed their specific porosity, chemical composition, and morphology, and difference interactions with various adsorbates. The materials with their own specific characteristics acquired by only modulating the condensation temperature were used as various applications. A clear change was observed between the precursor materials and the carbonized samples through solid-state NMR, disordered structures and related to sp^2-hybridized carbons were formed as the condensation temperature increased according to NMR signal width. Considering the functional groups from FTIR, the pre-condensed material was likely a modified form of indigoidine molecules which have continuously sp^2-conjugated carbons so that stable and conductive carbon materials can be obtained in a controlled

condensation (**Chapter 3.2.2**). The resulting materials have different porosity and atomic construction exhibiting a high nitrogen content up to 25 wt. % as well as a high porosity with a specific surface area of more than 1800 m^2 g^{-1}, and a high performance in selective CO_2 gas adsorption of 62.7. These pore structure as well as properties of surface have affected water adsorption showing a remarkably high Q_{st} of over 100 kJ mol^{-1}, significantly higher than that of zeolites (50 – 80 kJ mol^{-1}) or $CaCl_2$ (~80 kJ mol^{-1}) known as competent adsorbents (**Chapter 3.2.3**). Based on the EDLCs behavior, 120 F g^{-1} at 0.1 A g^{-1} with a highly symmetric triangular shape was shown in porous carbon materials condensed at high temperature in an aqueous based electrolyte environment. DSC measurements revealed that the pore structure of the material and the interaction of the material with water are considered as important factors as the change in the configuration of the water within the pores.

A C_2N-type nitrogen-doped carbon by template-free synthesis, that is C-HAT-CN, has been described as the third topic where the mechanisms of the formation of the pore structure inside the particle in the materials were investigated (**Chapter 3.3**). The shape of particles or the elemental composition of C/N were not affected by vacuum atmosphere in the condensation compared to inert gas flow conditions, but did change the overall pore structure. A high porosity of 720 m^2 g^{-1} and 0.5 cm^3 g^{-1} according to specific surface area and pore volume from N_2 isotherms was respectively introduced in vacuum environment, whereas a relatively lower porosity was formed as 430 m^2 g^{-1} and 0.25 cm^3 g^{-1} in an inert atmosphere, and this clear difference showed up especially at a temperature of 550 °C. This was also ascribed not only in the CO_2 isotherm, but also in the thermal response measurement using various gases as test gases. That is, the amount of pores available for utilization has considerably increased by introducing high amount of larger

micropores and mesopores when the vacuum was used for the condensation while similar micropore/mesopore structures were maintained at higher temperature of 700 °C regardless of vacuum or inert conditions. The pore structure of HAT-CN-derived carbon materials during condensation in vacuum could be fundamentally understood which is essential to maximize the utilization of porous system in materials.

In conclusion, the molecular designs of heteroatom containing porous carbon derived from abundant and simple molecules have been introduced in the presented thesis. Abundant precursors that already containing high amount of nitrogen or oxygen were beneficial to achieve enhanced interaction with adsorptives. The physical and chemical properties of these heteroatom-doped porous carbons are affected by mainly two parameters, that is, the porosity from the pore structure and the polarity from the atomic composition on the surface. In other words, controlling the porosity as well as the polarity of the carbon materials is important to understand interactions with different guest species which is a fundamental knowledge for the utilization on various applications. The salt-templating approach to fabricate the fine-tuned microporosity and atomic composition has been demonstrated and the enhanced uptake and selectivity of the materials in gas physisorptions has been shown. The presence of narrow micropore structures led to a highly enhanced gas adsorptions, and the introducing of heteroatom species on the surface even provided additional functional sites so that the polar guest species are further chemically attracted which is, for example, proved by CO_2 selectivity over N_2, adsorption heat capacity of H_2O on the materials, and the aqueous electrolyte- based electrochemical capacitance. The pore and atomic structure-related fundamental studies on the porous carbon materials could pave the way for the porous

carbons, a promising next- generation materials to be used in a wide range of applications in fields relevant for environment and energy storage.

5. References

1. International Energy Agency (IEA) (https://www.iea.org/analysis).
2. Global Energy Review 2020 (https://www.iea.org/reports/global-energy-review-2020).
3. Increase of the atmospheric CO2 concentration measured during 1958–2015 at the Mauna Loa (Hawaii).
4. Oschatz, M.; Antonietti, M., A search for selectivity to enable CO 2 capture with porous adsorbents. *Energy Environ. Sci.* **2018,** *11* (1), 57-70.
5. Communication from the Commision to the European parliament, The councel, The European economic and social committee and the committee of the regions, The 2030 Climatetargetplan, COM(2020) 562 final, Brussels, 17.9.2020.
6. Special Report on Global Warming of 1.5 ºC. Incheon, Republic of Korea: Intergovernmental Panel on Climate Change (IPCC). 8 October 2018. Retrieved 7 October 2018.
7. Irlam, L., Global costs of carbon capture and storage. *Global CCS Institute, Melbourne, Australia* **2017**.
8. Danckwerts, P., The reaction of CO2 with ethanolamines. *Chem. Eng. Sci.* **1979,** *34* (4), 443-446.
9. Versteeg, G.; Van Dijck, L.; van Swaaij, W. P. M., On the kinetics between CO2 and alkanolamines both in aqueous and non-aqueous solutions. An overview. *Chem. Eng. Commun.* **1996,** *144* (1), 113-158.
10. Arstad, B.; Blom, R.; Swang, O., CO2 absorption in aqueous solutions of alkanolamines: mechanistic insight from quantum chemical calculations. *J. Phys. Chem. A.* **2007,** *111* (7), 1222-1228.
11. Sun, W.-C.; Yong, C.-B.; Li, M.-H., Kinetics of the absorption of carbon dioxide into mixed aqueous solutions of 2-amino-2-methyl-l-propanol and piperazine. *Chem. Eng. Sci.* **2005,** *60* (2), 503-516.
12. Closmann, F.; Nguyen, T.; Rochelle, G. T., MDEA/Piperazine as a solvent for CO2 capture. *Energy Procedia* **2009,** *1* (1), 1351-1357.
13. Kim, S.; Shi, H.; Lee, J. Y., CO2 absorption mechanism in amine solvents and enhancement of CO2 capture capability in blended amine solvent. *Int. J. Greenh. Gas Control.* **2016,** *45*, 181-188.
14. Barrer, R. M., *Hydrothermal chemistry of zeolites*. Academic press: 1982.
15. Dong, F.; Lou, H.; Kodama, A.; Goto, M.; Hirose, T., The Petlyuk PSA process for the separation of ternary gas mixtures: exemplification by separating a mixture of CO2–CH4–N2. *Sep. Purif. Technol.* **1999,** *16* (2), 159-166.
16. Jadhav, P.; Chatti, R.; Biniwale, R.; Labhsetwar, N.; Devotta, S.; Rayalu, S., Monoethanol amine modified zeolite 13X for CO2 adsorption at different temperatures. *Energy Fuels* **2007,** *21* (6), 3555-3559.
17. Liang, Z.; Marshall, M.; Chaffee, A. L., CO2 adsorption-based separation by metal organic framework (Cu-BTC) versus zeolite (13X). *Energy Fuels* **2009,** *23* (5), 2785-2789.
18. Xia, Y.; Mokaya, R.; Walker, G. S.; Zhu, Y., Superior CO2 adsorption capacity on N-doped, high-surface-area, microporous carbons templated from zeolite. *Adv. Energy Mater.* **2011,** *1* (4), 678-683.
19. Li, H.; Eddaoudi, M.; O'Keeffe, M.; Yaghi, O. M., Design and synthesis of an exceptionally stable and highly porous metal-organic framework. *nature* **1999,** *402* (6759), 276-279.
20. Hönicke, I. M.; Senkovska, I.; Bon, V.; Baburin, I. A.; Bönisch, N.; Raschke, S.; Evans, J. D.; Kaskel, S., Balancing mechanical stability and ultrahigh porosity in crystalline framework materials. *Angew. Chem. Int. Ed.* **2018,** *57* (42), 13780-13783.
21. Eddaoudi, M.; Kim, J.; Rosi, N.; Vodak, D.; Wachter, J.; O'Keeffe, M.; Yaghi, O. M., Systematic design of pore size and functionality in isoreticular MOFs and their application in methane storage. *Science* **2002,** *295* (5554), 469-472.
22. Chui, S. S.-Y.; Lo, S. M.-F.; Charmant, J. P.; Orpen, A. G.; Williams, I. D., A chemically functionalizable nanoporous material [Cu3 (TMA) 2 (H2O) 3] n. *Science* **1999,** *283* (5405), 1148-1150.
23. Yang, Q.; Zhong, C., Molecular simulation of carbon dioxide/methane/hydrogen mixture adsorption in metal− organic frameworks. *J. Phys. Chem. B.* **2006,** *110* (36), 17776-17783.

24. Nugent, P.; Belmabkhout, Y.; Burd, S. D.; Cairns, A. J.; Luebke, R.; Forrest, K.; Pham, T.; Ma, S.; Space, B.; Wojtas, L., Porous materials with optimal adsorption thermodynamics and kinetics for CO 2 separation. *Nature* **2013,** *495* (7439), 80-84.
25. Lee, J.; Kim, J.; Hyeon, T., Recent progress in the synthesis of porous carbon materials. *Adv. Mater.* **2006,** *18* (16), 2073-2094.
26. Liang, C.; Li, Z.; Dai, S., Mesoporous carbon materials: synthesis and modification. *Angew. Chem. Int. Ed.* **2008,** *47* (20), 3696-3717.
27. Stein, A.; Wang, Z.; Fierke, M. A., Functionalization of porous carbon materials with designed pore architecture. *Adv. Mater.* **2009,** *21* (3), 265-293.
28. Morishita, T.; Tsumura, T.; Toyoda, M.; Przepiórski, J.; Morawski, A.; Konno, H.; Inagaki, M., A review of the control of pore structure in MgO-templated nanoporous carbons. *Carbon* **2010,** *48* (10), 2690-2707.
29. Presser, V.; Heon, M.; Gogotsi, Y., Carbide-derived carbons–from porous networks to nanotubes and graphene. *Adv. Funct. Mater.* **2011,** *21* (5), 810-833.
30. Liu, J.; Wickramaratne, N. P.; Qiao, S. Z.; Jaroniec, M., Molecular-based design and emerging applications of nanoporous carbon spheres. *Nat. Mater.* **2015,** *14* (8), 763-774.
31. Definition of oxidation state for carbon (https://courses.lumenlearning.com/suny-potsdam-organicchemistry2/chapter/19-1-definition-of-oxidation-state-for-carbon/).
32. Kroll, J. H.; Donahue, N. M.; Jimenez, J. L.; Kessler, S. H.; Canagaratna, M. R.; Wilson, K. R.; Altieri, K. E.; Mazzoleni, L. R.; Wozniak, A. S.; Bluhm, H., Carbon oxidation state as a metric for describing the chemistry of atmospheric organic aerosol. *Nat. Chem.* **2011,** *3* (2), 133-139.
33. Haley, M. M.; Tykwinski, R. R., *Carbon-Rich Compounds: From Molecules to Materials*. Wiley: 2006.
34. Kharisov, B. I.; Kharissova, O. V., Conventional Carbon Allotropes. In *Carbon Allotropes: Metal-Complex Chemistry, Properties and Applications*, Springer: 2019; pp 9-33.
35. Taft, E.; Philipp, H., Optical properties of graphite. *Phys. Rev.* **1965,** *138* (1A), A197.
36. Novoselov, K. S.; Geim, A. K.; Morozov, S. V.; Jiang, D.; Zhang, Y.; Dubonos, S. V.; Grigorieva, I. V.; Firsov, A. A., Electric field effect in atomically thin carbon films. *science* **2004,** *306* (5696), 666-669.
37. Nair, R. R.; Blake, P.; Grigorenko, A. N.; Novoselov, K. S.; Booth, T. J.; Stauber, T.; Peres, N. M.; Geim, A. K., Fine structure constant defines visual transparency of graphene. *Science* **2008,** *320* (5881), 1308-1308.
38. Balandin, A. A.; Ghosh, S.; Bao, W.; Calizo, I.; Teweldebrhan, D.; Miao, F.; Lau, C. N., Superior thermal conductivity of single-layer graphene. *Nano Lett.* **2008,** *8* (3), 902-907.
39. Morozov, S.; Novoselov, K.; Katsnelson, M.; Schedin, F.; Elias, D.; Jaszczak, J. A.; Geim, A., Giant intrinsic carrier mobilities in graphene and its bilayer. *Phys. Rev. Lett.* **2008,** *100* (1), 016602.
40. Bolotin, K. I.; Sikes, K. J.; Jiang, Z.; Klima, M.; Fudenberg, G.; Hone, J. e.; Kim, P.; Stormer, H., Ultrahigh electron mobility in suspended graphene. *Solid State Commun.* **2008,** *146* (9-10), 351-355.
41. Iijima, S., Helical microtubules of graphitic carbon. *nature* **1991,** *354* (6348), 56-58.
42. Mintmire, J. W.; Dunlap, B. I.; White, C. T., Are fullerene tubules metallic? *Phys. Rev. Lett.* **1992,** *68* (5), 631.
43. Hamada, N.; Sawada, S.-i.; Oshiyama, A., New one-dimensional conductors: Graphitic microtubules. *Phys. Rev. Lett.* **1992,** *68* (10), 1579.
44. Treacy, M. J.; Ebbesen, T. W.; Gibson, J. M., Exceptionally high Young's modulus observed for individual carbon nanotubes. *nature* **1996,** *381* (6584), 678-680.
45. Forro, L.; Salvetat, J.-P.; Bonard, J.-M.; Bacsa, R.; Thomson, N.; Garaj, S.; Thien-Nga, L.; Gaal, R.; Kulik, A.; Ruzicka, B., Electronic and mechanical properties of carbon nanotubes. In *Science and Application of Nanotubes*, Springer: 2002; pp 297-320.
46. Astefanei, A.; Núñez, O.; Galceran, M. T., Characterisation and determination of fullerenes: a critical review. *Anal. Chim. Acta* **2015,** *882*, 1-21.

47. Palmer, J.; Llobet, A.; Yeon, S.-H.; Fischer, J.; Shi, Y.; Gogotsi, Y.; Gubbins, K., Modeling the structural evolution of carbide-derived carbons using quenched molecular dynamics. *Carbon* **2010,** *48* (4), 1116-1123.
48. Oschatz, M.; Walczak, R., Crucial factors for the application of functional nanoporous carbon-based materials in energy and environmental applications. *C Journal of Carbon Research* **2018,** *4* (4), 56.
49. Ryoo, R.; Joo, S. H.; Jun, S., Synthesis of highly ordered carbon molecular sieves via template-mediated structural transformation. *J. Phys. Chem. B* **1999,** *103* (37), 7743-7746.
50. Wang, H.; Gao, Q.; Hu, J., High hydrogen storage capacity of porous carbons prepared by using activated carbon. *J. Am. Chem. Soc.* **2009,** *131* (20), 7016-7022.
51. Hao, G. P.; Li, W. C.; Qian, D.; Lu, A. H., Rapid synthesis of nitrogen-doped porous carbon monolith for CO2 capture. *Adv. Mater.* **2010,** *22* (7), 853-857.
52. Radovic, L. R.; Moreno-Castilla, C.; Rivera-Utrilla, J., Carbon materials as adsorbents in aqueous solutions. *Chem. Phys. Carbon.* **2001**, 227-406.
53. Serp, P.; Figueiredo, J. L., *Carbon materials for catalysis*. Wiley Online Library: 2009.
54. Yu, J.-S.; Kang, S.; Yoon, S. B.; Chai, G., Fabrication of ordered uniform porous carbon networks and their application to a catalyst supporter. *J. Am. Chem. Soc.* **2002,** *124* (32), 9382-9383.
55. Reed, M.; Brodd, R., Porous carbon for fuel cell electrodes. *Carbon* **1965,** *3* (3), 241-246.
56. Vix-Guterl, C.; Frackowiak, E.; Jurewicz, K.; Friebe, M.; Parmentier, J.; Béguin, F., Electrochemical energy storage in ordered porous carbon materials. *Carbon* **2005,** *43* (6), 1293-1302.
57. Yan, R.; Antonietti, M.; Oschatz, M., Toward the experimental understanding of the energy storage mechanism and ion dynamics in ionic liquid based supercapacitors. *Adv. Energy Mater.* **2018,** *8* (18), 1800026.
58. Gupta, V. K.; Saleh, T. A., Sorption of pollutants by porous carbon, carbon nanotubes and fullerene-an overview. *Environ. Sci. Pollut. Res.* **2013,** *20* (5), 2828-2843.
59. Burchell, T. D., *Carbon materials for advanced technologies*. Elsevier: 1999.
60. Eatemadi, A.; Daraee, H.; Karimkhanloo, H.; Kouhi, M.; Zarghami, N.; Akbarzadeh, A.; Abasi, M.; Hanifehpour, Y.; Joo, S. W., Carbon nanotubes: properties, synthesis, purification, and medical applications. *Nanoscale Res. Lett.* **2014,** *9* (1), 1-13.
61. Conventional Carbon Allotropes (https://link.springer.com/chapter/10.1007/978-3-030-03505-1_2).
62. Allotropes of Carbon (https://courses.lumenlearning.com/introchem/chapter/allotropes-of-carbon/).
63. Kyotani, T., Control of pore structure in carbon. *Carbon* **2000,** *38* (2), 269-286.
64. Liu, L.; Zeng, G.; Chen, J.; Bi, L.; Dai, L.; Wen, Z., N-doped porous carbon nanosheets as pH-universal ORR electrocatalyst in various fuel cell devices. *Nano Energy* **2018,** *49*, 393-402.
65. Chen, S.; Li, Y.; Mi, L., Porous carbon derived from metal organic framework for gas storage and separation: the size effect. *Inorg. Chem. Commun.* **2020,** *118*, 107999.
66. Borghei, M.; Laocharoen, N.; Kibena-Põldsepp, E.; Johansson, L.-S.; Campbell, J.; Kauppinen, E.; Tammeveski, K.; Rojas, O. J., Porous N, P-doped carbon from coconut shells with high electrocatalytic activity for oxygen reduction: alternative to Pt-C for alkaline fuel cells. *Appl. Catal. B.* **2017,** *204*, 394-402.
67. Yang, J.; Xiang, F.; Guo, H.; Wang, L.; Niu, X., Honeycomb-like porous carbon with N and S dual-doping as metal-free catalyst for the oxygen reduction reaction. *Carbon* **2020,** *156*, 514-522.
68. Thommes, M.; Kaneko, K.; Neimark, A. V.; Olivier, J. P.; Rodriguez-Reinoso, F.; Rouquerol, J.; Sing, K. S., Physisorption of gases, with special reference to the evaluation of surface area and pore size distribution (IUPAC Technical Report). *Pure Appl. Chem.* **2015,** *87* (9-10), 1051-1069.
69. Thrower, P. A., *Chemistry & Physics of Carbon: Volume 25*. CRC Press: 1996; Vol. 25.
70. Çeçen, F.; Aktas, Ö., *Activated carbon for water and wastewater treatment: Integration of adsorption and biological treatment*. John Wiley & Sons: 2011.
71. Chmiola, J.; Yushin, G.; Gogotsi, Y.; Portet, C.; Simon, P.; Taberna, P.-L., Anomalous increase in carbon capacitance at pore sizes less than 1 nanometer. *science* **2006,** *313* (5794), 1760-1763.

72. Raymundo-Pinero, E.; Kierzek, K.; Machnikowski, J.; Béguin, F., Relationship between the nanoporous texture of activated carbons and their capacitance properties in different electrolytes. *Carbon* **2006,** *44* (12), 2498-2507.
73. Ebie, K., Effect of pore size distribution of activated carbon on the adsorption of humic substances and trace organic compounds. *Water Supply* **1995,** *13*, 65-70.
74. Siriwardane, R. V.; Shen, M.-S.; Fisher, E. P.; Poston, J. A., Adsorption of CO2 on molecular sieves and activated carbon. *Energy Fuels* **2001,** *15* (2), 279-284.
75. O'koye, I.; Benham, M.; Thomas, K., Adsorption of gases and vapors on carbon molecular sieves. *Langmuir* **1997,** *13* (15), 4054-4059.
76. Wahby, A.; Ramos-Fernández, J. M.; Martínez-Escandell, M.; Sepúlveda-Escribano, A.; Silvestre-Albero, J.; Rodríguez-Reinoso, F., High-surface-area carbon molecular sieves for selective CO2 adsorption. *ChemSusChem* **2010,** *3* (8), 974-981.
77. Miura, K.; Hayashi, J.; Hashimoto, K., Production of molecular sieving carbon through carbonization of coal modified by organic additives. *Carbon* **1991,** *29* (4-5), 653-660.
78. Ma, Z.; Kyotani, T.; Tomita, A., Synthesis methods for preparing microporous carbons with a structural regularity of zeolite Y. *Carbon* **2002,** *40* (13), 2367-2374.
79. Stadie, N. P.; Wang, S.; Kravchyk, K. V.; Kovalenko, M. V., Zeolite-templated carbon as an ordered microporous electrode for aluminum batteries. *ACS nano* **2017,** *11* (2), 1911-1919.
80. Li, Z.; Yuan, L.; Yi, Z.; Sun, Y.; Liu, Y.; Jiang, Y.; Shen, Y.; Xin, Y.; Zhang, Z.; Huang, Y., Insight into the electrode mechanism in lithium-sulfur batteries with ordered microporous carbon confined sulfur as the cathode. *Adv. Energy Mater.* **2014,** *4* (7), 1301473.
81. Hu, Z.; Srinivasan, M. P.; Ni, Y., Preparation of mesoporous high-surface-area activated carbon. *Adv. Mater.* **2000,** *12* (1), 62-65.
82. Qie, L.; Chen, W.; Xu, H.; Xiong, X.; Jiang, Y.; Zou, F.; Hu, X.; Xin, Y.; Zhang, Z.; Huang, Y., Synthesis of functionalized 3D hierarchical porous carbon for high-performance supercapacitors. *Energy Environ. Sci.* **2013,** *6* (8), 2497-2504.
83. Wang, D. W.; Li, F.; Liu, M.; Lu, G. Q.; Cheng, H. M., 3D aperiodic hierarchical porous graphitic carbon material for high-rate electrochemical capacitive energy storage. *Angew. Chem. Int. Ed.* **2008,** *47* (2), 373-376.
84. Li, Y.; Fu, Z. Y.; Su, B. L., Hierarchically structured porous materials for energy conversion and storage. *Adv. Funct. Mater.* **2012,** *22* (22), 4634-4667.
85. Su, F.; Zeng, J.; Bao, X.; Yu, Y.; Lee, J. Y.; Zhao, X., Preparation and characterization of highly ordered graphitic mesoporous carbon as a Pt catalyst support for direct methanol fuel cells. *Chem. Mater.* **2005,** *17* (15), 3960-3967.
86. Zhang, Y.; Liu, Y.; Liu, W.; Li, X.; Mao, L., Synthesis of honeycomb-like mesoporous nitrogen-doped carbon nanospheres as Pt catalyst supports for methanol oxidation in alkaline media. *Appl. Surf. Sci.* **2017,** *407*, 64-71.
87. Trogadas, P.; Fuller, T. F.; Strasser, P., Carbon as catalyst and support for electrochemical energy conversion. *Carbon* **2014,** *75*, 5-42.
88. Yan, Z.; Gao, L.; Dai, C.; Zhang, M.; Lv, X.; Shen, P. K., Metal-free mesoporous carbon with higher contents of active N and S codoping by template method for superior ORR efficiency to Pt/C. *Int. J. Hydrog. Energy* **2018,** *43* (7), 3705-3715.
89. Liu, J.; Wu, X.; Yang, L.; Wang, F.; Yin, J., Unprotected Pt nanoclusters anchored on ordered mesoporous carbon as an efficient and stable catalyst for oxygen reduction reaction. *Electrochim. Acta* **2019,** *297*, 539-544.
90. Ryoo, R.; Joo, S. H.; Kruk, M.; Jaroniec, M., Ordered mesoporous carbons. *Adv. Mater.* **2001,** *13* (9), 677-681.
91. Chen, Y.; Liu, Q.; Wang, J., Carbon dioxide activated carbon nanofibers with hierarchical micro-/mesoporosity towards electrocatalytic oxygen reduction. *J. Mater. Chem. A.* **2016,** *4* (15), 5553-5560.

92. Molina-Sabio, M.; Gonzalez, M.; Rodriguez-Reinoso, F.; Sepúlveda-Escribano, A., Effect of steam and carbon dioxide activation in the micropore size distribution of activated carbon. *Carbon* **1996,** *34* (4), 505-509.
93. Kim, P.; Agnihotri, S., Application of water–activated carbon isotherm models to water adsorption isotherms of single-walled carbon nanotubes. *J. Colloid Interface Sci.* **2008,** *325* (1), 64-73.
94. Ahmadpour, A.; Do, D., The preparation of active carbons from coal by chemical and physical activation. *Carbon* **1996,** *34* (4), 471-479.
95. Romanos, J.; Beckner, M.; Rash, T.; Firlej, L.; Kuchta, B.; Yu, P.; Suppes, G.; Wexler, C.; Pfeifer, P., Nanospace engineering of KOH activated carbon. *Nanotechnology* **2011,** *23* (1), 015401.
96. Babel, K.; Jurewicz, K., KOH activated carbon fabrics as supercapacitor material. *J. Phys. Chem. Solids.* **2004,** *65* (2-3), 275-280.
97. Caturla, F.; Molina-Sabio, M.; Rodriguez-Reinoso, F., Preparation of activated carbon by chemical activation with ZnCl2. *Carbon* **1991,** *29* (7), 999-1007.
98. Nakagawa, Y.; Molina-Sabio, M.; Rodríguez-Reinoso, F., Modification of the porous structure along the preparation of activated carbon monoliths with H3PO4 and ZnCl2. *Microporous Mesoporous Mater.* **2007,** *103* (1-3), 29-34.
99. Prahas, D.; Kartika, Y.; Indraswati, N.; Ismadji, S., Activated carbon from jackfruit peel waste by H3PO4 chemical activation: Pore structure and surface chemistry characterization. *Chem. Eng. J.* **2008,** *140* (1-3), 32-42.
100. Nowrouzi, M.; Younesi, H.; Bahramifar, N., High efficient carbon dioxide capture onto as-synthesized activated carbon by chemical activation of Persian Ironwood biomass and the economic pre-feasibility study for scale-up. *J. Clean. Prod.* **2017,** *168*, 499-509.
101. Williams, P. T.; Reed, A. R., Development of activated carbon pore structure via physical and chemical activation of biomass fibre waste. *Biomass Bioenergy* **2006,** *30* (2), 144-152.
102. Jun, S.; Joo, S. H.; Ryoo, R.; Kruk, M.; Jaroniec, M.; Liu, Z.; Ohsuna, T.; Terasaki, O., Synthesis of new, nanoporous carbon with hexagonally ordered mesostructure. *J. Am. Chem. Soc.* **2000,** *122* (43), 10712-10713.
103. Huang, Y.; Gong, Q.; Song, X.; Feng, K.; Nie, K.; Zhao, F.; Wang, Y.; Zeng, M.; Zhong, J.; Li, Y., Mo2C nanoparticles dispersed on hierarchical carbon microflowers for efficient electrocatalytic hydrogen evolution. *ACS nano* **2016,** *10* (12), 11337-11343.
104. Kresge, C.; Leonowicz, M.; Roth, W. J.; Vartuli, J.; Beck, J., Ordered mesoporous molecular sieves synthesized by a liquid-crystal template mechanism. *nature* **1992,** *359* (6397), 710-712.
105. Yang, P.; Zhao, D.; Margolese, D. I.; Chmelka, B. F.; Stucky, G. D., Generalized syntheses of large-pore mesoporous metal oxides with semicrystalline frameworks. *Nature* **1998,** *396* (6707), 152-155.
106. Brinker, C. J.; Lu, Y.; Sellinger, A.; Fan, H., Evaporation-induced self-assembly: nanostructures made easy. *Adv. Mater.* **1999,** *11* (7), 579-585.
107. Zhao, D.; Feng, J.; Huo, Q.; Melosh, N.; Fredrickson, G. H.; Chmelka, B. F.; Stucky, G. D., Triblock copolymer syntheses of mesoporous silica with periodic 50 to 300 angstrom pores. *science* **1998,** *279* (5350), 548-552.
108. Sakamoto, Y.; Kaneda, M.; Terasaki, O.; Zhao, D. Y.; Kim, J. M.; Stucky, G.; Shin, H. J.; Ryoo, R., Direct imaging of the pores and cages of three-dimensional mesoporous materials. *Nature* **2000,** *408* (6811), 449-453.
109. Ryoo, R.; Kim, J. M.; Ko, C. H.; Shin, C., Disordered molecular sieve with branched mesoporous channel network. *J. Phys. Chem. A.* **1996,** *100* (45), 17718-17721.
110. Smarsly, B.; Antonietti, M., Block copolymer assemblies as templates for the generation of mesoporous inorganic materials and crystalline films. *Eur. J. Inorg. Chem.* **2006,** *2006* (6), 1111-1119.
111. Oh, S.; Kim, K., Synthesis of a new mesoporous carbon and its application to electrochemical double-layer capacitors. *Chem. Commun.* **1999,** (21), 2177-2178.
112. Jun, S.; Joo, S. H.; Ryoo, R.; Kruk, M.; Jaroniec, M.; Liu, Z.; Ohsuna, T.; Terasaki, O., Synthesis of new, nanoporous carbon with hexagonally ordered mesostructure. *Journal of the American Chemical Society* **2000,** *122* (43), 10712-10713.

113. Ji, X.; Lee, K. T.; Nazar, L. F., A highly ordered nanostructured carbon–sulphur cathode for lithium–sulphur batteries. *Nat. Mater.* **2009,** *8* (6), 500-506.
114. Joo, S. H.; Choi, S. J.; Oh, I.; Kwak, J.; Liu, Z.; Terasaki, O.; Ryoo, R., Ordered nanoporous arrays of carbon supporting high dispersions of platinum nanoparticles. *Nature* **2001,** *412* (6843), 169-172.
115. Oschatz, M.; Walczak, R., Crucial factors for the application of functional nanoporous carbon-based materials in energy and environmental applications. *C—Journal of Carbon Research* **2018,** *4* (4), 56.
116. McNaught, A. D.; Wilkinson, A., *Compendium of chemical terminology*. Blackwell Science Oxford: 1997; Vol. 1669.
117. Fechler, N.; Fellinger, T. P.; Antonietti, M., "Salt templating": a simple and sustainable pathway toward highly porous functional carbons from ionic liquids. *Adv. Mater.* **2013,** *25* (1), 75-79.
118. Díez, N.; Fuertes, A. B.; Sevilla, M., Molten salt strategies towards carbon materials for energy storage and conversion. *Energy Storage Mater.* **2021,** *38*, 50-69.
119. Yue, Z.; Mangun, C. L.; Economy, J., Preparation of fibrous porous materials by chemical activation: 1. ZnCl2 activation of polymer-coated fibers. *Carbon* **2002,** *40* (8), 1181-1191.
120. Shang, H.; Lu, Y.; Zhao, F.; Chao, C.; Zhang, B.; Zhang, H., Preparing high surface area porous carbon from biomass by carbonization in a molten salt medium. *RSC Adv.* **2015,** *5* (92), 75728-75734.
121. Sevilla, M.; Mokaya, R., Energy storage applications of activated carbons: supercapacitors and hydrogen storage. *Energy Environ. Sci.* **2014,** *7* (4), 1250-1280.
122. Cesano, F.; Rahman, M. M.; Bertarione, S.; Vitillo, J. G.; Scarano, D.; Zecchina, A., Preparation and adsorption properties of activated porous carbons obtained using volatile zinc templating phases. *Carbon* **2012,** *50* (5), 2047-2051.
123. Porada, S.; Schipper, F.; Aslan, M.; Antonietti, M.; Presser, V.; Fellinger, T. P., Capacitive Deionization using Biomass-based Microporous Salt-Templated Heteroatom-Doped Carbons. *ChemSusChem* **2015,** *8* (11), 1867-1874.
124. Molina-Sabio, M.; Rodrıguez-Reinoso, F., Role of chemical activation in the development of carbon porosity. *Colloids Surf. A* **2004,** *241* (1-3), 15-25.
125. Shaw, S. J.; Perry, G. S., LiCl-ZnCl2, phase diagram. *Thermochim. Acta* **1989,** *155*, 87-96.
126. Phase diagrams for the materials, https://www.metallab.net/chemsoc/alloys.php.
127. Liu, X.; Fechler, N.; Antonietti, M., Salt melt synthesis of ceramics, semiconductors and carbon nanostructures. *Chem. Soc. Rev.* **2013,** *42* (21), 8237-8265.
128. Dai, L.; Xue, Y.; Qu, L.; Choi, H.-J.; Baek, J.-B., Metal-free catalysts for oxygen reduction reaction. *Chem. Rev.* **2015,** *115* (11), 4823-4892.
129. Liu, X.; Dai, L., Carbon-based metal-free catalysts. *Nature Reviews Materials* **2016,** *1* (11), 1-12.
130. Du, F.; Yu, D.; Dai, L.; Ganguli, S.; Varshney, V.; Roy, A., Preparation of tunable 3D pillared carbon nanotube–graphene networks for high-performance capacitance. *Chem. Mater.* **2011,** *23* (21), 4810-4816.
131. Zhang, J.; Dai, L., Heteroatom-doped graphitic carbon catalysts for efficient electrocatalysis of oxygen reduction reaction. *ACS Catal.* **2015,** *5* (12), 7244-7253.
132. Wang, H.; Maiyalagan, T.; Wang, X., Review on recent progress in nitrogen-doped graphene: synthesis, characterization, and its potential applications. *ACS Catal.* **2012,** *2* (5), 781-794.
133. Hu, T.; Gerber, I. C., Theoretical study of the interaction of electron donor and acceptor molecules with graphene. *J. Phys. Chem. C.* **2013,** *117* (5), 2411-2420.
134. Mali, K. S.; Greenwood, J.; Adisoejoso, J.; Phillipson, R.; De Feyter, S., Nanostructuring graphene for controlled and reproducible functionalization. *Nanoscale* **2015,** *7* (5), 1566-1585.
135. Jiao, Y.; Zheng, Y.; Jaroniec, M.; Qiao, S. Z., Origin of the electrocatalytic oxygen reduction activity of graphene-based catalysts: a roadmap to achieve the best performance. *J. Am. Chem. Soc.* **2014,** *136* (11), 4394-4403.
136. Zhang, J.; Zhao, Z.; Xia, Z.; Dai, L., A metal-free bifunctional electrocatalyst for oxygen reduction and oxygen evolution reactions. *Nat. Nanotechnol.* **2015,** *10* (5), 444-452.
137. Lahaye, J.; Nanse, G.; Bagreev, A.; Strelko, V., Porous structure and surface chemistry of nitrogen containing carbons from polymers. *Carbon* **1999,** *37* (4), 585-590.

138. Gong, K.; Du, F.; Xia, Z.; Durstock, M.; Dai, L., Nitrogen-doped carbon nanotube arrays with high electrocatalytic activity for oxygen reduction. *science* **2009,** *323* (5915), 760-764.
139. Wang, X.; Lee, J. S.; Zhu, Q.; Liu, J.; Wang, Y.; Dai, S., Ammonia-treated ordered mesoporous carbons as catalytic materials for oxygen reduction reaction. *Chem. Mater.* **2010,** *22* (7), 2178-2180.
140. Mahurin, S. M.; Lee, J. S.; Wang, X.; Dai, S., Ammonia-activated mesoporous carbon membranes for gas separations. *J. Membr. Sci.* **2011,** *368* (1-2), 41-47.
141. Béguin, F.; Szostak, K.; Lota, G.; Frackowiak, E., A self-supporting electrode for supercapacitors prepared by one-step pyrolysis of carbon nanotube/polyacrylonitrile blends. *Adv. Mater.* **2005,** *17* (19), 2380-2384.
142. Shen, W.; Fan, W., Nitrogen-containing porous carbons: synthesis and application. *J. Mater. Chem. A.* **2013,** *1* (4), 999-1013.
143. Bhadra, B. N.; Vinu, A.; Serre, C.; Jhung, S. H., MOF-derived carbonaceous materials enriched with nitrogen: Preparation and applications in adsorption and catalysis. *Mater. Today* **2019,** *25*, 88-111.
144. Wang, Z.; Qie, L.; Yuan, L.; Zhang, W.; Hu, X.; Huang, Y., Functionalized N-doped interconnected carbon nanofibers as an anode material for sodium-ion storage with excellent performance. *Carbon* **2013,** *55*, 328-334.
145. Perovic, M.; Qin, Q.; Oschatz, M., From Molecular Precursors to Nanoparticles—Tailoring the Adsorption Properties of Porous Carbon Materials by Controlled Chemical Functionalization. *Adv. Funct. Mater.* **2020**, 1908371.
146. Terrones, M.; Terrones, H.; Grobert, N.; Hsu, W.; Zhu, Y.; Hare, J.; Kroto, H.; Walton, D.; Kohler-Redlich, P.; Rühle, M., Efficient route to large arrays of CN x nanofibers by pyrolysis of ferrocene/melamine mixtures. *Appl. Phys. Lett.* **1999,** *75* (25), 3932-3934.
147. Wang, X.; Li, X.; Zhang, L.; Yoon, Y.; Weber, P. K.; Wang, H.; Guo, J.; Dai, H., N-doping of graphene through electrothermal reactions with ammonia. *science* **2009,** *324* (5928), 768-771.
148. Tang, Y.; Allen, B. L.; Kauffman, D. R.; Star, A., Electrocatalytic activity of nitrogen-doped carbon nanotube cups. *J. Am. Chem. Soc.* **2009,** *131* (37), 13200-13201.
149. Matter, P. H.; Zhang, L.; Ozkan, U. S., The role of nanostructure in nitrogen-containing carbon catalysts for the oxygen reduction reaction. *J. Catal.* **2006,** *239* (1), 83-96.
150. Chen, S.; Bi, J.; Zhao, Y.; Yang, L.; Zhang, C.; Ma, Y.; Wu, Q.; Wang, X.; Hu, Z., Nitrogen-doped carbon nanocages as efficient metal-free electrocatalysts for oxygen reduction reaction. *Adv. Mater.* **2012,** *24* (41), 5593-5597.
151. Niwa, H.; Kobayashi, M.; Horiba, K.; Harada, Y.; Oshima, M.; Terakura, K.; Ikeda, T.; Koshigoe, Y.; Ozaki, J.-i.; Miyata, S., X-ray photoemission spectroscopy analysis of N-containing carbon-based cathode catalysts for polymer electrolyte fuel cells. *J. Power Sources* **2011,** *196* (3), 1006-1011.
152. Yu, D.; Zhang, Q.; Dai, L., Highly efficient metal-free growth of nitrogen-doped single-walled carbon nanotubes on plasma-etched substrates for oxygen reduction. *J. Am. Chem. Soc.* **2010,** *132* (43), 15127-15129.
153. Kundu, S.; Nagaiah, T. C.; Xia, W.; Wang, Y.; Dommele, S. V.; Bitter, J. H.; Santa, M.; Grundmeier, G.; Bron, M.; Schuhmann, W., Electrocatalytic activity and stability of nitrogen-containing carbon nanotubes in the oxygen reduction reaction. *J. Phys. Chem. C.* **2009,** *113* (32), 14302-14310.
154. Rao, C. V.; Cabrera, C. R.; Ishikawa, Y., In search of the active site in nitrogen-doped carbon nanotube electrodes for the oxygen reduction reaction. *J. Phys. Chem. Lett.* **2010,** *1* (18), 2622-2627.
155. Zhang, J.; Xia, Z.; Dai, L., Carbon-based electrocatalysts for advanced energy conversion and storage. *Sci. Adv.* **2015,** *1* (7), e1500564.
156. Niwa, H.; Horiba, K.; Harada, Y.; Oshima, M.; Ikeda, T.; Terakura, K.; Ozaki, J.-i.; Miyata, S., X-ray absorption analysis of nitrogen contribution to oxygen reduction reaction in carbon alloy cathode catalysts for polymer electrolyte fuel cells. *J. Power Sources* **2009,** *187* (1), 93-97.
157. Liu, R.; Wu, D.; Feng, X.; Müllen, K., Nitrogen-doped ordered mesoporous graphitic arrays with high electrocatalytic activity for oxygen reduction. *Angew. Chem.* **2010,** *122* (14), 2619-2623.
158. Paraknowitsch, J. P.; Zhang, J.; Su, D.; Thomas, A.; Antonietti, M., Ionic liquids as precursors for nitrogen-doped graphitic carbon. *Adv. Mater.* **2010,** *22* (1), 87-92.

159. Thomas, A.; Fischer, A.; Goettmann, F.; Antonietti, M.; Müller, J.-O.; Schlögl, R.; Carlsson, J. M., Graphitic carbon nitride materials: variation of structure and morphology and their use as metal-free catalysts. *J. Mater. Chem.* **2008,** *18* (41), 4893-4908.
160. Wang, X.; Maeda, K.; Thomas, A.; Takanabe, K.; Xin, G.; Carlsson, J. M.; Domen, K.; Antonietti, M., A metal-free polymeric photocatalyst for hydrogen production from water under visible light. *Nat. Mater.* **2009,** *8* (1), 76-80.
161. Sidik, R. A.; Anderson, A. B.; Subramanian, N. P.; Kumaraguru, S. P.; Popov, B. N., O2 reduction on graphite and nitrogen-doped graphite: experiment and theory. *J. Phys. Chem. B* **2006,** *110* (4), 1787-1793.
162. Lota, G.; Grzyb, B.; Machnikowska, H.; Machnikowski, J.; Frackowiak, E., Effect of nitrogen in carbon electrode on the supercapacitor performance. *Chem. Phys. Lett.* **2005,** *404* (1-3), 53-58.
163. Paraknowitsch, J. P.; Thomas, A., Doping carbons beyond nitrogen: an overview of advanced heteroatom doped carbons with boron, sulphur and phosphorus for energy applications. *Energy Environ. Sci.* **2013,** *6* (10), 2839-2855.
164. Boehm, H. P.; Mair, G.; Stoehr, T.; De Rincón, A. R.; Tereczki, B., Carbon as a catalyst in oxidation reactions and hydrogen halide elimination reactions. *Fuel* **1984,** *63* (8), 1061-1063.
165. Stöhr, B.; Boehm, H.; Schlögl, R., Enhancement of the catalytic activity of activated carbons in oxidation reactions by thermal treatment with ammonia or hydrogen cyanide and observation of a superoxide species as a possible intermediate. *Carbon* **1991,** *29* (6), 707-720.
166. Pietrzak, R.; Jurewicz, K.; Nowicki, P.; Babeł, K.; Wachowska, H., Nitrogen-enriched bituminous coal-based active carbons as materials for supercapacitors. *Fuel* **2010,** *89* (11), 3457-3467.
167. Pietrzak, R.; Wachowska, H.; Nowicki, P., Preparation of nitrogen-enriched activated carbons from brown coal. *Energy fuels* **2006,** *20* (3), 1275-1280.
168. Nowicki, P.; Pietrzak, R.; Wachowska, H., Influence of the precursor metamorphism degree on preparation of nitrogen-enriched activated carbons by ammoxidation and chemical activation of coals. *Energy Fuels* **2009,** *23* (4), 2205-2212.
169. Yang, C.-M.; Weidenthaler, C.; Spliethoff, B.; Mayanna, M.; Schüth, F., Facile template synthesis of ordered mesoporous carbon with polypyrrole as carbon precursor. *Chem. Mater.* **2005,** *17* (2), 355-358.
170. Yang, Z.; Xia, Y.; Sun, X.; Mokaya, R., Preparation and hydrogen storage properties of zeolite-templated carbon materials nanocast via chemical vapor deposition: effect of the zeolite template and nitrogen doping. *J. Phys. Chem. B* **2006,** *110* (37), 18424-18431.
171. Shen, W.; Fan, W., Nitrogen-containing porous carbons: synthesis and application. *J. Mater. Chem. A* **2013,** *1* (4), 999-1013.
172. Xia, Y.; Mokaya, R., Generalized and facile synthesis approach to N-doped highly graphitic mesoporous carbon materials. *Chem. Mater.* **2005,** *17* (6), 1553-1560.
173. Shen, W.; Zhang, S.; He, Y.; Li, J.; Fan, W., Hierarchical porous polyacrylonitrile-based activated carbon fibers for CO 2 capture. *J. Mater. Chem.* **2011,** *21* (36), 14036-14040.
174. Castro-Muñiz, A.; Suárez-García, F.; Martínez-Alonso, A.; Tascón, J. M., Activated carbon fibers with a high content of surface functional groups by phosphoric acid activation of PPTA. *J. Colloid Interface Sci.* **2011,** *361* (1), 307-315.
175. Antonietti, M.; Oschatz, M., The Concept of "Noble, Heteroatom-Doped Carbons," Their Directed Synthesis by Electronic Band Control of Carbonization, and Applications in Catalysis and Energy Materials. *Adv. Mater.* **2018,** *30* (21), 1706836.
176. Fukuzumi, S.; Ohkubo, K., Organic synthetic transformations using organic dyes as photoredox catalysts. *Org. Biomol. Chem.* **2014,** *12* (32), 6059-6071.
177. Lee, Y.; Lee, H.; Park, S.; Yi, Y., Energy level alignment at the interfaces between typical electrodes and nucleobases: Al/adenine/indium-tin-oxide and Al/thymine/indium-tin-oxide. *Appl. Phys. Lett.* **2012,** *101* (23), 233305.
178. Kazemiabnavi, S.; Zhang, Z.; Thornton, K.; Banerjee, S., Electrochemical stability window of imidazolium-based ionic liquids as electrolytes for lithium batteries. *J. Phys. Chem. B* **2016,** *120* (25), 5691-5702.

179. Zhang, J.; Sun, J.; Maeda, K.; Domen, K.; Liu, P.; Antonietti, M.; Fu, X.; Wang, X., Sulfur-mediated synthesis of carbon nitride: band-gap engineering and improved functions for photocatalysis. *Energy Environ. Sci.* **2011,** *4* (3), 675-678.
180. Lin, L.; Ou, H.; Zhang, Y.; Wang, X., Tri-s-triazine-based crystalline graphitic carbon nitrides for highly efficient hydrogen evolution photocatalysis. *ACS Catal.* **2016,** *6* (6), 3921-3931.
181. Zhang, S.; Tsuzuki, S.; Ueno, K.; Dokko, K.; Watanabe, M., Upper limit of nitrogen content in carbon materials. *Angew. Chem., Int. Ed.* **2015,** *54* (4), 1302-1306.
182. Li, J.-R.; Kuppler, R. J.; Zhou, H.-C., Selective gas adsorption and separation in metal–organic frameworks. *Chem. Soc. Rev.* **2009,** *38* (5), 1477-1504.
183. Dąbrowski, A., Adsorption—from theory to practice. *Adv. Colloid Interface Sci.* **2001,** *93* (1-3), 135-224.
184. Ustinov, E. A.; Klyuev, L. E., Adsorption equilibrium of binary mixtures in zeolites and state of adsorbed phase. *Adsorption* **1999,** *5* (4), 331-343.
185. Rouf, S. A.; Eić, M., Adsorption of SO 2 from wet mixtures on hydrophobic zeolites. *Adsorption* **1998,** *4* (1), 25-33.
186. An, J.; Rosi, N. L., Tuning MOF CO2 adsorption properties via cation exchange. *J. Am. Chem. Soc.* **2010,** *132* (16), 5578-5579.
187. Mulloth, L. M.; Finn, J. E., *Carbon dioxide adsorption on a 5A zeolite designed for CO2 removal in spacecraft cabins*. National Aeronautics and Space Administration, Ames Research Center: 1998.
188. Hernández-Huesca, R.; Díaz, L.; Aguilar-Armenta, G., Adsorption equilibria and kinetics of CO2, CH4 and N2 in natural zeolites. *Sep. Purif. Technol.* **1999,** *15* (2), 163-173.
189. Sherman, J. D., Synthetic zeolites and other microporous oxide molecular sieves. *Proc. Natl. Acad. Sci. U.S.A.* **1999,** *96* (7), 3471-3478.
190. Yong, Z.; Mata, V.; Rodrigues, A. r. E., Adsorption of carbon dioxide at high temperature—a review. *Sep. Purif. Technol.* **2002,** *26* (2-3), 195-205.
191. Konduru, N.; Lindner, P.; Assaf-Anid, N. M., Curbing the greenhouse effect by carbon dioxide adsorption with zeolite 13X. *AIChE J.* **2007,** *53* (12), 3137-3143.
192. Li, G.; Xiao, P.; Webley, P. A.; Zhang, J.; Singh, R., Competition of CO2/H2O in adsorption based CO2 capture. *Energy Procedia* **2009,** *1* (1), 1123-1130.
193. Sumida, K.; Rogow, D. L.; Mason, J. A.; McDonald, T. M.; Bloch, E. D.; Herm, Z. R.; Bae, T.-H.; Long, J. R., Carbon dioxide capture in metal–organic frameworks. *Chem. Rev.* **2012,** *112* (2), 724-781.
194. Rowsell, J. L.; Yaghi, O. M., Metal–organic frameworks: a new class of porous materials. *Microporous Mesoporous Mat.* **2004,** *73* (1-2), 3-14.
195. Yaghi, O. M.; O'Keeffe, M.; Ockwig, N. W.; Chae, H. K.; Eddaoudi, M.; Kim, J., Reticular synthesis and the design of new materials. *Nature* **2003,** *423* (6941), 705-714.
196. Férey, G.; Mellot-Draznieks, C.; Serre, C.; Millange, F.; Dutour, J.; Surblé, S.; Margiolaki, I., A chromium terephthalate-based solid with unusually large pore volumes and surface area. *Science* **2005,** *309* (5743), 2040-2042.
197. Mueller, U.; Schubert, M.; Teich, F.; Puetter, H.; Schierle-Arndt, K.; Pastre, J., Metal–organic frameworks—prospective industrial applications. *J. Mater. Chem.* **2006,** *16* (7), 626-636.
198. Duan, J.; Jin, W.; Kitagawa, S., Water-resistant porous coordination polymers for gas separation. *Coord. Chem. Rev.* **2017,** *332*, 48-74.
199. Sevilla, M.; Fuertes, A. B., Sustainable porous carbons with a superior performance for CO 2 capture. *Energy & Environmental Science* **2011,** *4* (5), 1765-1771.
200. Patel, H. A.; Byun, J.; Yavuz, C. T., Carbon dioxide capture adsorbents: chemistry and methods. *ChemSusChem* **2017,** *10* (7), 1303-1317.
201. Zhao, Y.; Liu, X.; Han, Y., Microporous carbonaceous adsorbents for CO 2 separation via selective adsorption. *RSC Advances* **2015,** *5* (38), 30310-30330.
202. Sevilla, M.; Valle-Vigón, P.; Fuertes, A. B., N-doped polypyrrole-based porous carbons for CO2 capture. *Adv. Funct. Mater.* **2011,** *21* (14), 2781-2787.

203. Gu, J.-M.; Kim, W.-S.; Hwang, Y.-K.; Huh, S., Template-free synthesis of N-doped porous carbons and their gas sorption properties. *Carbon* **2013,** *56*, 208-217.
204. To, J. W.; He, J.; Mei, J.; Haghpanah, R.; Chen, Z.; Kurosawa, T.; Chen, S.; Bae, W.-G.; Pan, L.; Tok, J. B.-H., Hierarchical N-doped carbon as CO2 adsorbent with high CO2 selectivity from rationally designed polypyrrole precursor. *J. Am. Chem. Soc.* **2016,** *138* (3), 1001-1009.
205. Liu, L.; Tan, S. J.; Horikawa, T.; Do, D.; Nicholson, D.; Liu, J., Water adsorption on carbon-A review. *Adv. Colloid Interface Sci.* **2017,** *250*, 64-78.
206. Wang, J.; Heerwig, A.; Lohe, M. R.; Oschatz, M.; Borchardt, L.; Kaskel, S., Fungi-based porous carbons for CO 2 adsorption and separation. *J. Mater. Chem.* **2012,** *22* (28), 13911-13913.
207. Presser, V.; McDonough, J.; Yeon, S.-H.; Gogotsi, Y., Effect of pore size on carbon dioxide sorption by carbide derived carbon. *Energy Environ. Sci.* **2011,** *4* (8), 3059-3066.
208. Oschatz, M.; Leistner, M.; Nickel, W.; Kaskel, S., Advanced structural analysis of nanoporous materials by thermal response measurements. *Langmuir* **2015,** *31* (13), 4040-4047.
209. Gongadze, E.; Velikonja, A.; Slivnik, T.; Kralj-Iglič, V.; Iglič, A., The quadrupole moment of water molecules and the permittivity of water near a charged surface. *Electrochim. Acta* **2013,** *109*, 656-662.
210. Pérez-Ramírez, J.; Christensen, C. H.; Egeblad, K.; Christensen, C. H.; Groen, J. C., Hierarchical zeolites: enhanced utilisation of microporous crystals in catalysis by advances in materials design. *Chem. Soc. Rev.* **2008,** *37* (11), 2530-2542.
211. Salanne, M.; Rotenberg, B.; Naoi, K.; Kaneko, K.; Taberna, P.-L.; Grey, C. P.; Dunn, B.; Simon, P., Efficient storage mechanisms for building better supercapacitors. *Nature Energy* **2016,** *1* (6), 1-10.
212. Luo, X.-y.; Chen, Y.; Mo, Y., A review of charge storage in porous carbon-based supercapacitors. *New Carbon Mater.* **2021,** *36* (1), 49-68.
213. Gamby, J.; Taberna, P.; Simon, P.; Fauvarque, J.; Chesneau, M., Studies and characterisations of various activated carbons used for carbon/carbon supercapacitors. *J. Power Sources* **2001,** *101* (1), 109-116.
214. Chmiola, J.; Largeot, C.; Taberna, P. L.; Simon, P.; Gogotsi, Y., Desolvation of ions in subnanometer pores and its effect on capacitance and double-layer theory. *Angew. Chem. Int. Ed.* **2008,** *47* (18), 3392-3395.
215. Prehal, C.; Koczwara, C.; Jäckel, N.; Schreiber, A.; Burian, M.; Amenitsch, H.; Hartmann, M. A.; Presser, V.; Paris, O., Quantification of ion confinement and desolvation in nanoporous carbon supercapacitors with modelling and in situ X-ray scattering. *Nature Energy* **2017,** *2* (3), 1-8.
216. Zhang, L. L.; Zhao, X.; Ji, H.; Stoller, M. D.; Lai, L.; Murali, S.; Mcdonnell, S.; Cleveger, B.; Wallace, R. M.; Ruoff, R. S., Nitrogen doping of graphene and its effect on quantum capacitance, and a new insight on the enhanced capacitance of N-doped carbon. *Energy Environ. Sci.* **2012,** *5* (11), 9618-9625.
217. Lin, L.; Xie, H.; Lei, Y.; Li, R.; Liu, X.; Ou, J., Nitrogen source-mediated cocoon silk-derived N, O-doped porous carbons for high performance symmetric supercapacitor. *J. Mater. Sci.: Mater. Electron.* **2020,** *31*, 10825-10835.
218. Bichat, M.; Raymundo-Piñero, E.; Béguin, F., High voltage supercapacitor built with seaweed carbons in neutral aqueous electrolyte. *Carbon* **2010,** *48* (15), 4351-4361.
219. Zhao, C.; Zheng, W., A review for aqueous electrochemical supercapacitors. *Front. Energy Res.* **2015,** *3*, 23.
220. Li, X.-r.; Jiang, Y.-h.; Wang, P.-z.; Mo, Y.; Li, Z.-j.; Yu, R.-j.; Du, Y.-t.; Zhang, X.-r.; Chen, Y., Effect of the oxygen functional groups of activated carbon on its electrochemical performance for supercapacitors. *New Carbon Materials* **2020,** *35* (3), 232-243.
221. Xia, Y.; Yang, Z.; Mokaya, R., Templated nanoscale porous carbons. *Nanoscale* **2010,** *2* (5), 639-659.
222. Inagaki, M.; Toyoda, M.; Soneda, Y.; Tsujimura, S.; Morishita, T., Templated mesoporous carbons: Synthesis and applications. *Carbon* **2016,** *107*, 448-473.

223. Lama, S. M.; Schmidt, J.; Malik, A.; Walczak, R.; Silva, D. V.; Völkel, A.; Oschatz, M., Modification of Salt-Templated Carbon Surface Chemistry for Efficient Oxidation of Glucose with Supported Gold Catalysts. *ChemCatChem* **2018,** *10* (11), 2458-2465.
224. Hwang, J.; Walczak, R.; Oschatz, M.; Tarakina, N. V.; Schmidt, B. V., Micro-Blooming: Hierarchically Porous Nitrogen-Doped Carbon Flowers Derived from Metal-Organic Mesocrystals. *Small* **2019,** *15* (37), 1901986.
225. Kuhn, P.; Antonietti, M.; Thomas, A., Porous, covalent triazine-based frameworks prepared by ionothermal synthesis. *Angew. Chem. Int. Ed.* **2008,** *47* (18), 3450-3453.
226. Jia, J.; Chen, Z.; Belmabkhout, Y.; Adil, K.; Bhatt, P. M.; Solovyeva, V. A.; Shekhah, O.; Eddaoudi, M., Carbonization of covalent triazine-based frameworks via ionic liquid induction. *J. Mater. Chem. A* **2018,** *6* (32), 15564-15568.
227. Yan, R.; Heil, T.; Presser, V.; Walczak, R.; Antonietti, M.; Oschatz, M., Ordered Mesoporous Carbons with High Micropore Content and Tunable Structure Prepared by Combined Hard and Salt Templating as Electrode Materials in Electric Double-Layer Capacitors. *Adv. Sustain. Syst.* **2018,** *2* (2), 1700128.
228. Fellinger, T. P.; Thomas, A.; Yuan, J.; Antonietti, M., 25th anniversary article:"cooking carbon with salt": carbon materials and carbonaceous frameworks from ionic liquids and poly (ionic liquid) s. *Adv. Mater.* **2013,** *25* (41), 5838-5855.
229. Oschatz, M.; Hofmann, J. P.; van Deelen, T. W.; Lamme, W. S.; Krans, N. A.; Hensen, E. J.; de Jong, K. P., Effects of the Functionalization of the Ordered Mesoporous Carbon Support Surface on Iron Catalysts for the Fischer–Tropsch Synthesis of Lower Olefins. *ChemCatChem* **2017,** *9* (4), 620-628.
230. Walczak, R.; Kurpil, B.; Savateev, A.; Heil, T.; Schmidt, J.; Qin, Q.; Antonietti, M.; Oschatz, M., Template-and metal-free synthesis of nitrogen-rich nanoporous "Noble" carbon materials by direct pyrolysis of a preorganized hexaazatriphenylene precursor. *Angew. Chem. Int. Ed.* **2018,** *57* (33), 10765-10770.
231. Tang, Z.; Pei, Z.; Wang, Z.; Li, H.; Zeng, J.; Ruan, Z.; Huang, Y.; Zhu, M.; Xue, Q.; Yu, J., Highly anisotropic, multichannel wood carbon with optimized heteroatom doping for supercapacitor and oxygen reduction reaction. *Carbon* **2018,** *130*, 532-543.
232. Xing, W.; Liu, C.; Zhou, Z.; Zhang, L.; Zhou, J.; Zhuo, S.; Yan, Z.; Gao, H.; Wang, G.; Qiao, S. Z., Superior CO 2 uptake of N-doped activated carbon through hydrogen-bonding interaction. *Energy Environ. Sci.* **2012,** *5* (6), 7323-7327.
233. Walczak, R.; Savateev, A.; Heske, J.; Tarakina, N. V.; Sahoo, S.; Epping, J. D.; Kühne, T. D.; Kurpil, B.; Antonietti, M.; Oschatz, M., Controlling the strength of interaction between carbon dioxide and nitrogen-rich carbon materials by molecular design. *Sustain. Energy Fuels* **2019,** *3* (10), 2819-2827.
234. Savateev, A.; Pronkin, S.; Epping, J. D.; Willinger, M. G.; Antonietti, M.; Dontsova, D., Synthesis of an electronically modified carbon nitride from a processable semiconductor, 3-amino-1, 2, 4-triazole oligomer, via a topotactic-like phase transition. *J. Mater. Chem. A* **2017,** *5* (18), 8394-8401.
235. Sundermeyer, W., Fused salts and their use as reaction media. *Angew. Chem. Int. Ed.* **1965,** *4* (3), 222-238.
236. Dupont, J., From molten salts to ionic liquids: a "nano" journey. *Accounts of chemical research* **2011,** *44* (11), 1223-1231.
237. Fechler, N.; Antonietti, M., Domino games: Controlling structure and patterns of carbon nanomaterials in 2D & 3D. *Nano Today* **2015,** *10* (5), 593-614.
238. Wang, W.; Wang, B.; Embrechts, H.; Damm, C.; Cadranel, A.; Strauß, V.; Distaso, M.; Hinterberger, V.; Guldi, D. M.; Peukert, W., Shedding light on the effective fluorophore structure of high fluorescence quantum yield carbon nanodots. *RSC advances* **2017,** *7* (40), 24771-24780.
239. Mahmood, J.; Lee, E. K.; Jung, M.; Shin, D.; Jeon, I.-Y.; Jung, S.-M.; Choi, H.-J.; Seo, J.-M.; Bae, S.-Y.; Sohn, S.-D., Nitrogenated holey two-dimensional structures. *Nat. Commun.* **2015,** *6*, 6486.
240. Pels, J.; Kapteijn, F.; Moulijn, J.; Zhu, Q.; Thomas, K., Evolution of nitrogen functionalities in carbonaceous materials during pyrolysis. *Carbon* **1995,** *33* (11), 1641-1653.

241. Maldonado, S.; Morin, S.; Stevenson, K. J., Structure, composition, and chemical reactivity of carbon nanotubes by selective nitrogen doping. *Carbon* **2006,** *44* (8), 1429-1437.
242. Osswald, S.; Chmiola, J.; Gogotsi, Y., Structural evolution of carbide-derived carbons upon vacuum annealing. *Carbon* **2012,** *50* (13), 4880-4886.
243. Oschatz, M.; Pré, P.; Dörfler, S.; Nickel, W.; Beaunier, P.; Rouzaud, J.-N.; Fischer, C.; Brunner, E.; Kaskel, S., Nanostructure characterization of carbide-derived carbons by morphological analysis of transmission electron microscopy images combined with physisorption and Raman spectroscopy. *Carbon* **2016,** *105*, 314-322.
244. Silvestre-Albero, J.; Silvestre-Albero, A.; Rodríguez-Reinoso, F.; Thommes, M., Physical characterization of activated carbons with narrow microporosity by nitrogen (77.4 K), carbon dioxide (273 K) and argon (87.3 K) adsorption in combination with immersion calorimetry. *Carbon* **2012,** *50* (9), 3128-3133.
245. Millward, A. R.; Yaghi, O. M., Metal− organic frameworks with exceptionally high capacity for storage of carbon dioxide at room temperature. *J. Am. Chem. Soc.* **2005,** *127* (51), 17998-17999.
246. D'Alessandro, D. M.; Smit, B.; Long, J. R., Carbon dioxide capture: prospects for new materials. *Angew. Chem. Int. Ed.* **2010,** *49* (35), 6058-6082.
247. Hao, G. P.; Mondin, G.; Zheng, Z.; Biemelt, T.; Klosz, S.; Schubel, R.; Eychmüller, A.; Kaskel, S., Unusual Ultra-Hydrophilic, Porous Carbon Cuboids for Atmospheric-Water Capture. *Angew. Chem. Int. Ed.* **2015,** *54* (6), 1941-1945.
248. Gong, J.; Antonietti, M.; Yuan, J., Poly (Ionic Liquid)-Derived Carbon with Site-Specific N-Doping and Biphasic Heterojunction for Enhanced CO2 Capture and Sensing. *Angew. Chem. Int. Ed.* **2017,** *56* (26), 7557-7563.
249. Valiev, R., Nanomaterial advantage. *Nature* **2002,** *419* (6910), 887-889.
250. Marambio-Jones, C.; Hoek, E. M., A review of the antibacterial effects of silver nanomaterials and potential implications for human health and the environment. *J. Nanoparticle Res.* **2010,** *12* (5), 1531-1551.
251. Santhosh, C.; Velmurugan, V.; Jacob, G.; Jeong, S. K.; Grace, A. N.; Bhatnagar, A., Role of nanomaterials in water treatment applications: a review. *Chem. Eng. J.* **2016,** *306*, 1116-1137.
252. Rodriguez-Reinoso, F., The role of carbon materials in heterogeneous catalysis. *Carbon* **1998,** *36* (3), 159-175.
253. White, R. J.; Antonietti, M.; Titirici, M.-M., Naturally inspired nitrogen doped porous carbon. *Journal of Materials Chemistry* **2009,** *19* (45), 8645-8650.
254. Su, D. S.; Zhang, J.; Frank, B.; Thomas, A.; Wang, X.; Paraknowitsch, J.; Schlögl, R., Metal-free heterogeneous catalysis for sustainable chemistry. *ChemSusChem* **2010,** *3* (2), 169-180.
255. Yu, D.; Nagelli, E.; Du, F.; Dai, L., Metal-free carbon nanomaterials become more active than metal catalysts and last longer. *J. Phys. Chem. Lett.* **2010,** *1* (14), 2165-2173.
256. Sevilla, M.; Fuertes, A. B., Direct synthesis of highly porous interconnected carbon nanosheets and their application as high-performance supercapacitors. *ACS nano* **2014,** *8* (5), 5069-5078.
257. Yu, L.; Brun, N.; Sakaushi, K.; Eckert, J.; Titirici, M. M., Hydrothermal nanocasting: Synthesis of hierarchically porous carbon monoliths and their application in lithium–sulfur batteries. *Carbon* **2013,** *61*, 245-253.
258. Jost, K.; Perez, C. R.; McDonough, J. K.; Presser, V.; Heon, M.; Dion, G.; Gogotsi, Y., Carbon coated textiles for flexible energy storage. *Energy Environ. Sci.* **2011,** *4* (12), 5060-5067.
259. Merlet, C.; Rotenberg, B.; Madden, P. A.; Taberna, P.-L.; Simon, P.; Gogotsi, Y.; Salanne, M., On the molecular origin of supercapacitance in nanoporous carbon electrodes. *Nat. Mater.* **2012,** *11* (4), 306-310.
260. Perovic, M.; Qin, Q.; Oschatz, M., From molecular precursors to nanoparticles—tailoring the adsorption properties of porous carbon materials by controlled chemical functionalization. *Adv. Funct. Mater.* **2020,** *30* (41), 1908371.
261. Zhang, S.; Tsuzuki, S.; Ueno, K.; Dokko, K.; Watanabe, M., Upper limit of nitrogen content in carbon materials. *Angew. Chem. Int. Ed.* **2015,** *54* (4), 1302-1306.

262. Reckmeier, C. J.; Schneider, J.; Xiong, Y.; Häusler, J.; Kasák, P.; Schnick, W.; Rogach, A. L., Aggregated molecular fluorophores in the ammonothermal synthesis of carbon dots. *Chem. Mater.* **2017,** *29* (24), 10352-10361.
263. Stagi, L.; Mura, S.; Malfatti, L.; Carbonaro, C. M.; Ricci, P. C.; Porcu, S.; Secci, F.; Innocenzi, P., Anomalous optical properties of citrazinic acid under extreme pH conditions. *ACS omega* **2020,** *5* (19), 10958-10964.
264. Kuhn, R.; Bauer, H.; Knackmuss, H. J., Struktur und Synthesen des Bakterienfarbstoffs Indigoidin. *Chem. Ber.* **1965,** *98* (7), 2139-2153.
265. Wade, L. G.; Simek, J. W., *Organic chemistry*. Glenview, IL : Pearson: 2017.
266. Kuhn, R.; Starr, M. P.; Kuhn, D. A.; Bauer, H.; Knackmuss, H.-J., Indigoidine and other bacterial pigments related to 3, 3′-bipyridyl. *Archiv für Mikrobiologie* **1965,** *51* (1), 71-84.
267. Day, P. A.; Villalba, M. S.; Herrero, O. M.; Arancibia, L. A.; Alvarez, H. M., Formation of indigoidine derived-pigments contributes to the adaptation of Vogesella sp. strain EB to cold aquatic iron-oxidizing environments. *Antonie van Leeuwenhoek* **2017,** *110* (3), 415-428.
268. Sarkar, S.; Dutta, S.; Ray, C.; Dutta, B.; Chowdhury, J.; Pal, T., A two-component hydrogelator from citrazinic acid and melamine: synthesis, intriguing role of reaction parameters and iodine adsorption study. *CrystEngComm* **2015,** *17* (42), 8119-8129.
269. Ambrozio, A. R.; Leyssale, J.-M.; Pellenq, R. J.-M.; de Souza, F. A.; Vignoles, G. L.; Scopel, W. L.; Freitas, J. C., 13C NMR Parameters of Disordered Carbons: Atomistic Simulations, DFT Calculations, and Experimental Results. *J. Phys. Chem. C* **2020,** *124* (23), 12784-12793.
270. Freitas, J.; Cunha, A.; Emmerich, F., *Chem. Phys. Carbon* **2012,** *CRC Press*, 102−187.
271. Fedoseeva, Y. V.; Okotrub, A.; Koroteev, V.; Borzdov, Y. M.; Palyanov, Y. N.; Shubin, Y. V.; Maksimovskiy, E.; Makarova, A.; Münchgesang, W.; Bulusheva, L., Graphitization of 13C enriched fine-grained graphitic material under high-pressure annealing. *Carbon* **2019,** *141*, 323-330.
272. Koroteev, V.; Münchgesang, W.; Shubin, Y. V.; Palyanov, Y. N.; Plyusnin, P.; Smirnov, D.; Kovalenko, K.; Bobnar, M.; Gumeniuk, R.; Brendler, E., Multiscale characterization of 13C-enriched fine-grained graphitic materials for chemical and electrochemical applications. *Carbon* **2017,** *124*, 161-169.
273. Grünberg, B.; Emmler, T.; Gedat, E.; Shenderovich, I.; Findenegg, G. H.; Limbach, H. H.; Buntkowsky, G., Hydrogen bonding of water confined in mesoporous silica MCM-41 and SBA-15 studied by 1H solid-state NMR. *Chemistry–A European Journal* **2004,** *10* (22), 5689-5696.
274. Hao, G.-P.; Li, W.-C.; Qian, D.; Wang, G.-H.; Zhang, W.-P.; Zhang, T.; Wang, A.-Q.; Schüth, F.; Bongard, H.-J.; Lu, A.-H., Structurally designed synthesis of mechanically stable poly (benzoxazine-co-resol)-based porous carbon monoliths and their application as high-performance CO2 capture sorbents. *J. Am. Chem. Soc.* **2011,** *133* (29), 11378-11388.
275. Yuan, B.; Wu, X.; Chen, Y.; Huang, J.; Luo, H.; Deng, S., Adsorption of CO2, CH4, and N2 on ordered mesoporous carbon: approach for greenhouse gases capture and biogas upgrading. *Environ. Sci. Technol.* **2013,** *47* (10), 5474-5480.
276. Eggenhuisen, T. M.; Prieto, G.; Talsma, H.; de Jong, K. P.; de Jongh, P. E., Entrance Size Analysis of Silica Materials with Cagelike Pore Structure by Thermoporometry. *J.Phys.Chem.C* **2012,** *116* (44), 23383-23393.
277. Morishige, K.; Yasunaga, H.; Matsutani, Y., Effect of pore shape on freezing and melting temperatures of water. *J. Phys. Chem. C.* **2010,** *114* (9), 4028-4035.
278. Morishige, K.; Yasunaga, H.; Denoyel, R.; Wernert, V., Pore-blocking-controlled freezing of water in cagelike pores of KIT-5. *The Journal of Physical Chemistry C* **2007,** *111* (26), 9488-9495.
279. Sarker, A. I.; Aroonwilas, A.; Veawab, A., Equilibrium and kinetic behaviour of CO2 adsorption onto zeolites, carbon molecular sieve and activated carbons. *Energy Procedia* **2017,** *114*, 2450-2459.
280. Wöllner, M.; Leistner, M.; Wollmann, P.; Benusch, M.; Klein, N.; Grählert, W.; Kaskel, S., Estimating pore size distributions of activated carbons via optical calorimetry. *Adsorption* **2017,** *23* (2), 313-320.

281. Song, G.; Zhu, X.; Chen, R.; Liao, Q.; Ding, Y.-D.; Chen, L., An investigation of CO2 adsorption kinetics on porous magnesium oxide. *Chem. Eng. J.* **2016,** *283*, 175-183.
282. Brunauer, S.; Emmett, P. H.; Teller, E., Adsorption of gases in multimolecular layers. *J. Am. Chem. Soc.* **1938,** *60* (2), 309-319.
283. Neimark, A. V.; Lin, Y.; Ravikovitch, P. I.; Thommes, M., Quenched solid density functional theory and pore size analysis of micro-mesoporous carbons. *Carbon* **2009,** *47* (7), 1617-1628.
284. Leistner, M.; Grählert, W.; Kaskel, S., Screening of porous materials by thermal response measurements. *Chem. Ing. Tech.* **2013,** *85* (5), 747-752.
285. Kurpil, B.; Savateev, A.; Papaefthimiou, V.; Zafeiratos, S.; Heil, T.; Özenler, S.; Dontsova, D.; Antonietti, M., Hexaazatriphenylene doped carbon nitrides—biomimetic photocatalyst with superior oxidation power. *Appl. Catal. B* **2017,** *217*, 622-628.

6. Appendix

6.1 List of abbreviations

Abbreviation	Full name
at.%	atomic percentage
BCP	Block copolymer
BET	Brunauer–Emmett–Teller
CCS	carbon capture and storage
CDCs	carbide-derived carbons
CMK	carbon mesostructured by KAIST
CV	Cyclic voltammetry
EDLC	electrochemical double-layer capacitors
EDX	Energy-dispersive X-ray spectroscopy
HAT-CN	Hexaazatriphenylene-hexacarbonitrile
HOMO	highest Occupied Molecular *Orbital*
IAST	ideal adsorption solution theory
IUPAC	International Union of Pure and Applied Chemistry
KIT	Korea Advanced Institute of Science and Technology, KAIST
LEDs	light-emitting diode
MEA	monoethanol amine
MOFs	Metal-organic frameworks
NPs	Nanoparticles
OMCs	ordered mesoporous carbons
ORR	oxygen reduction reaction
PCC	post combustion capture
PSA	pressure swing adsorption
PSD	Pore size distribution
PTFE	Polytetrafluoroethylene
QSDFT	Quenched solid density functional theory
Q_{st}	heat of adsorption
RHE	reference hydrogen electrode
SBA	Santa Barbara Amorphous type material
SEM	Scanning electron microscopy
SSA	Specific surface area
STC	Salt-templated carbon
TEM	Transmission electron microscopy
TGA	Thermogravimetric analysis
TSA	thermal swing adsorption
UPS	ultraviolet photoelectron spectroscopy
wt.%	weight percentage
XPS	X-ray photoelectron spectroscopy
XRD	X-ray diffraction

6.2 Characterization methods

Physisorption measurements

N_2/Ar physisorption: The information regarding the specific surface area (SSA), the total pore volume, and the pore size distribution of materials can be derived by nitrogen/argon physisorption measurements. The basic principle is to measure the adsorbed volume of the adsorbate such as N_2 or Ar relative to the mass of the adsorbent as a function of the relative pressure ($p\ p_0^{-1}$) of the adsorption where p_0 represents the saturation pressure of the adsorptive gas at a particular temperature. Every physisorption measurement is dependent on the temperature and the type of adsorbate. As the N_2 measurement is most often carried out at 77 K and at ambient pressure or below, weak van der Waals interactions between the gas and adsorbent are dominant. The adsorption isotherms can have different shapes based on the strength of the interactions. The pore size can be classified depending on the pore width of the materials into micropores, mesopores, and macropores according to the International Union of Pure and Applied Chemistry (IUPAC) that is also mentioned in **Chapter 2.2**.[68]

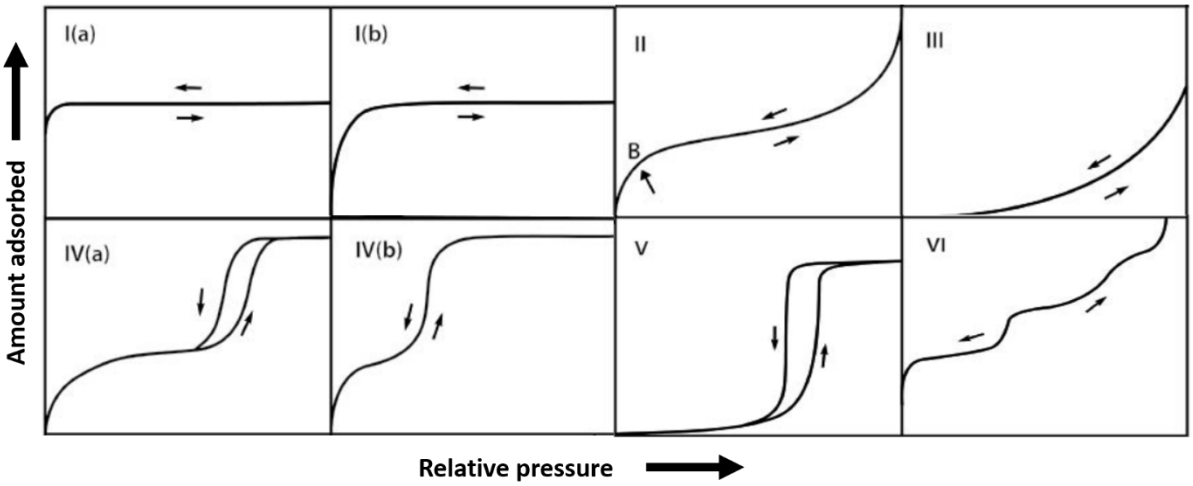

Figure 6.1 Classification of physisorption isotherms (adapted with permission from reference [68])

Figure 6.1 describes the different types of isotherms suggested by IUPAC. Microporous materials typically show the type I(a) and I(b) in which ultramicropores (0 – 0.7 nm) and supermicropores (0.7 – 2 nm) are filled with the adsorption gases that take place at relative pressure of $p\ p_0^{-1} < 0.01$ and $p\ p_0^{-1} = 0.01 – 0.15$, respectively.[68] Type II are shown when the materials are non-porous or contain solely macropores where monolayer-multilayer formation of the adsorptive gas takes place over the whole range of pressure and point B corresponds to the completion of the monolayer adsorption. In type III, the materials are non-porous or macroporous like for type II, but the interaction of adsorbate-adsorbate are more favorable so that adsorbate molecules form the clusters because of too weak interaction between adsorbate and adsorbent. When a material is mesoporous, isotherms of type IV are shown where a gas- liquid transition occurs due to their capillary condensation in the pores. Depending on the pore size, a hysteresis can be observed with the bigger mesopores that is described as type IV(a) while reversible isotherms of type IV(b) without any hysteresis are represented when narrower mesopores are present. By type V and type VI which are not common isotherms, a porous material but with weak interactions of adsorbent-adsorbate and a non-porous material with multilayer formed layer-by-layer adsorption are described, respectively.[68]

The BET (Brunauer, Emmett, and Teller) method is widely used to evaluate the specific surface area of materials as this model considers the possibility of multilayer adsorption on the surface of materials between adsorbate-adsorbate which takes place in a different adsorption enthalpy, and thus it is accurate and applicable for microporous or mesoporous materials.[282] The specific surface area can be calculated from the physisorption isotherms containing the total adsorbed volume (V_{ads}), the volume of a monolayer (V_{Mono}), and the adsorption constant (C) by using Equation (6.1).

$$\frac{p}{(p_0 - p) \times V_{ads}} = \frac{1}{C \times V_{Mono}} + \frac{C-1}{C \times V_{Mono}} \times \frac{1}{p} \tag{6.1}$$

$$SSA_{BET} = \frac{N_A \times V_{Mono} \times \sigma_{N_2}}{V_{mol} \times m_{Ads}} \tag{6.2}$$

$$\ln\frac{p}{p_0} = \frac{-2 \times \gamma \times V_m \times cos\varphi}{r \times R \times T} \tag{6.3}$$

Using the obtained V_{Mono} by Equation (6.1), the specific BET surface area (SSA_{BET}) are determined by Equation (6.2) where the Avogadro constant (N_A), the cross-section of a single N_2 molecule (σ_{N_2}; 0.162 nm^2), the ideal gas volume (V_{mol}), and the mass of the adsorbent (m_{Ads}) are included. Besides, the mesopore size can be analyzed by the Barrett-Joyner-Halenda (BJH) method based on the Kelvin equations as shown in Equation (6.3) (each sign represents the surface tension of fluid (γ), the ideal gas volume (V_m), the wetting angle (φ), the radius of the meniscus in the pore condensed liquid (r), the ideal gas constant (R), and the temperature (T)), where the correlation between the relative pressure at which pore condensation occurs and the radius of the meniscus of the condensed specimen. The model, however, only describes the cylindrical shape of pores bigger than 2.5 nm of pore width, and therefore density functional theory (DFT) models have been developed to improve the pore size analysis for the micro/mesopores structure. Quenched solid density functional theory (QSDFT) have been widely used especially to analyze porous carbon based materials with typically heterogeneous surface structure.[283]

***CO_2 physisorption**:* The analysis of pore structure by using N_2 or Ar has limitations because of their kinetic restrictions and possible diffusion problems at the cryogenic measurement temperature leading to time-consuming measurements. To overcome these disadvantages, CO_2 physisorption measurements at 273 K are applied. At this temperature, CO_2 has a high saturation

pressure around 26141 torr. That is, measuring up to ambient conditions (1 – 760 torr) corresponds to a low relative pressure ($p\ p_0^{-1} \sim 0.03$) where micropores size can be measured with fast kinetics. Meanwhile, as mentioned in Chapter 2.4.1, it should be noted that the CO_2 molecule has a relatively large quadrupole moment and forms certain interactions with polar materials (e.g., zeolites, MOFs, or heteroatom-doped carbon materials), so the pore structure analysis with this test gas can be complicated for such materials.

$$s_{CO_2/N_2} = \frac{X_{CO_2}}{X_{N_2}} \times \frac{Y_{N_2}}{Y_{CO_2}} \tag{6.4}$$

The adsorption selectivity of CO_2 over N_2 was determined based on the adsorption isotherms measured at 273 K and 298 K according to the ideal adsorption solution theory (IAST) method assuming a N_2/CO_2 ratio of 90/10 as shown in Equation (6.4), where X and Y represent the molar ratio of the adsorbed phase in materials and the molar ratio of the gas, respectively.

***H_2O (vapor) physisorption**:* H_2O has been recently attracted attention as a promising test gas because of not only its rather smaller kinetic diameter (0.265 nm) than CO_2 (0.33 nm), and thus the easier diffusion into narrow pores but also its higher dipole moment. Therefore it can provide information about the polarity of the adsorbents depending on the adsorption types and uptakes. Combining the adsorption result of N_2/Ar and H_2O, the information about the pore structure and the surface properties of the porous materials can be decoupled from each other. The hydrophilicity can be observed according to IUPAC classification. For example, hydrophobic micro/mesoporous materials show type V isotherm with a hysteresis while type I, II, or IV can be observed with the

porous materials containing polar functional groups on the surfaces revealing the rather higher adsorption uptake at lower relative pressure.

$$-Q_{st} = R \frac{\partial \ln(\frac{p}{p_0})}{\partial (\frac{1}{T})} \tag{6.5}$$

The isosteric heat of adsorption (Q_{st}) for the test gas (e.g., CO_2 and H_2O) can be determined by the Clausius-Clapeyron equation (Equation (6.5)) which demands two or more than two isotherms measured at different temperature, where each character means the adsorption heat (Q_{st}), the ideal gas constant (R; 8.3144 J mol^{-1} K^{-1}), the partial pressure of the adsorbate (p), the saturation pressure of the adsorbate (p_0), and the temperature (T).

All samples (40- 50 mg of sample weight for N_2, CO_2, and H_2O, and 10-20 mg of sample weight for Ar) were degassed at 150 ^oC for 20 h under vacuum. For N_2 physisorption measurements, a Quantachrome Autosorb IQ (Quantachrome Instruments) apparatus and a Quadrasorb apparatus (Quantachrome Instruments) were used while the Quantachrome Autosorb IQ was used for all Ar, CO_2, and H_2O measurements. The specific surface area (SSA) was calculated based on the multipoint Brunauer-Emmett-Teller model in the range of $p\ p_0^{-1}$= 0.05 - 0.15 for N_2 and $p\ p_0^{-1}$= 0.005 - 0.05 for Ar. The pore size distributions were calculated with QSDFT for Ar adsorbed on carbon with cylindrical/sphere pore shape (adsorption branch kernel) at 87 K, and with QSDFT for N_2 adsorbed on carbon with a slit/cylindrical pore shape (adsorption branch kernel) model at 77 K implemented into the ASiQwin 3.0 analysis software. Micropore volumes below 2 nm were determined from the cumulative pore volume at 2 nm from Ar/N_2 results. Water vapor physisorption was measured at 298 K, 303 K and 308 K while CO_2 measurement was carried out at 273 K and 298 K.

***InfraSORP technique for Thermal Response Measurement*:** The thermal response measurement by using InfraSORP is a useful technique for the fast measurement and analysis of porous materials. The technique is based on optical adsorption calorimetry and it consists of an infrared sensor which optically detects the temperature change of the materials during the adsorption/ desorption of a test gas. The intensity of the temperature change can be correlated to the amount of adsorbed molecules, the pore size of the adsorbents, and the heat capacity of the adsorbents. That is, the resulting curves reveal the information about the properties of the sample - not only the adsorption capacity but the adsorption kinetics.[208,284] Because the adsorption of test gas is usually exothermic which releases the heat while and the heat is adsorbed in an endothermic mechanism, a continuous gas supply during the adsorption process raises the temperature to a certain point, and vice versa. Considering each measuring condition corresponds to the physisorption measurement with a certain relative pressure and temperature, the resulting temperature change curves in InfraSORP varies depending on not only the pore size distribution, heat capacity, chemical composition, or surface properties of the adsorbents, but also the amount of gas molecules, the kinetics of adsorption of the adsorbate used as the test gas (e.g., CO_2, n-butane, and H_2O). Using n-butane as a test gas, for example, the saturation pressure of these gas is ~ 2.4 bar at 298 K and the corresponding relative pressure at 1 bar pressure of n-butane is $p\ p_0^{-1} = 0.4$ at. In this condition, only mono/multilayer adsorption takes place with the larger mesopores still not saturated and only the micropores filled with test gas.

Thermal response measurements were carried out by using an optical calorimeter (InfraSORP Technology by Fraunhofer/Rubotherm). For the adsorption and desorption cycling measurements for CO_2 physisorption at 298 K, the materials (~ 10 mg) degassed in advance were placed in the sample cell, followed by purging with N_2 gas (70 – 80 ml min^{-1}, 1 bar) until the temperature stabilized. Then, the sample was subjected to the test gas (i.e., CO_2 and n-butane) for 100 – 200 s

(70 – 80 ml min^{-1}, 1 bar). Subsequently, a N_2 gas flow was subjected to the sample for the duration of ~ 200 s, resulting in the decrease of temperature due to desorption of test gas. For the measurement of H_2O (wet N_2) as a test gas, it was subjected for ~ 3000 s, followed by ~2000 s of desorption gas flow with N_2. The total uptake of samples was obtained from the integrated peak area (A) of the thermal response curve. This area was divided with the sample mass or total pore volume from N_2/Ar physisorption to compare the normalized uptake of the materials.

X-ray Phtoelectron Spectroscopy (XPS): XPS is a characterization technique to quantitatively identify the elements covering the surface of a material. By XPS, the chemical state of the elements as well as the electronic states and its density can be figured out. The basic physics of XPS is using the energy of X-ray at a certain wavelength which is already known (E_{photon} = 1486.7 eV for Al K_α X-ray). According to the photoelectric effect (Equation (6.6), where $E_{binding}$, E_{photon}, and $E_{kinetic}$, and ϕ mean the binding energy of the electron relative to the chemical potential, the energy from the X-ray photons, the kinetic energy of the electron by the instrument, and the work function for the surface of the materials, respectively), the binding energy of the each of the emitted electron can be determined when the kinetic energy of the emitted electron is measured.

$$E_{binding} = E_{photon} - (E_{kinetic} + \phi) \tag{6.6}$$

X-ray photoelectron spectroscopy (XPS) was performed on a Thermo Scientific K-Alpha spectrometer equipped with monochromatic Al K_α anode (hυ = 1486.6 eV) operating at 72 W. Elemental compositions were determined using survey recorded with a step size of 1.0 eV and a pass energy of 200 eV. The background pressure of the ultra-high vacuum (UHV) chamber was $< 2 \cdot 10^{-8}$ mbar. Quantitative characterization of the presence of carbon, nitrogen, and oxygen was accomplished with high-resolution regional XPS scans with a step size of 0.1 eV and a pass energy of 50 eV. Samples were handled in air without further precautions and mounted on conductive

carbon tape. Binding energies are reported as measured without further calibration. The measurement in Chapter 3.1 was performed by Prof. Dr. Jan P. Hofmann in the Eindhoven University of Technology, the Netherlands.

Elemental Analysis (EA): By combusting a material, the quantified composition of the elements can be analyzed especially for the elements C, N, H, and S. With the exposure of a flow of oxygen at ~ 1000 ºC, the combustion products such as CO_2, N_2, SO_2, and H_2O are generated, and thus the accurate contents of elements can be detected from the individual contents of these gases.

EA for C, H, N, S was performed by using a Vario Micro device. This analysis was carried out by Antje Völkel.

Thermogravimetric Analysis (TGA): TGA is a method to observe the mass of a material over time during a temperature change under a certain atmosphere. This measurement can for instance provide quantitative information about adsorption/desorption processes, phase transitions, and thermal decomposition.

TGA measurements were carried out under air flow using TG 209 F1 Libra (Netzsch, Germany) at a heating rate of 10 °C min^{-1} from room temperature to 1000 °C. This analysis was carried out by Antje Völkel.

Differential Scanning Calorimetry (DSC): As a thermoanalytical technique, DSC measures the amount of heat released or absorbed by a sample relative to a reference as a function of temperature. A well-defined heat capacity is demanded for the reference sample. The more or less heat flow of the sample than the reference is observed when the physical transformation of phase transitions occurs in that sample so that the heat change can be determined by DSC. DSC is classified into

the *heat-flux DSC* where the difference of the sample and the reference is measured during heat flux, and the *power differential DSC* during the power supplied to the sample and reference.

DSC measurements have been performed with a Differential Scanning Calorimeter, NETZSCH DSC 204 (Netzsch, Selb, Germany). An aluminum pan with a pierced lid was used for the measurement of 10 (±1) mg of the sample with a heating/cooling rate of 2.5 K/min in range between from - 60°C to 20°C /60°C at 5000µV. This analysis was carried out by Antje Völkel.

Scanning Electron Microscope/High-Resolution Transmission Electron Microscopy (SEM/ HRTEM)*:* SEM and HRTEM both use the electrons from an electron beam which interact with the sample. That is, the electrons generated from an electron gun are accelerated by an electromagnetic field followed by directing to the sample by the electromagnetic lenses so that the morphology and topography of the samples can be analyzed. In SEM, the secondary and backscattered electrons from the samples after the incident beam scanned over the specimen and interacted with the specimen are detected. In general, secondary electrons are widely used for SEM while backscattered electrons are applied for revealing the contrast in the composition of the sample. As secondary electrons are sensitive to the surface, the brightness difference depending on the angles of the incident electron beam is changed, and thus the topography can be observed. Meanwhile, because the backscattered electrons emitted from deeper region have rather higher energy, the heavier atom which contains high amount of backscattered electrons provides the brighter image than the lighter ones. The composition of the elements of a sample can be qualitatively and quantitatively identified by Energy Dispersive X-ray (EDX) spectroscopy where the electron vacancy of inner shell of the element in the sample caused by the striking of the incident electron beam is filled with the electrons from rather higher energy outer shell releasing

the energy of X-rays. By measuring those emitted energy from the sample, the elements of the sample can be quantified.

HRTEM is a powerful technique to analyze the properties of a sample on its atomic scale (e.g., crystal structure, elemental composition, or symmetry of the structure) by direct imaging of the atomic structure. The images are formed by the transmitted electrons through the thinned sample. In a bright field mode, commonly used for TEM, the area in which the electrons are transmitted becomes brighter while the region adsorbing or scattering electrons becomes dark so that the area with heavier elements appears as dark field and vice versa. Meanwhile, in the dark field mode, an inversed image appears where the scattered electrons are used to provide the diffraction patterns showing the brighter images. It gives the information for the crystallographic phases and the resolution can be determined by the acceleration voltage resulting in a higher resolution by using a higher voltage.

A LEO 1550-Gemini microscope operating at 3.00 kV was used for SEM measurements while EDX investigation was performed on a Link ISIS-300 system (Oxford Microanalysis Group) equipped with a Si(Li) detector and an energy resolution of 133 eV. The measurements were carried out by Heike Runge.

JEOL ARM 200F was used for HRTEM measurement. The investigations in **Chapter 3.1** and **3.2** were conducted using double-cs-correction, equipped with a cold field emission gun at 80kV of the acceleration voltage and 10µA of the emission, and a condenser aperture with a diameter of 150µm. The measurements were carried out by Bolortuya Badamdorj (**Chapter 3.1** and **3.2**) and Dr. Nadja Tarakina (**Chapter 3.3**).

Solid-state Nuclear magnetic resonance (ss NMR): The resonance frequency of nuclear spins is affected by the magnetic field. In solid state media with only little mobility (e.g., glasses or

crystalline powders), anisotropic interactions significantly influence the movement of the nuclear spins which are observed in the spectrum while a series spectra of sharp and intense peaks are observed in solution NMR due to the averaging of anisotropic interactions to zero so that it is not reflected in NMR spectra. The presence of the broad peaks rather provides the structure and dynamics of the solid state by analyzing the internuclear distances, probing the symmetry, and deconvolution of quadrupolar/dipolar influenced spectra.

The structural investigation of ^{13}C CPMAS NMR as well ^{1}H MAS NMR spectroscopy was carried out on a Bruker Avance III NMR magnetic field at a magnetic strength of 7 T. The spectrometer equipment with a 4 mm probe head allowed achieving the spinning frequency of 10 kHz. For the collection of 1H $\rightarrow$ ^{13}C CPMAS data the ^{1}H 90°-pulse with a duration of 2.3 µs was set. The flipped ^{1}H (spin) magnetization was locked applying the power of 60 W. The ^{13}C and ^{1}H spins were matched under the Hartmann-Hahn conditions during the contact time of 3 ms and requiring the pulse power of 200 W in the ^{13}C channel. For the ^{1}H spin decoupling the spinal 64_13 applying 40 W was used. The repetition time between the recorded 12 670 scans (ca. 18 h) amounted 5 s. To study the structural environment of protons the background suppression pulse sequence was chosen with appropriate pulse lengths of 2.3 µs and 4.6 µs. The delay time between the 90° and 180°-pulse was 2 µs, whereby the pulses were emitted using a repetition time of 5 s. For a taking of every ^{1}H spectrum 36 scans (3 min.) were accumulated. This analysis was carried out by Edina Šić and Dr. Torsten Gutmann in Eduard-Zintl Institut for Inorganic and Physical Chemistry.

Raman Spectroscopy: A structural fingerprint typically through vibrational modes of molecules can be identified by using Raman spectroscopy. Inelastic scattering of photons which is known as Raman scattering is the main principle of this technique. When a monochromatic light source such as visible, near infrared, or near ultraviolet laser interacts with the vibrations of the molecules,

phonons or other excited parts result in the shifted energy of the laser photons. By analyzing the shift of energy, the information about the vibrational modes can be provided in the system.

Raman spectra were obtained by using a Witec Raman microscope operating with an objective (Nikon, Japan, 10×/0.25, ∞/-WD 6.1), an excitation wavelength of 532 nm of green laser at the intensity of 1.0 mW. The measurements were performed by Jinyeon Hwang (**Chapter 3.1**) and Wuyong Zhang (**Chapter 3.2**).

Fourier-Transform Infrared Spectroscopy (FT-IR): An infrared spectrum of the absorption and emission in a sample of gas, liquid, or solid can be obtained over a wide spectral range through FTIR which is caused by the stretching, vibration, or rotation of the chemical bonds in the molecules. That is, the amount of monochromatic light beam adsorbed by the sample for each different wavelength is measured. As the part of infrared radiation is absorbed or transmitted by the sample, the resulting spectra represent the fingerprint of the chemical composition of the sample. The raw data which contains the light absorption for each mirror position (that is used during measurement for each wavelength) requires a computer processing algorithm called the Fourier transformation to turn into the desired data of the absorbed light for each wavelength.

FTIR was performed on a Nicolet iS 5FTIR spectrometer (Thermo Fisher Scientific). The measurements were performed by Dr. Ivan Ilic.

X-Ray Diffraction (XRD): XRD is a powerful method to characterize the crystalline structure of the samples. The monochromatic X-ray beam with a certain wavelength generated from the target such as copper or molybdenum hits the sample, resulting in the deaccelerated and diffracted radiation of the X-ray diffraction pattern. The X-ray diffraction can be intuitively understood according to Bragg's law (Equation (6.7), where the symbols mean the any integer (n), the

wavelength of the beam (λ), the spacing between diffracting planes (d), and the incident angle (θ), respectively) where the constructive interference in few specific directions is determined when a regular array of scatterers (secondary spherical waves scattering from the electrons after striking the electrons) generates a regular array of wave in spherical shape. The investigation of the powder samples demands the scanning with a wide range of 2θ angles to lead to the diffraction in all directions possible.

$$n\lambda = 2d\sin\theta \tag{6.7}$$

Powder X-ray diffraction (XRD) patterns were obtained by using a Bruker D8 Advance diffractometer equipped with a scintillation counter detector (Cu K_α, $\lambda = 0.15184$ nm) applying in the 2θ range of 5° – 90° with a step size of 0.04° and counting time of 1s per step.

Inductively Coupled Plasma – Optical Emission Spectrometry (ICP-OES): ICP is a technique of optical emission spectrometry. The component elements are excited by the plasma energy injected from outside to analyze the sample. For the plasma generation, the high frequency of current is exposed to the torch coil in argon gas, and this argon gas is ionized so that the plasma is produced. Due to its high electron density and high temperature of 10,000 K, the excitation-emission of the sample is conducted by the energy of plasma. The excited atoms become to the lower energy emitting the spectrum rays corresponding to the photon wavelength. The contents of elements are determined by the position of the photons and its intensity.

The measurement was performed on an ICP-OES Optima 8000 von Perkin Elmer and for the calibration of an MES (multi elemental standard). It was carried out by Jessica Brandt.

Electrochemical Measurements for electric double-layer capacitors (EDLCs)

The electrodes for EDLCs were fabricated as follows: 45 mg of a sample and 5.5 ul of polytetrafluoroethylene (PTFE, 60 wt% solution) were mixed in 1 ml of ethanol. After transfer to a glass plate, it is mixed during drying with razor blades until a bean-like consistency is formed. By rolling the resulting material to a uniform thin sheet (thickness of 50 ± 10 μm), and then punching into 10 mm of diameter circle, freestanding electrode disks are obtained. All electrodes are used after drying at 60 °C overnight. In the Swagelok type cells, a pair of electrodes and a separator (Dreamweaver Silver, Dreamweaver International Inc.) of 13 mm in diameter form a sandwich-like assembly with a 70~80 ul of electrolyte (i.e., 1 M Na_2SO_4 aqueous solution or DI water) and a pair of Pt foils as current collectors. All electrochemical measurements have been carried out on a Biologic MPG-2 galvanostat/potentiostat at room temperature.

Electrochemical Impedance Spectroscopy (EIS): EIS measures the impedance of a measuring cell by changing a frequency range widely at the low amplitude of voltage. The resulting data is shown as a Nyquist plot containing the real and imaginary parts, representing a curve with a mixture of a semicircular shape and a straight line. The diameter of the semicircle and the slope of the straight line are determined by the surface conductivity of the interface in the system and the kinetics of the cell, respectively. The diameter of semicircle is inversely proportional with the conductivity while the larger slope represents a fast diffusion.

Cyclic Voltammetry (CV): CV, as a most common technique in electrochemical measurements, measures the resulting current as a response to the voltage change. By varying the scan rate, the information about the sample such as reversibility or Faradaic contribution to the whole capacity can be provided. The CV test was performed at a scan range of 0.1 – 500 mV s^{-1}. The differential gravimetric capacitance (C_d, [F g^{-1}]) and the integral gravimetric capacitance (C, [F g^{-1}]) from the

CV curves are calculated by the following Equation (6.8) and (6.9), where the symbols represent the current (I), the active mass in a carbon electrode (m), the scan rate in unit of V s^{-1} (γ).

$$\mathrm{C_d} = \frac{2 \times I}{m \times \gamma} \tag{6.8}$$

$$\mathrm{C} = \frac{\int_{V_1}^{V_2} I_+(V)dV - \int_{V_1}^{V_2} I_-(V)dV}{m \times \gamma \times (V_2 - V_2)} \tag{6.9}$$

Galvanostatic Charging/discharging with Potential Limitation (GCPL): By cycling under galvanostatic mode in a defined current, the voltage drop during discharge and thus the decreased capacitance can be obtained at an imposed current density. GCPL was measured at specific currents from 0.1 to 40 A g^{-1} within the cell voltage limitation ranges from −0.5 to +0.5 V. The gravimetric capacitances of carbon (C, [F g^{-1}]) were calculated according to the Equation (6.10) where Q_{dis} [C], V [V], V_{drop} [V], and m [g] mean the charge of the discharging cycle, the change of the discharging potential, the voltage drop at the discharge, and the active mass in a carbon electrode, respectively.

$$\mathrm{C} = \frac{2Q_{dis}}{(V - V_{drop})m} \tag{6.10}$$

6.3 Experimental process

Chemicals

Acetic acid, Acetonitrile (Sigma Aldrich), Ammonnium hydroxide solution, Citrazinic acid (Sigma Aldrich), Diaminomaleonitrile (Alfa Aesar), Hexaketocyclohexane octahydrate (Arcos Organics), Hydrochloric acid (Sigma Aldrich), Melamine (Sigma Aldrich), Nitric acid (Merck), Nitric acid, Potassium chloride (Sigma Aldrich), Sucrose (Sigma Aldrich), Sulfuric acid (Sigma Aldrich), Zinc chloride, polytetrafluoroethylene (PTFE, 60 wt% solution), Na_2SO_4 (Sigma Aldrich) were used without any further purification.

Synthetic procedures

Pre-condensation of citrazinic acid: 4 g of citrazinic acid (2,6-dihydroxy-4-pyridinecarboxylic acid, the condensation product of citric acid and ammonia) was placed on a crucible porcelain plate and annealed under air for 1 h at 350 °C. A yellowish solid was formed by the evaporated condensation products during the heat treatment with the typical appearance of carbon nitrides and a dark-brown or black oligomer was obtained in a yield of about 30 %. This resulting powder was well ground in a mortar.

Synthesis of nitrogen- and oxygen-lined carbons (NOC-X): $ZnCl_2$ was employed as the salt template for the synthesis of *NOC-Xs*. In a typical procedure, 12.44 g $ZnCl_2$ and 0.315 g melamine were physically well mixed with 1.24 g of the citrazinic acid condensate to form a dark grey colored powder. The mixture was then treated in a quartz flask with an electric heating mantle at 350 °C or 550 °C for 3 h. Resulting samples are named as *NOC-350 and NOC-550,* respectively. A portion of *NOC-550* was further condensed at higher temperatures ("X" = 750 °C and 950 °C), for 3 h under N_2 gas flow with 5 °C min^{-1} heating rate in a horizontal tubular furnace. Resulting

materials are named as *NOC-750 and NOC-950*, respectively. The remaining $ZnCl_2$ was removed with 1 M HCl aqueous solution overnight under vigorous stirring followed by filtration and washing with a large amount of deionized water. After the HCl-washing and filtering process has been carried out for two times, the resulting black powder was dried at 80 °C overnight under air. For the preparation of reference samples without pre-condensation, the same method was applied but 3.27 g of citrazinic acid were directly used as precursor.

Synthesis of nitrogen- and oxygen-lined carbons without salt as pore stabilizer (NOC-X-Y): NOC-X-Ys materials as a reference group have been prepared by the same method as *NOC-Xs* with the only difference that an additional heat treatment processes was applied after washing. That is, after the first heat treatment at a rather low temperature (X = 350 °C or 550 °C), salt was removed using the same washing process as described above for *NOC-X*. The additional heat treatment was performed under the same conditions as for *NOC-X* at a maximum temperature (Y = 550 °C, 750 °C, or 950 °C).

Synthesis of citrazinic acid and melamine based porous carbon (CMC-X): As the salt-template for CMC-Xs, the mixture of $ZnCl_2$ and KCl was employed. The salts (6.37 g of $ZnCl_2$ and 3.63 g of KCl) were dissolved in 10 ml of distilled water while 0.4 g of citrazinic acid was dissolved in 5 ml of ammonnium hydroxide solution (28 %) by ultra-sonication, giving a transparent and yellow solution, respectively. After mixing two solutions in the dish, it was dried overnight at 90 °C under air. The obtained deep blue material was well mixed and grinded with 0.13g of melamine. The heating ramp was set up as 1 h at 150 °C in heating mantle, and additional 3 h at 350, 550, 650 °C under argon gas (CMC-350, CMC-550, and CMC-650, respectively). For CMC-750 and CMC-1000, a portion of CMC-550 was further condensed at 750 °C and 1000°C, respectively, for 3 h under argon gas flow with 5 °C min^{-1} heating rate in a horizontal tubular furnace. 100 ml of 1 M

HCl aqueous solution was used to wash the remaining salts overnight and filtered. After the washing and filtering process were carried out two times, the result materials were dried overnight at 60 ℃ oven under air.

Synthesis of HAT-CNs: HAT-CN has been synthesized according to a recent report.[285] 4 g (12.6 mmol) of hexaketocyclohexane octahydrate and 10.88 g (100.8 mmol) of diaminomaleonitrile were refluxed in 150 ml of acetic acid for 2 h. Then the mixture was filtered and washed by using 25 ml of hot acetic acid several times. After the resulting black solid was suspended in 60 ml of 30 % nitric acid solution, it was heated up to 100 ℃ for 3 h and then was cooled down overnight in the ice water bath. The filtered solid was refluxed with 400 ml of acetonitrile for 2 h. After filtration and evaporation of residual solvent, an orange powder was produced.

Synthesis of C-HAT-Ts: C-HAT-Ts have been synthesized as reported before. 0.5 g of *HAT-CN* was carbonized at a temperature (T = 550 ℃ and 700 ℃) for 1 h under Ar gas flow with heating rates of 2 ℃ min^{-1} until 80 ℃ and 4℃ min^{-1} until 550 and 700, respectively in a quartz tube in a horizontal tubular furnace. *HAT-1000* in Chapter 3.2 is basically the same sample with C-HAT-Ts but only the condensation temperature is 1000 ℃.

Synthesis of Vac-HAT-Ts: Vac-HAT-Ts have been prepared at the same temperatures as *C-HAT-Ts* with the only difference that the quartz tube was constantly evacuated to a pressure of 34 mbar and no external gas was supplied. The heating rate was set to 10℃ min^{-1}.

6.4 Supporting tables and figures

Table S1. XPS data summary for atomic and weight percentage (rounded to two significant digits) of elements in the samples.

	C-content (at.%) (wt.%)	N-content (at.%) (wt.%)	O-content (at.%) (wt.%)	Zn-content (at.%) (wt.%)	Cl-content (at.%) (wt.%)	Others (at.%)	C/N (at. ratio)
NOC-350	58 (53)	29 (31)	11 (14)	0.1 (0.4)	0.9 (2.3)	-	2.0
NOC-550	74 (69)	20 (21)	6.0 (7.5)	-	0.6 (1.8)	0.1	3.8
NOC-750	78 (73)	15 (17)	5.0 (6.2)	0.2 (1.1)	0.9 (2.6)	-	5.1
NOC-950	87 (83)	5.1 (5.6)	6.3 (8.0)	0.1 (0.3)	0.7 (1.9)	0.5	17.1
NOC-350-550	74 (69)	20 (22)	6.4 (8.0)	0.2 (1.0)	0.1 (0.3)	-	3.7
NOC-550-750	82 (76)	13 (14)	3.7 (4.6)	0.8 (4.0)	0.5 (1.5)	-	6.2
NOC-550-950	93 (91)	4.6 (5.3)	2.8 (3.7)	0.1 (0.3)	-	-	20.1

Table S2. ^{13}C CPMAS NMR chemical shifts and signal width at half maximum of fitted peaks for primary materials (citrazinic acid, pre-CMC-X and melamine) as well for CMC-X materials condensed at different temperature.

Sample	Parameter	Fit 1	Fit 2	Fit 3	Fit 4	Fit 5	Fit 6
Citrazinic acid	δ_{iso} (ppm/TMS)	168.73	164.79	159.31	147.98	106.25	94.98
	fwhm (ppm)	6.00	3.32	5.36	4.95	7.02	7.19
pre-CMC-X	δ_{iso} (ppm/TMS)	192.68	172.07	164.11	150.76	100.23	46.4
	fwhm (ppm)	146.98	8.00	6.00	5.82	10.07	80.00
Melamine	δ_{iso} (ppm/TMS)	169.26	53.15	-	-	-	-
	fwhm (ppm)	9.02	96.72	-	-	-	-
CMC-350	δ_{iso} (ppm/TMS)	163.15	126.90	-	-	-	-
	fwhm (ppm)	13.95	83.05				
CMC-550	δ_{iso} (ppm/TMS)	157.87	120.80	35.94	-	-	-
	fwhm (ppm)	24.23	38.92	64.09			
CMC-650	δ_{iso} (ppm/TMS)	157.05	121.17	38.4	-	-	-
	fwhm (ppm)	32.83	30.00	97.39			
CMC-750	δ_{iso} (ppm/TMS)	153.57	127.77	30.7	-	-	-
	fwhm (ppm)	32.99	38.19	81.13			
CMC-1000	δ_{iso} (ppm/TMS)	129.93	26.91	16.10	-	-	-
	fwhm (ppm)	38.00	8.55	38.84	-	-	-

Table S3. Overview of estimated ^{1}H chemical shifts and signal widths regarding the dominating/most intensive signals for primary materials (citrazinic acid, pre-CMC-X and melamine) and condensed CMC-X materials at different temperature.

Sample	Parameter	Signal 1	Signal 2
Citrazinic acid	δ_{iso} (ppm/TMS)	13.33	6.39
	fwhm (ppm)	12.60	
pre-CMC-X	δ_{iso} (ppm/TMS)	6.48	3.05
	fwhm (ppm)	1.07	1.65
Melamine	δ_{iso} (ppm/TMS)	2.24	-
	fwhm (ppm)	16.91	-
CMC-350	δ_{iso} (ppm/TMS)	5.40	-
	fwhm (ppm)	12.06	-
CMC-550	δ_{iso} (ppm/TMS)	4.65	-
	fwhm (ppm)	5.60	-
CMC-650	δ_{iso} (ppm/TMS)	4.28	-
	fwhm (ppm)	2.88	-
CMC-750	δ_{iso} (ppm/TMS)	3.60	-
	fwhm (ppm)	0.96	-
CMC-1000	δ_{iso} (ppm/TMS)	0.62	-
	fwhm (ppm)	0.83	-

Table S4. Atomic percentage of the elements in CMC-Xs from EA and ICP-OES (rounded to a significant digit below the decimal point).

	C[at. %]	N[at. %]	H[at. %]	Zn[at. %]*	K[at. %]*	O[at.%]**	C/N atomic ratio
CMC-350	36.1	16.8	33.3	0.0	0.0	14.7	2.2
CMC-550	40.4	16.9	30.7	0.0	0.0	13.1	2.4
CMC-650	39.0	16.0	31.2	0.1	0.0	15.0	2.4
CMC-750	44.3	10.3	30.8	0.2	0.0	16.3	4.3
CMC-1000	59.6	3.5	22.5	0.0	0.0	17.4	17.1

* Calculated from ICP-OES measurement.

** Calculated by assuming oxygen as the remaining weight from integrated element weight of C, N, H, S (by EA), and Zn, K (by ICP-OES).

Table S5. N_2 physisorption at 77 K (specific surface area, pore volume), elemental analysis, and yield data of Vac-HAT-Ts at different condensation temperatures.

	SSA_{BET} [$m^2 g^{-1}$]	$V_{p/p0=0.95}$ [$cm^3 g^{-1}$]	N (wt.%)	C (wt.%)	C/N (wt.%)	Yield
Vac-HAT-200	-	-	40.2	53.7	1.3	97%
Vac-HAT-300	3.6	0.0058	39.8	53.9	1.4	97%
Vac-HAT-400	0.15	0.00027	40.0	54.1	1.4	93%
Vac-HAT-500	191	0.19	38.1	51.3	1.4	43%
Vac-HAT-550	720	0.5	32.4	46.4	1.4	9.2%
Vac-HAT-600	802	0.33	30.5	44.6	1.5	31%
Vac-HAT-700	809	0.35	26.6	49.0	1.8	30%

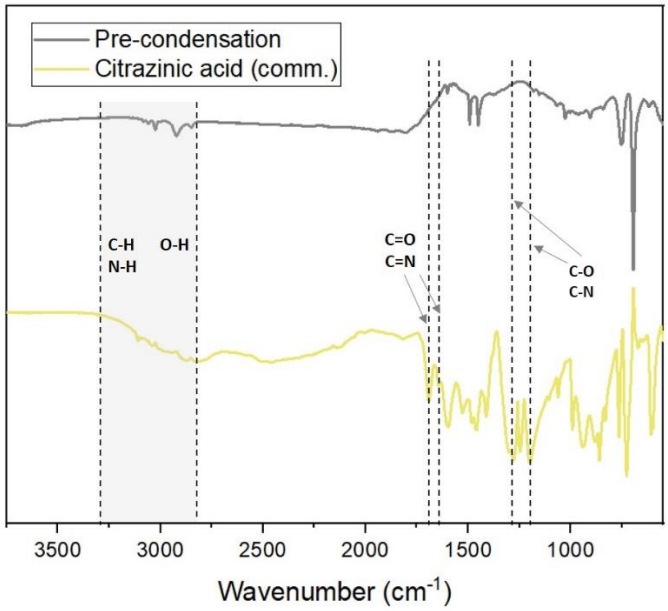

Figure S1. FT-IR spectra of commercial citrazinic acid and the product after pre-condensation.

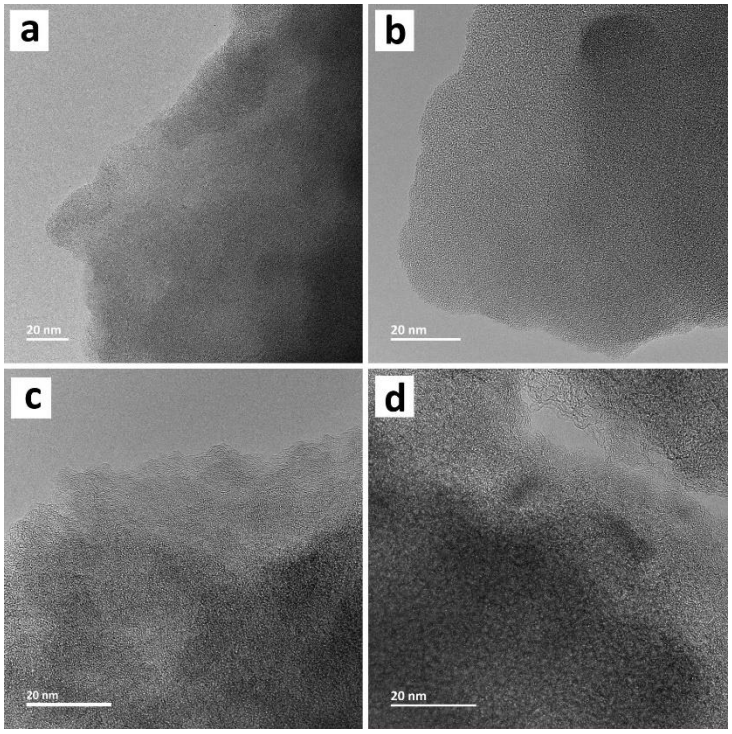

Figure S2. High-resolution transmission electron microscopy (HRTEM) images of (a) NOC-350, (b) NOC-550, (c) NOC-750, and (d) NOC-950.

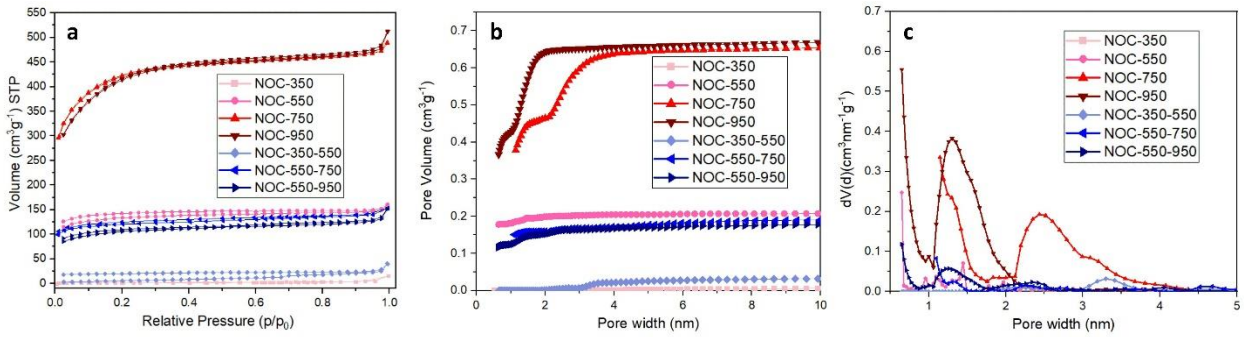

Figure S3. (a) N_2 physisorption isotherms (77 K), (b) corresponding cumulative pore volume distribution, and (c) differential pore size distribution calculated with QSDFT (N_2 on carbons with cylindrical/sphere pores at 77 K) of NOC-Xs and NOC-X-Ys.

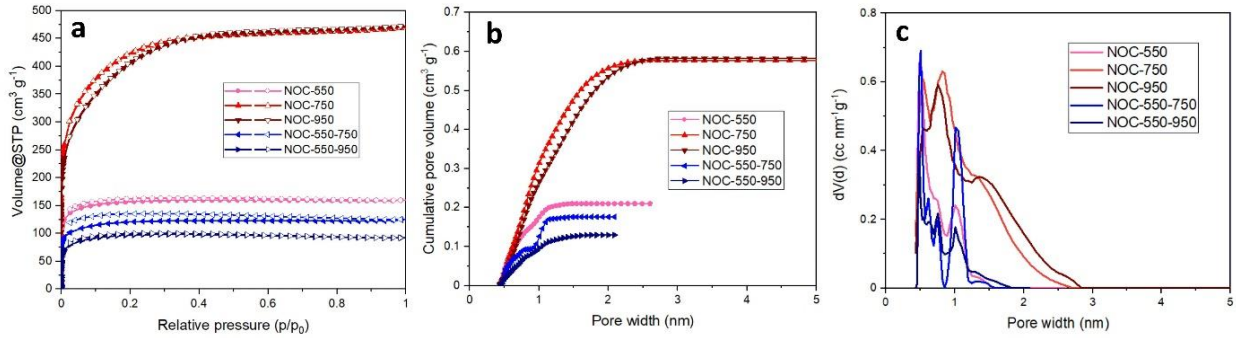

Figure S4. (a) Ar physisorption isotherms (87 K, filled and open symbols represent adsorption and desorption branches, respectively), (b) corresponding cumulative pore volume distribution, and (c) differential pore size distribution calculated with QSDFT equilibrium model (argon on carbons with slit pores at 87 K) of NOC-Xs and NOC-X-Ys.

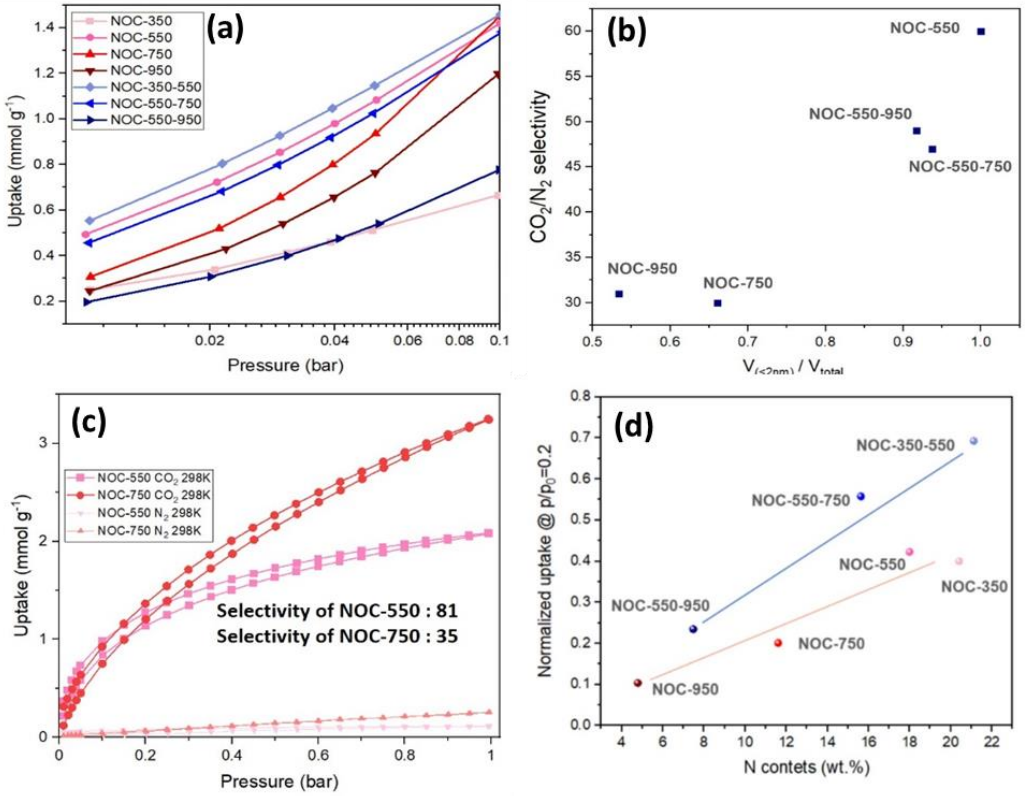

Figure S5. (a) Logarithmic plots of CO_2 isotherms (273 K) in the low pressure range, (b) relation between the CO_2/N_2 selectivity at 273 K and the ratio of micropore volume to total pore volume from Ar physisorption, (c) CO_2 and N_2 physisorption isotherms of NOC-550 and NOC-750 measured at 298 K, and (d) the normalized uptake at relative pressure $p/p_0 = 0.2$ as a function of the N content of NOC-Xs and NOC-X-Ys from EA.

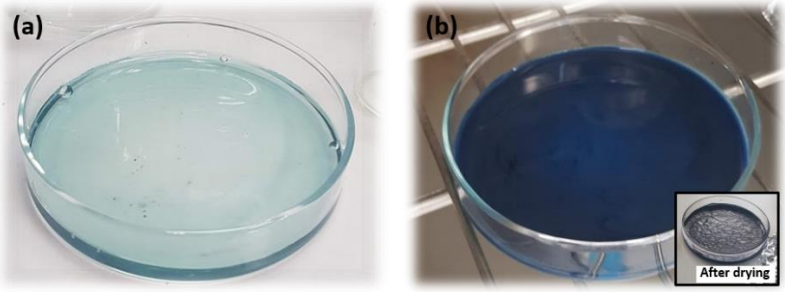

Figure S6. Photographs (a) after mixing the salts and citrazinic acid solutions and (b) after drying 1 h and after whole drying (inset).

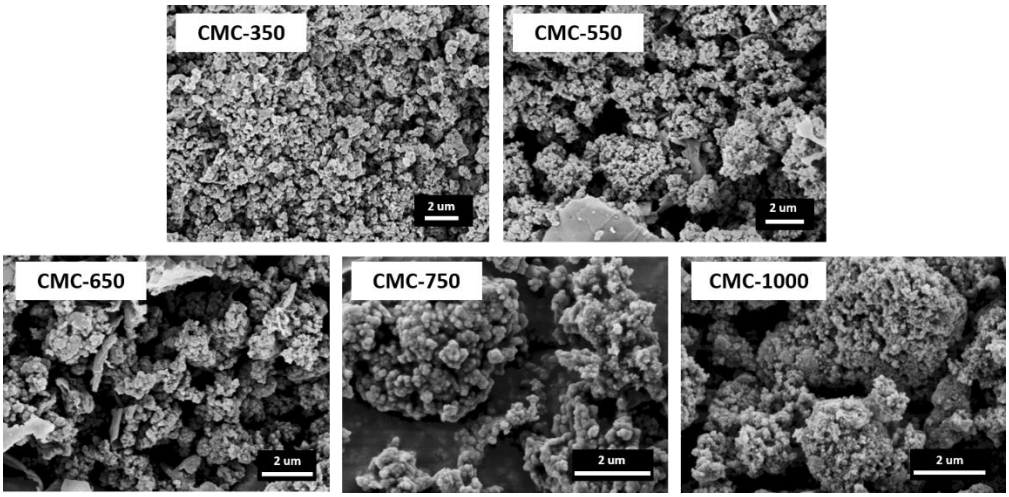

Figure S7. SEM images of CMC-Xs.

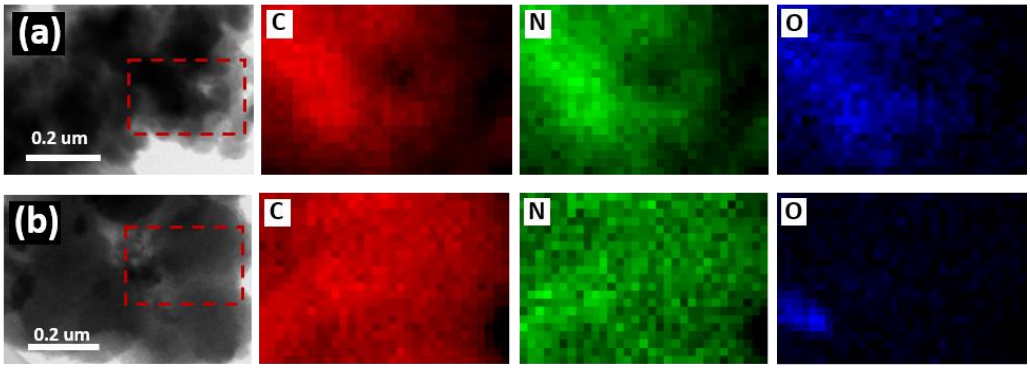

Figure S8. Elemental mapping of C (red), N (greed), and O (blue) of (a) CMC-550, and (b) CMC-750.

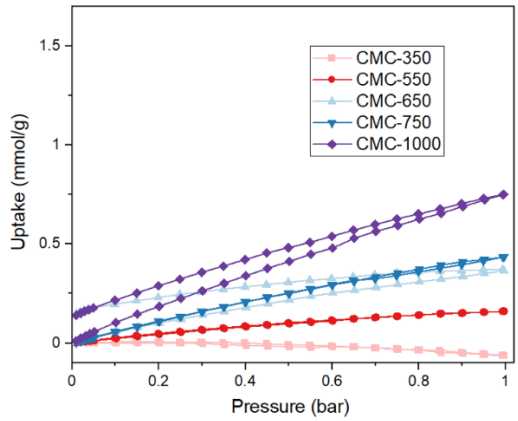

Figure S9. N_2 physisorption isotherms at 273 K of CMC-Xs.

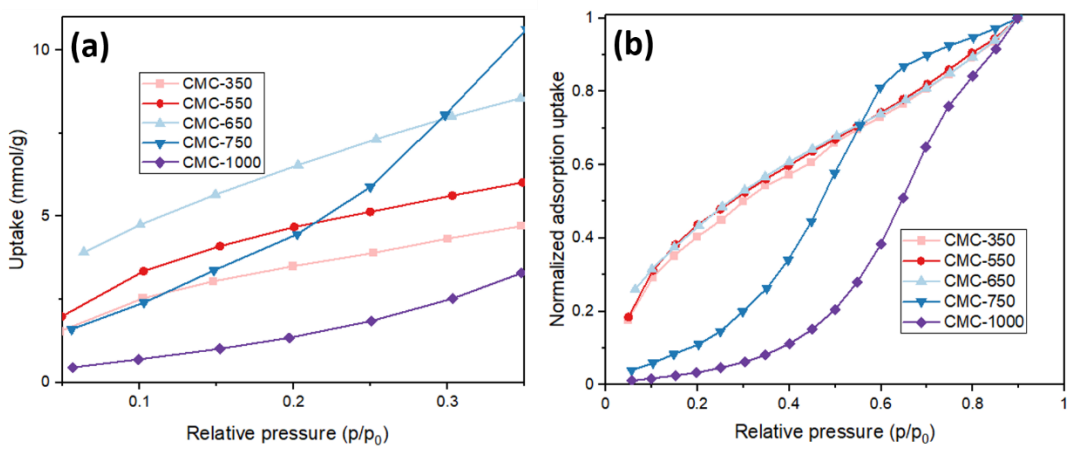

Figure S10. (a) H_2O physospriton isotherms magnified at low relative pressure region below and (b) normalized adsorption amount relative to the maximum H_2O uptake of CMC-Xs.

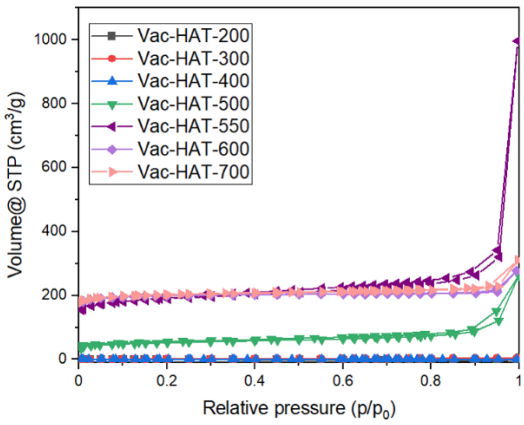

Figure S11. N_2 physisorption isotherms (77 K) of Vac-HAT-Ts obtained at different condensation temperatures.

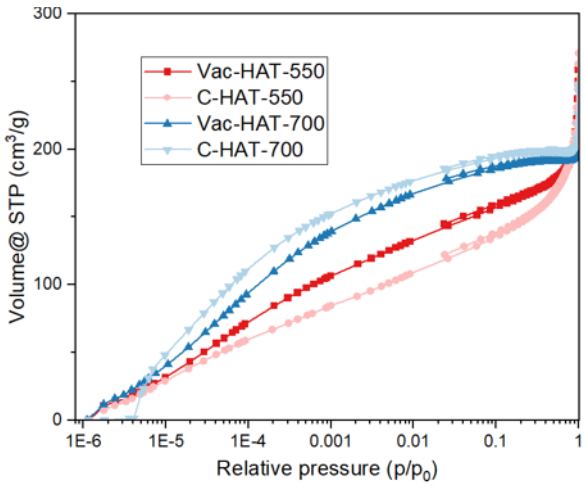

Figure S12. Logarithmic plots of Ar physisorption isotherms at 87 K of Vac-HAT-Ts and C-HAT-Ts.

6.4.1 List of tables

Table 1. EA summary of samples with and without pre-condensation. 42
Table 2. EA and yield of NOC-Xs and NOC-X-Ys materials. 43
Table 3. Ar physisorption at 87 K (specific surface area, pore volume, micropore volume), and CO_2/N_2 selectivity at 273 K data of NOC-Xs and NOC-X-Ys materials. 46
Table 4. N_2 physisorption at 77 K (specific surface area, pore volume), micropore volume from N_2 (77 K) and CO_2 (273 K) physisorption, elemental analysis, and CO_2/N_2 selectivity at 273 K data of the CMC-Xs materials. 68
Table 5. N_2 at 77 K (specific surface area, pore volume), Ar at 87 K (specific surface area, pore volume) micropore volume from N_2, Ar and CO_2 physisorption, EA, and yields of Vac-HAT-Ts and C-HAT-Ts. 84

Table S1. XPS data summary for atomic and weight percentage (rounded to two significant digits) of elements in the samples. 132
Table S2. ^{13}C CPMAS NMR chemical shifts and signal width at half maximum of fitted peaks for primary materials (citrazinic acid, pre-CMC-X and melamine) as well for CMC-X materials condensed at different temperature. 132
Table S3. Overview of estimated ^{1}H chemical shifts and signal widths regarding the dominating/most intensive signals for primary materials (citrazinic acid, pre-CMC-X and melamine) and condensed CMC-X materials at different temperature. 133
Table S4. Atomic percentage of the elements in CMC-Xs from EA and ICP-OES (rounded to a significant digit below the decimal point). 133

Table S5. N_2 physisorption at 77 K (specific surface area, pore volume), elemental analysis, and yield data of Vac-HAT-Ts at different condensation temperatures. 134

6.4.2 List of Figures

Figure 1.1 (a) Total energy supply by source from 1900 to 2018, and (b) increase of the atmospheric CO_2 concentration measured from 1958 to 2015. 1

Figure 2.1 Different carbon allotropes. (a) Cubic diamond, (b) graphite, (c) graphene, (d) carbon nanotube, (e) fullerene and (f) nanoporous carbon materials (adapted with permission from (a,b,c)[61], (d-f)[62], respectively) 7
Figure 2.2 (a) Synthesis methods of ordered mesoporous carbon materials *via* soft- templating (adapted with a permission from reference [115]) and (b) the soft- templating procedure on the example of SBA-15..... 12
Figure 2.3 Synthesis methods of ordered mesoporous carbon materials *via* hard- templating (adapted with a permission from reference [115]). 12
Figure 2.4 (a) Scheme of preparation of salt-templated carbons (STCs), (b) micro-/mesopore ratios in various STCs depending on the mass ratio of salts ($ZnCl_2$) and carbon precursors (sucrose) calculated based on the N_2 (at 77 K) and CO_2 (at 273 K) physisorption. (adapted with permission from reference (a,b)[57]), and (c) schematic illustration of porosity and morphology in carbon materials obtained from salt-templating by using various mixture of salts.[117] 13
Figure 2.5 Scheme illustration of various nitrogen functionalities in nitrogen-containing graphitic carbons. 17
Figure 2.6 (a) Electrochemical potentials for some known materials and (b) two reaction paths of carbonization for non-noble (reaction to upwards) and noble carbons (reaction to downwards) (adapted with permission from reference (a,b)[175])..... 22
Figure 2.7 (a) Scheme of porosity and surface chemistry for optimization of sorbent, (b) electrostatic potentials for CO_2 and N_2 mapped against the iso-electron density value of 0.005 a.u., and (c) representative CO_2 adsorption isotherms of 2 materials with similar uptake at 1 bar but different CO_2 capacity at low partial pressure (i.e., different gaps of CO_2 uptake between adsorption and regeneration conditions). (adapted with permission from reference (a)[200], (b)[201], and (c)[4])..... 28
Figure 2.8 (a) CO_2 isotherms from different types of pore structure of sorbent, and (b) water isotherms from different types of pore structure carbons. (adapted with permission from reference (a)[200], and (b)[205]) 30
Figure 2.9 (a) Specific power against specific energy for various electrical energy storage devices and (b) schematic of an electric double layer capacitor..... 32
Figure 2.10 Graphical overview of the functionalized porous carbon materials in this thesis.... 37

Figure 3.1 Preparation of nitrogen- and oxygen-lined salt-templated carbons with (NOC-Xs) and without (NOC-X-Ys) $ZnCl_2$ as pore stabilizer..... 42
Figure 3.2 (a) TGA curves under synthetic air, (b) XRD patterns, and (c) Raman spectra of NOC-Xs and NOC-X-Ys..... 44
Figure 3.3 Fitted Raman spectra of NOC-Xs and NOC-X-Ys. 44
Figure 3.4 High-resolution C1s and N1s XPS spectra with corresponding fitting curves of (a) NOC-350 and (b) NOC-550 as well as and HRTEM images of (c) NOC-350 and (d) NOC-550. 47
Figure 3.5 High-resolution C1s XPS spectra and corresponding fitting curves of NOC-Xs and NOC-X-Ys. 47
Figure 3.6 High-resolution N1s XPS spectra and corresponding fitted curves of NOC-Xs and NOC-X-Ys. 49
Figure 3.7 High-resolution O1s XPS spectra and corresponding fitted curves of NOC-Xs and NOC-X-Ys. 50
Figure 3.8 Scanning electron microscopy (SEM) images of (a) NOC-350, (b) NOC-550, (c) NOC-750, (d) NOC-950, (e) NOC-350-550, (f) NOC-550-750, and (g) NOC-550-950..... 50
Figure 3.9 EDX elemental mapping of C (red), N (greed), and O (blue) of (a) NOC-350 and (b) NOC-550..... 50
Figure 3.10 (a) Ar physisorption isotherms (87 K), (b) corresponding cumulative pore volume distribution, and (c) differential pore size distribution calculated with QSDFT (argon on carbons with cylindrical/sphere pores at 87 K) of NOC-Xs and NOC-X-Ys. 53
Figure 3.11 (a) CO_2 physisorption isotherms at 273 K, (b) CO_2 thermal response adsorption and desorption measurements at 1 bar and 25 ℃, and (c) integrated adsorption and desorption (left bar and right bar, respectively) temperature peak area normalized by the mass and the total pore volume from Ar physisorption of NOC-Xs and NOC-X-Ys..... 54
Figure 3.12 (a) Water vapor physisorption isotherms at 298 K, (b) normalized amount adsorbed relative to the maximum H_2O uptake at 298 K, and (c) the normalized uptake at relative pressure $p/p_0 = 0.2$ as a function of the nitrogen and oxygen content of NOC-Xs and NOC-X-Ys from XPS. 57
Figure 3.13 Preparation of salt-templated citrazinic acid and melamine based porous carbon (CMC-Xs). 64
Figure 3.14 (a) Fourier transform infrared (FTIR) spectra of citrazinic acid, the dried mixture of salts and citrazinic acid, CMC-550, CMC-750, and CMC-1000, (b) $^1H \rightarrow ^{13}C$ CPMAS NMR spectra and (c) ^1H MAS NMR of the precursor materials citracinic acid, pre-CMC-X, melamine, and CMC-Xs. (The black, grey, and red lines are figured by the experimental results, the individual Gauss/Lorentz simulated peaks in the $^1H \rightarrow ^{13}C$ CPMAS NMR, and the cumulative fitted curves spectra, respectively, and the signals marked with * and # are spinning sidebands, and a background signal of the probe that could not be suppressed, respectively.)..... 65
Figure 3.15 HRTEM images of (a,b) CMC-550, and (c,d)CMC-750. 68
Figure 3.16 (a) XRD patterns, (b) the raw (left, top) and fitted Raman spectra of CMC-Xs..... 69

Figure 3.17 (a) Nitrogen physisorption isotherms (77 K) and (b) differential pore size distribution with corresponding cumulative pore volume distribution (inset) calculated with QSDFT (nitrogen on carbons with slit/cylinder and pores at 77 K) of CMC-Xs. 70
Figure 3.18 (a) CO_2 physisorption isotherms at 273 K and (b) CO_2 thermal response adsorption and desorption measurements from 3rd cycle at 1 bar and 298 K, and (c) integrated adsorption temperature peak area normalized by the mass and the total pore volume from nitrogen physisorption (black line) and by the mass and the micropore volume less than 1.5 nm from CO_2 physisorption (red line) of CMC-Xs. 71
Figure 3.19 (a) H_2O physisorption isotherms at 298 K, (b) various temperatures of CMC-Xs, (c) isosteric heat (Q_{st}) from H_2O desorption curves of CMC-650, CMC-750 and CMC-1000, (d) thermal response measurements of H_2O adsorption (1bar, 298 K), and (e) correlation of H_2O total uptake at $p\ p_0^{-1} = 0.9$ from physisorption and normalizing temperature peak area of H_2O from InfraSORP by the mass of CMC-Xs. 73
Figure 3.20 (a) Thermal response measurements of H_2O adsorption (1bar, 298K) of CMC-Xs and (b) integrated adsorption (left) and desorption (right) temperature peak area normalized by the mass and the total H_2O uptake from H_2O physisorption at $p\ p_0^{-1} = 0.9$ of CMC-Xs. 75
Figure 3.21 DSC curves and the integrated surface area from 1st cooling cycle curve with baseline of water-filled (a,b) CMC-650, (c,d) CMC-750, and (e,f) CMC-1000. 76
Figure 3.22 (a) Cyclic voltammograms at different scan rates, (b) charge/discharge curves at different specific currents of CMC-1000, (c) specific capacitance with increasing scan rate, and (d) specific capacity with increasing specific current of CMC-750 and CMC-1000 in 1 M Na_2SO_4.78
Figure 3.23 Nyquist plots of CMC-750 and CMC-1000 tested in 1 M Na_2SO_4. 78
Figure 3.24 (a) Conductivity measurement of CMC-Xs, and cyclic voltammograms of (b) CMC-750, and (c) CMC-650 at different scan rates. 79
Figure 3.25 Charge/discharge profiles of CMC-750 and CMC-1000 at 1 A g^{-1} every 10 h in 1 M Na_2SO_4. 79
Figure 3.26 SEM images of (a) Vac-HAT-550, (b) C-HAT-550, (c) Vac-HAT-700, and (d) C-HAT-700. 84
Figure 3.27 (a) N_2 isotherms at 77 K, and (b) corresponding cumulative pore volume distribution, (c) Ar isotherms at 87 K and (d) corresponding cumulative pore volume distribution (insets: differential pore size distribution) of Vac-HAT-Ts and C-HAT-Ts. 86
Figure 3.28 CO_2 physisorption isotherms of Vac-HAT-Ts and C-HAT-Ts at (a) 273 K, and (b) 298 K. 88
Figure 3.29 Thermal response measurement of n-butane (1 bar, 298 K) of (a) Vac-HAT-550 and C-HAT-550, (b) Vac-HAT-700 and C-HAT-700 of adsorption in 3rd cycle (insets: 3 cycles of thermal response measurements), and (c) integrated adsorption and desorption peak areas (left and right bar, respectively) normalized by the total mass. 90
Figure 3.30 Thermal response measurement of CO_2 (1 bar, 298 K) of (a) Vac-HAT-550 and C-HAT-550, (b) Vac-HAT-700 and C-HAT-700 of adsorption in 3rd cycle (insets: 3 cycles of thermal response measurements), and (c) integrated adsorption and desorption peak areas (left and right bar, respectively) normalized by the total mass. 91

Figure 6.1 Classification of physisorption isotherms (adapted with permission from reference [68]) 114

Figure S1. FT-IR spectra of commercial citrazinic acid and the product after pre-condensation. 134
Figure S2. High-resolution transmission electron microscopy (HRTEM) images of (a) NOC-350, (b) NOC-550, (c) NOC-750, and (d) NOC-950. 135
Figure S3. (a) N_2 physisorption isotherms (77 K), (b) corresponding cumulative pore volume distribution, and (c) differential pore size distribution calculated with QSDFT (N_2 on carbons with cylindrical/sphere pores at 77 K) of NOC-Xs and NOC-X-Ys. 135
Figure S4. (a) Ar physisorption isotherms (87 K, filled and open symbols represent adsorption and desorption branches, respectively), (b) corresponding cumulative pore volume distribution, and (c) differential pore size distribution calculated with QSDFT equilibrium model (argon on carbons with slit pores at 87 K) of NOC-Xs and NOC-X-Ys. 136
Figure S5. (a) Logarithmic plots of CO_2 isotherms (273 K) in the low pressure range, (b) relation between the CO_2/N_2 selectivity at 273 K and the ratio of micropore volume to total pore volume from Ar physisorption, (c) CO_2 and N_2 physisorption isotherms of NOC-550 and NOC-750 measured at 298 K, and (d) the normalized uptake at relative pressure $p/p_0 = 0.2$ as a function of the N content of NOC-Xs and NOC-X-Ys from EA. 136
Figure S6. Photographs (a) after mixing the salts and citrazinic acid solutions and (b) after drying 1 h and after whole drying (inset). 137
Figure S7. SEM images of CMC-Xs. 137
Figure S8. Elemental mapping of C (red), N (greed), and O (blue) of (a) CMC-550, and (b) CMC-750. 137
Figure S9. N_2 physisorption isotherms at 273 K of CMC-Xs. 138
Figure S10. (a) H_2O physospriton isotherms magnified at low relative pressure region below and (b) normalized adsorption amount relative to the maximum H_2O uptake of CMC-Xs. 138
Figure S11. N_2 physisorption isotherms (77 K) of Vac-HAT-Ts obtained at different condensation temperatures. 138
Figure S12. Logarithmic plots of Ar physisorption isotherms at 87 K of Vac-HAT-Ts and C-HAT-Ts. 139

List of Publications

[1] **Sol Youk**; Edina Šić; Bolortuya Badamdorj; Antje Völkel; Ivan K. Ilic; Wuyong Zhang; Torsten Gutmann; Markus Antonietti and Martin Oschatz "Salt-melt synthesis of molecularly designed nanoporous carbon from citrazinic acid for physisorption and energy storage" *Manuscropt in preparation,* **2021**

[2] **Sol Youk**; Nadja Tarakina; Markus Antonietti and Martin Oschatz "Carbon materials with kinetically favorable pore structure by direct pyrolysis of a preorganized hexaazatriphenylene precursor" *Manuscropt in preparation,* **2021**

[3] Julian Heske; Ralf Walczak; Jan D. Epping; **Sol Youk**; Sudhir K. Sahoo; Markus Antonietti; Thomas D. Kühne and Martin Oschatz "When water becomes an integral part of carbon - combining theory and experiment to understand the zeolite-like water adsorption properties of porous C_2N materials" *submitted,* **2021**

[4] Jin Yang; Amitava Acharjya; Meng-Yang Ye; Jabor Rabeah; Shuang Li; Zdravko Kochovski; **Sol Youk**; Jérôme Roeser; Julia Grüneberg; Christopher Penschke; Michael Schwarze; Tianyi Wang; Yan Lu; Roel van de Krol; Martin Oschatz; Reinhard Schomäcker; Peter Saalfrank and Arne Thomas "Protonated imine-linked covalent organic frameworks for photocatalytic hydrogen evolution" *Angewandte Chemie International Edition (accepted),* **2021**

[5] Jinyeon Hwang; **Sol Youk**; Konstantin Schutjajew; Wuyong Zhang and Martin Oschatz "Bridging the gap between electrochemistry and gas physisorption to understand the interplay between heteroatoms and nanoporosity in all-carbon mixtures for efficient lithium storage" *submitted,* **2021**

[6] Jinyoen Hwang; Wuyong Zhang; **Sol Youk**; Konstantin Schujajew and Martin Oschatz "Understanding structure-property relationships under experimental conditions for the optimization of lithium ion capacitor anodes based on all-carbon-composite materials" *Energy Technology,* **2021,** 9, 2001054

[7] Stefano Mazzanti; Shaowen Cao; Katharina ten Brummelhuis; Jagadish Khamrai; Dmitry I. Sharapa; **Sol Youk**; Indrajit Ghosh; Burkhard König; Martin Oschatz; Markus Antonietti and Aleksandr Savateev "All-organic Z-scheme photoreduction of CO_2 with water as electron source, a full artificial photosynthesis" *Applied Catalysis B: Environmental,* **2021**, 285, 119773

[8] **Sol Youk**; Jan P. Hofmann; Bolortuya Badamdorj; Antje Völkel; Markus Antonietti and Martin Oschatz "Controlling pore size and pore functionality in sp^2- conjugated microporous materials by precursor chemistry and salt templating" *Journal of Materials chemistry A,* **2020**, 8, 21680

Declaration

Die vorliegende Dissertation entstand in dem Zeitraum zwischen März 2019 und Juni 2021 am Max-Planck-Institut für Kolloid- und Grenzflächenforschung unter Betreuung von Prof. Dr. Dr. h.c. Markus Antonietti.
Hiermit erkläre ich, dass die vorliegende Arbeit selbstständig angefertigt wurde und keine anderen als die angegebenen Hilfsmittel und Quelle verwendet wurden.
Die Arbeit wurde bisher weder im Inland noch im Ausland in gleicher oder ähnlicher Form einer anderen Prüfungsbehörde vorgelegt. Es habe bisher keine früheren erfolglosen Promotionsverfahren stattgefunden.

The present work was carried out during the period of March 2019 to July 2021 at the Max Planck Institute of Colloids and Interfaces under supervision of Prof. Dr. Dr. h.c. Markus Antonietti.
I declare that I have written this work on my own and used no other than the named aids and references.
This thesis was not submitted to another examination board in this or other countries. There were no unsuccessful examination processes.

Sol Youk

Potsdam, den 16.08.2021